REACTIVE ION BEAM ETCHING AND CHARACTERIZATION OF HIGH-T$_c$ SUPERCONDUCTOR Bi2212

A Thesis submitted to
The Graduate School of Engineering and Science of
İzmir Institute of Technology
in Partial Fulfillment of the Requirements for the Degree of

MASTER OF SCIENCE

in Physics

by
Hasan KÖSEOĞLU

June 2009
İZMİR

We approve the thesis of **Hasan KÖSEOĞLU**

_____

Assoc. Prof. Lütfi ÖZYÜZER
Supervisor

_____

Prof. Doğan ABUKAY
Committee Member

_____

Prof. Mustafa EROL
Committee Member

25 June 2009

_____   _____

Prof. Durmuş Ali DEMİR   **Prof. Hasan Böke**
Head of the Physics Department   Dean of the Graduate
                                                     School of Engineering and Sciences

ACKNOWLEDGEMENT

ABSTRACT

REACTIVE ION BEAM ETCHING AND CHARACTERIZATION OF HIGH T_c SUPERCONDUCTOR Bi2212

The lack of coherent, continuous and tunable compact solid-state sources of electromagnetic radiations at terahertz (THz) frequency range (0.3-30 THz) can be solved by high temperature superconductors (HTS) which are better candidates for generation of THz radiation. THz sources have potential application areas in materials characterization, biology, communication, medicine and security. The HTSs have large energy gap intervals which are available for radiations at THz frequency range, so recently, they were used as better converters from DC-voltage to high frequency radiation in junction technologies. $Bi_2Sr_2CaCu_2O_{8+\delta}$ (Bi2212) HTS single crystals include natural superconductor-insulator-superconductor multi-junctions called intrinsic Josephson junctions. For generation of coherent continuous and powerful THz radiations, we have fabricated large and tall mesas on Ca rich Bi2212, although mesas with small planar and lateral dimensions were preferred in recent studies because of the heating effect. We have used underdoped Bi2212 to control the heating problem. By using the vacuum thermal evaporation, optical photolithography, magnetron sputtering and reactive ion beam etching techniques, the mesas with size of 40-100x300 μm^2 have been fabricated by using single layer mask (PR) and two different multilayer masks, which are Ta/PR and PR′/Ta/PR. Their heights and lateral dimensions were analyzed by Atomic Force Microscopy, profilometer and SEM. We have investigated temperature dependence of c-axis resistivity and current-voltage (I-V) tunneling characteristics of under-doped Bi2212 which exhibit exponentially increases in resistivity from 300 K to T_c. The influences of heating effect were analyzed at temperature evolution of I-V measurements. Finally, bolometric detections of emission from long edges of mesas were done.

ÖZET

YÜKSEK SICAKLIK ÜSTÜNİLETKENİ Bi2212' NİN REAKTİF İYON DEMETİ DAĞLANMASI VE KARAKTERİZASYONU

Terahertz frekans aralığında (0.3–10 THz) koherent aralıksız ve ayarlanabilir bir şekilde elektromanyetik ışıma yapacak kompakt katı hal kaynaklarının eksikliği, bu ışınlarını elde etmede daha iyi bir aday olan yüksek sıcaklık süperiletkenlerle çözülebilir. THz kaynakları; materyal karakterize etmede, biyolojide, iletişimde, tıpta ve güvenlik alanlarında geniş uygulama potansiyeline sahiptir. Yüksek sıcaklık süperiletkenleri ise THz frekans aralığına ışıma yapmak için uygun olan büyük enerji aralıklarına sahiptir. Bu yüzden bu süperiletkenler eklemli yapı teknolojilerinde, DC voltajı yüksek frekanslı ışımaya çeviren iyi bir dönüştürücü olarak kullanılmaktadırlar. Bir süperiletken olan $Bi_2Sr_2CaCu_2O_{8+d}$ (Bi2212) tek kristalleri özgün Josephson eklemleri şeklinde anılan doğal süperiletken yalıtkan süperiletken gibi üst üste çoklu eklemli yapılar içerir. Isınma olaylarından ötürü küçük düzlemsel ve yanalsal boyutlu mesalar tercih edilmesine rağmen, koherent aralıksız ve güçlü bir şekilde THz ışımalarını elde etmek için, Ca ile zenginleştirilmiş Bi2212 üzerine geniş ve uzun boyutlarda mesalar ürettik. Isınma problemini kontrol edebilmek için normal düzeyin altında O2 katkılandırılmış Bi2212 kullandık. Vakumlu termal buharlaştırma, optik fotolitografi ve iyon demeti aşındırma metotları kullanılarak, 40-100x300 μm^2 boyutlu mesalar tek katman maske (PR) ve Ta/PR ve PR′/Ta/PR olan iki farklı çoklu katman maske ile üretildi. Mesaların yükseklikleri ve yanal boyutları Atomik Kuvvet Mikroskobuyla analiz edildi. Bi2212'nin sıcaklığa bağlı c-ekseni özdirencini ve akı m-voltaj (I-V) tünelleme niteliklerini inceledik. Bu incelemelerde 300 K ten T_c'ye üssel olarak artan bir özdirenç normal düzeyin altında O_2 katkılandırılmış bir Bi2212 süperiletkeni ile çalışıldığını göstermektedir. Sıcaklıkla değişen I-V ölçümlerinde ısınma olayının etkileri analiz edildi. Son olarak mesaların uzun kenarlarından bolometrik ışıma algılama ölçümleri yapıldı.

TABLE OF CONTENTS

LIST OF FIGURES

LIST OF TABLES

CHAPTER 1

INTRODUCTION

1.1. Phenomenon of Superconductivity: Its Discovery and Evolution

The phenomenon of superconductivity has been known for almost hundred years. It was discovered in 1911 by H. Kamerlingh-Onnes (Onnes 1911) who pioneered the refrigeration technique required to reach temperatures a few degrees above absolute zero (0 K). He studied the temperature dependence of the resistance of a sample of mercury and found very surprising behavior of it. At a temperature of $T_c \sim 4$ K, the resistance dropped to zero and remained unmeasurably small at temperatures below T_c. This temperature dependence of the resistance is schematically illustrated in figure 1.1. It is important to notice that the resistance at temperatures below T_c is not just very small, but is exactly zero! Thus, any small electrical current which may occur in the superconducting sample will not decay and persists as long as the sample temperature is kept below T_c.
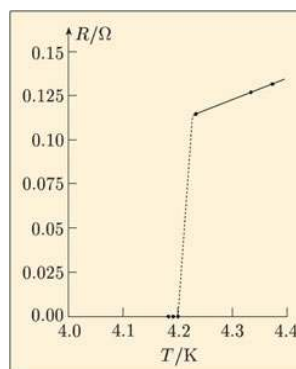
Figure 1.1. Experimental data obtained in mercury by Gilles Holst and H. Kamerlingh Onnes in 1911, showing for the first time the transition from the resistive state to the superconducting state.

Several other simple metals (Sn, In, Al, and others) were found to be superconductors soon after the discovery of this phenomenon in mercury. The highest superconducting transition temperatures among pure metals were found for Nb and Pb, about 9.2 K and 7.2 K, respectively.

The second outstanding feature of superconductivity is perfect diamagnetism, which is known as Meissner Effect (Meissner and Ochsenfeld 1933). In 1933, Meissner and Ochsenfeld discovered that superconductors expel magnetic fields from their interior. If some material has zero resistance, then it is known from Maxwell's equations that it will not allow a magnetic field to enter through the boundaries. If, however, the magnetic field is present before the material becomes a perfect conductor, then it will remain inside the material. In the 1950's it was determined that superconducting materials can be separated into two categories exhibiting different behavior, type I and type II superconductors. A Type I superconductor completely obeys Meissner effect but a Type II superconductor have two critical magnetic fields H_{c1} and H_{c2}. Below first critical magnetic field (H_{c1}) it expels magnetic field and above this value magnetic flux penetrate into the material in normal regions surrounded by superconducting ones. The material remains perfect conductor until applied magnetic field exceed second critical magnetic field (H_{c2}). Both H_{c1} and H_{c2} depend on temperature. In the mixed state, also called vortex state, the magnetic field penetrates into superconductor in quantized units of magnetic flux,

$$\Phi = h / 2e = 2.068 \times 10^{-15} \text{ Wb} \tag{1.1}$$

Thus, in the mixed state there are normal regions surrounded by superconducting regions. The magnetic field vs. temperature and the transition behavior of type-I and type-II superconductors under externally magnetic field is shown in the figure 1.2.
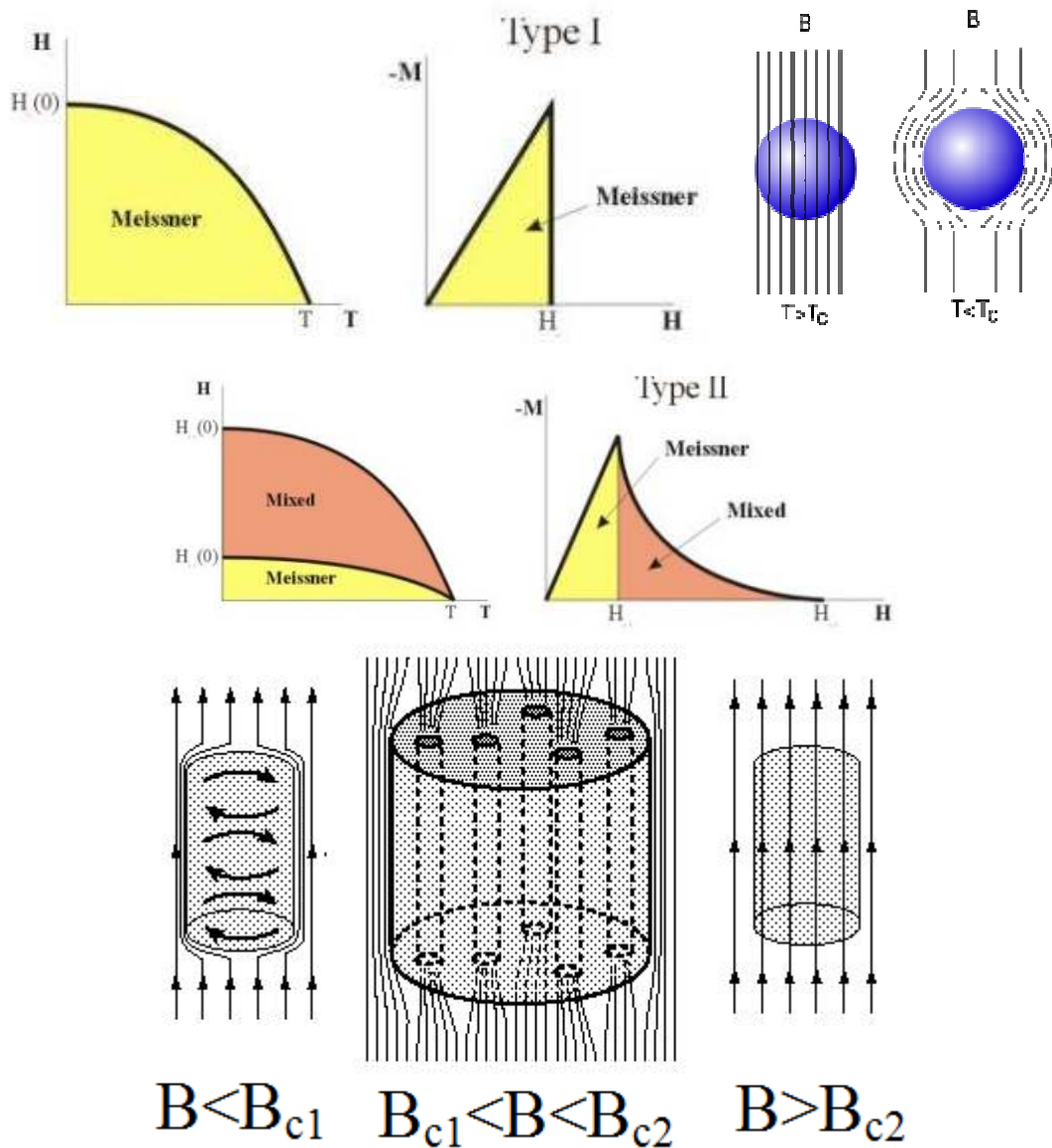
Figure 1.2. The magnetic field vs. temperature and the transition behavior of type-I and type-II superconductors under externally magnetic field

The report of the Meissner effect led the London brothers, Fritz and Heinz, to propose equations that explain this effect and predict how far a static external magnetic field can penetrate into a superconductor (London and London 1935). They proposed the relationship

$$\nabla \times J_s = -\frac{n_s e^2}{mc} H \tag{1.2}$$

where J_s is the supercurrent density, n_s is the density of supercurrent carriers, m is the mass of a supercurrent carrier, and H is the magnetic field. Such a relationship together with Maxwell's and Newton's equations leads to the Meissner effect, but also superconducting vortices may be described by the theory.

Another phenomenological theory was put forth in 1950 by Landau and Ginzburg. The theory combined Landau's theory of second order phase transitions with a Schrödinger-like wave equation, and has great success in explaining many properties of superconductors. A breakthrough was made by Abrikosov who showed the existence of two types of superconductors and the vortex state, only found in Type-II superconductors. It is known that in some limit the theory reduces to the London theory. Ginzburg, Abrikosov, and Legget (superfluids) received a Nobel Prize in 2003 for pioneering contributions to the theory of superconductors and superfluids.

It was predicted theoretically by H. Fröhlich (1950) that the transition temperature would decrease as the average isotopic mass increased. This effect, called the isotope effect, was observed experimentally the same year (Maxwell 1950, Reynolds, et al. 1950). The isotope effect provided support for the electron-phonon interaction mechanism of superconductivity.

A microscopic theory explaining the superconductive state has been formulated not until the year 1957 by Bardeen, Cooper and Schrieffer. Their Theories of Superconductivity became know as the BCS theory (Bardeen, et al. 1957), derived from the first letter of each man's last name and won them a Nobel Prize in 1972. According to their theory, conduction electrons of opposite spin and momentum form bound pairs under the influence of a lattice phonon-induced attraction. The resulting particle, a so-called Cooper pair, has a spin of zero and hence obeys the Bose-Einstein statistics. This implies that, at low temperatures, all Cooper pairs condense into a ground state of lowest energy, while single electron states, which are called quasiparticles, are energetically separated by a gap Δ that is related to the binding energy of the Cooper pair. The Ginzburg–Landau (1950) and London (1950) results fit well into the BCS formalism. Experimentally, the energy gap varies with temperature that is also predicted by BCS theory. At T=0, the ratio $2\Delta(0)/k_B T_c$ variation with superconductor elements are typically between 3.2 and 4.6 but this radio predicted by BCS theory is equal to 3.5

(Wesche 1998). Much of the present theoretical debate centers on how well the BCS theory explains the properties of the new high temperature superconductors.

In 1959 Gor'kov showed that the BCS theory reduces to the phenomenological Ginzburg Landau theory when the temperature is close to the transition temperature (Gor'kov 1960). This is tremendously important, since it explains the validity of the Ginzburg-Landau theory allowing in many cases for simpler calculations than the BCS theory.

The extremely important phenomenon of tunneling in superconductors was discovered around 1960. Giaever did experiments on superconducting tunneling systems (Giaever 1960) and a few years later, Josephson explained tunneling in superconductors theoretically (Josephson 1962). Giaever, Josephson, and Esaki (semiconductors) received a Nobel Prize in 1973 for their work (Esaki and Giaever for their experimental discoveries regarding tunneling phenomena in semiconductors and superconductors respectively, Josephson for his theoretical predictions of the properties of a supercurrent through a tunnel barrier, in particular those phenomena which are generally known as the Josephson effects).

1.2. High Temperature Superconductors

Many years of research after the Kamerlingh-Onnes discovery, numerous superconducting alloys and compounds had been discovered, with the highest T_c being about 23 K. Although physicists had believed that BCS theory forbade superconductivity at temperatures between 30 and 40 K due to thermal vibrations, another milestone in the field of superconductivity came in 1986 when Muller and Bednorz discovered superconductivity in copper-oxide based compounds. For this discovery they were awarded the Nobel Prize as soon as in 1987. The accomplishment of Muller and Bednorz was that they showed a measurement with a transition temperature above 35 K of a compound consisting of La, Ba, Cu, and O ($La_{2x}Ba_xCuO_4$) (Bednorz and Müller 1986). This important discovery has renewed the interest in the superconductive researches. A striking evolution came in 1987 with the discovery of

high-temperature superconductivity in the complex ceramic oxide $YBa_2Cu_3O_7$ by replacing La^{3+} with Y^{3-}, which has a critical temperature of about 92 K (Wu, et al. 1987). With this discovery superconductivity entered a new era, since superconductors could then be cooled with liquid nitrogen, boiling at 77 K and much cheaper than liquid helium. Just a year later in 1988, Bi and Tl based superconducting cuprates were discovered with the critical temperature T_c=110 K (Maeda, et al. 1988) and 125 K (Hazen, et al. 1988), respectively. Finally, Hg based cuprates with the highest critical temperature T_c=135 K was discovered in 1993 (at high pressure, T_c increased up to 164 K) (Schilling, et al. 1993). Figure 1.3 shows the superconducting critical temperature of several cuprates as a function of the year of discovery, as well as T_c of some metallic superconductors.
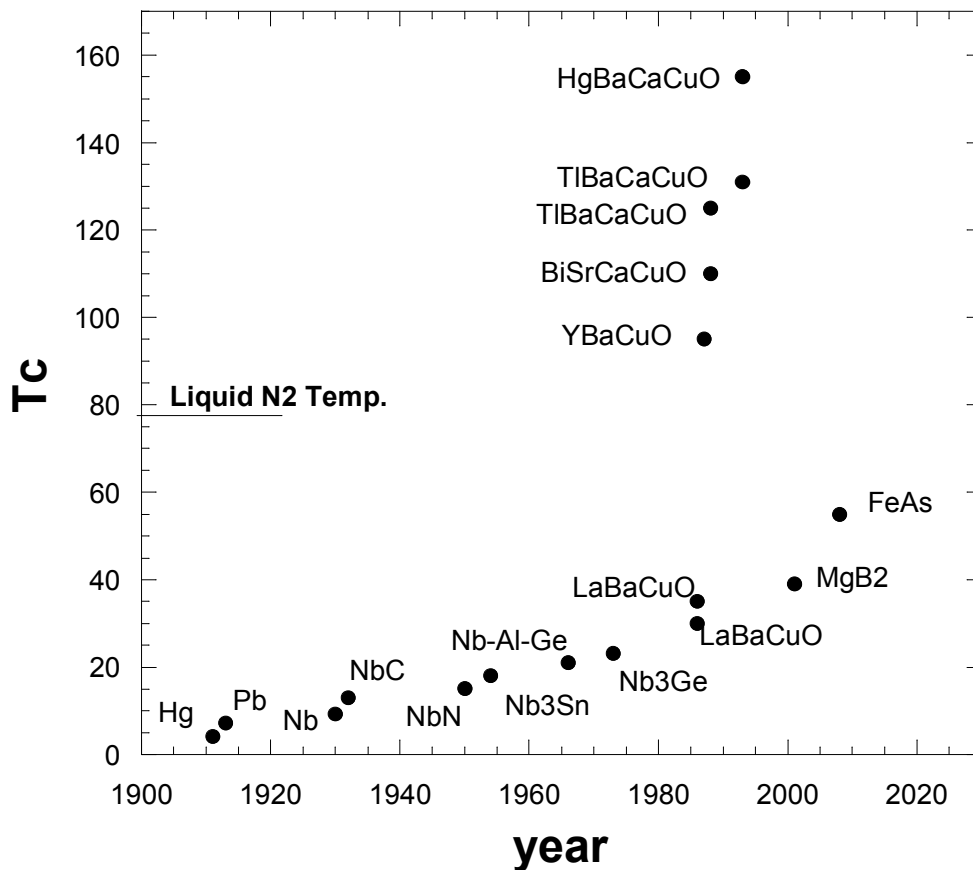
Figure 1.3. The critical temperature evolutions of the superconducting materials

All of the HTSs have a layered crystal structure and they include copper oxide layers providing superconductivity separated by non-superconductor layers. They are base on oxygen defect modification of a perovskite structure which is adopted by many oxides that have the chemical formula ABO_2. Its structure is a primitive cube, with the A-cation in the middle of the cube, the B-cation in the corner and the anion, commonly oxygen, in the centre of the face edges. Due to these layered structures of HTSs, at critical field, London penetration dept, coherence length and resistivity they have anisotropic behaviors. They are extremely type II superconductors and only these superconductors can be used for magnet and energy applications which can be well defined by the Ginzburg-Landau theory (Ginzburg and Landau 1950).

In 1959, it has been showed that this theory can be derived from the BCS theory (Gor'kov 1959). There are some different between Type I and type II superconductors, such as critical fields, London penetration dept λ and coherence length ξ. If a superconductor's coherence length is bigger than London penetration dept ($\xi > \lambda$), it shows that it has the characteristics of type I superconductors, but as the situation is $\xi < \lambda$, it has the characteristics of type II superconductors. Moreover, If the ratio λ/ξ called the Ginzburg-Landau parameter (κ) is greater than $1/\sqrt{2}$, superconductor must be type II (Wesche 1998). Although the values of the coherence length ξ of HTSs are short, they have large critical magnetic field.

1.3. AC Josephson Effect

Tunneling phenomena in superconductor provides valuable information about superconducting materials such as energy gap and other superconducting features. Two superconducting layers separated by very thin insulating layer are called Josephson junctions. Josephson theoretically predicted cooper pair tunneling across the insulating layers, apart from single electron tunneling, so they are called as Josephson junction (Josephson 1962). The insulating layer in SIS junctions can be such as cracks, grain boundaries and point contacts. The single electron tunneling is a well known phenomena and based on classical mechanics but his theoretical prediction on pair tunneling presented new important conception to superconductive theories. He

predicted that the cooper pair tunneling current through the barrier is depended on the difference of phases of the effective wave functions on the two sides of the junction and the phase difference is both temporally and spatially variable. Apart from single electron tunneling, there are no excitation and bias across the junction. Cooper pair tunneling occurs the Josephson current flowing without resistance until the critical current value I_c of the SIS junction is exceeded. After the critical current value I_c, voltage and current jump to values exhibiting single electron (quasiparticle) tunneling characteristic on the I-V (Duzer and Turner 1999).

There are two principle phenomena in Josephson effect which are DC and AC Josephson effects. When Josephson current flows at absence of any electrical and magnetic field, DC Josephson effect occurs. The current resulting from cooper pair tunneling across the thin insulating layer at zero voltage is dependent on phase differences between two superconductors on either side of the junction. If a constant nonzero voltage is applied across the insulating barrier, an alternating Josephson current occurs. This oscillating current is explained by AC Josephson effect. This oscillating current generates emission. Because of the radiation frequency proportional to the voltage, Josephson junctions are used such a voltage-frequency converter (Bourdillon and Bourdillon 1994).

1.4. Terahertz Radiation

Terahertz radiation is part of the electromagnetic spectrum (figure 1.4) lying between microwaves and the far-IR. This region has frequencies ranging from 0.1 – 10 THz and wavelengths from 3 mm to 0.03 mm. This spectral region is often referred to as the "THz gap" as these frequencies fall between electronic and optical means of generation. Terahertz radiation possesses unique characteristics not found in other portions of the spectrum. It matches in frequency the motion of an enormous range of chemical and biological molecules. Unlike far more energetic X-rays, T-rays do not have sufficient energy to "ionize" an atom by knocking loose one of its electrons. This ionization causes the cellular damage that can lead to radiation sickness or cancer. Since

T-rays are non-ionizing radiation, like radio waves or visible light, people exposed to terahertz radiation will suffer no ill effects. Furthermore, although terahertz radiation does not penetrate through metals and water, it does penetrate through many common materials, such as leather, fabric, cardboard and paper (Ferguson and Zhang 2002).
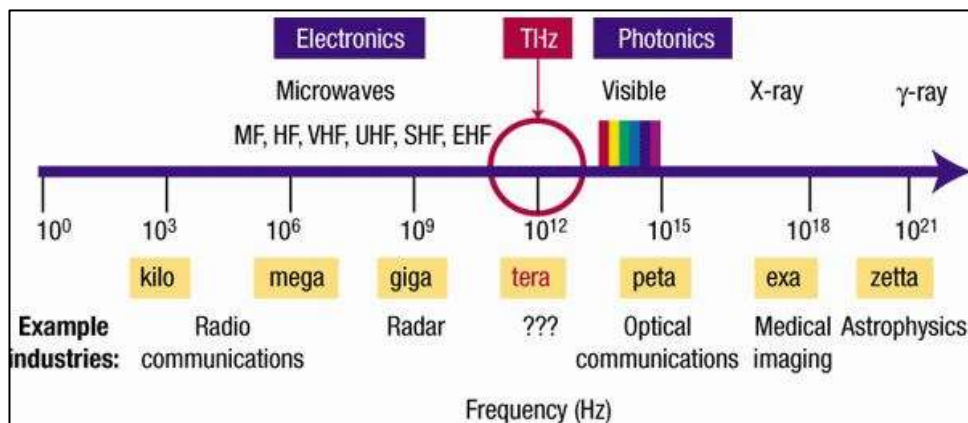
Figure 1.4. The electromagnetic spectrum with THz gap

This gap of the spectrum is extremely important. It is the most scientifically rich band of frequencies in the entire spectrum. Researchers have discovered over the past 20 years that organic molecules resonate at frequencies in this range. This means that the presence and composition of organic matter can be detected by Terahertz radar sending out terahertz frequencies. This has many interesting applications. The military and other security organizations are requesting hand held Terahertz radar to remotely detect the presence of explosive materials, poison gases, ceramic weapons, and biological warfare agents like viruses and bacteria. The medical community has shown that terahertz waves can detect the presence of cancer, viruses, bacteria, and other diseases instantly without surgery, biopsies, or other expensive procedures making this an important and urgent application of terahertz waves. Pharmaceutical and Agricultural companies are investigating the use of terahertz waves in quality control and research.

Since the 1990s, technical breakthroughs in sources and detectors have brought terahertz technology within striking distance of significant commercial markets. While work still needs to be done on components and systems to improve performance and lower cost, there are commercial terahertz systems on the market today, used for

product inspection and material evaluation. Industry participants are already planning for the growth of new markets that capitalize on the unique capabilities of terahertz technology.

1.4.1. Terahertz Sources

As of 2004, the only viable sources of terahertz radiation were the gyrotron, the backward wave oscillator (BWO), the far infrared laser ("FIR laser"), quantum cascade laser, the free electron laser (FEL), synchrotron light sources, photomixing sources, and single-cycle sources used in Terahertz time domain spectroscopy such as photoconductive, surface field, Photo-dember and optical rectificaiton emitters. The first images generated using terahertz radiation date from the 1960s; however, in 1995, images generated using terahertz time-domain spectroscopy generated a great deal of interest, and sparked a rapid growth in the field of terahertz science and technology. This excitement, along with the associated coining of the term "T-rays", even showed up in a contemporary novel by Tom Clancy.

There have also been solid-state sources of millimeter and submillimeter waves for many years. AB Millimeter in Paris, for instance, produces a system that covers the entire range from 8 to 1000 GHz with solid state sources and detectors. Nowadays, most time-domain work is done via ultrafast lasers.

The problem with Terahertz Waves is that they are difficult to create. These frequencies lie between the capabilities of typical optical devices and typical electronic devices. The devices that do exist to create Terahertz waves (besides those created by the Teraphysics Corporation) are inadequate for commercial use. They are either of extremely low power (in the Microwatt realm), or are too large to be of any practical use. A Free Electron Laser and a typical Backward Wave Oscillator images are seen in Figure 1.5.
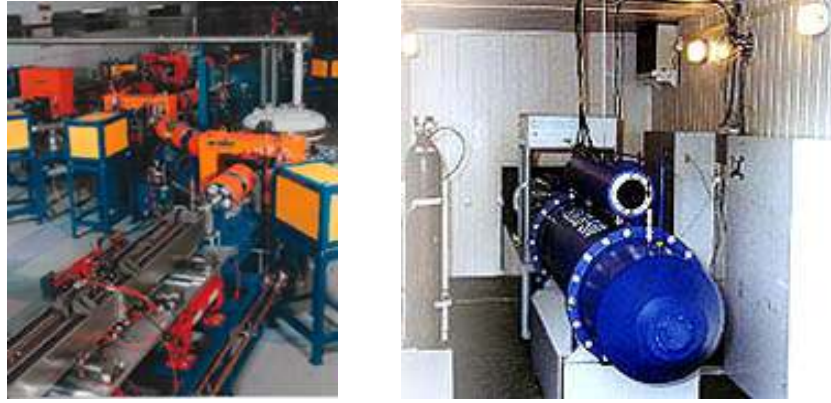
Figure 1.5. Image of Free Electron Laser- Typical Backward Wave Oscillator

However, in mid-2007, scientists at the U.S. Department of Energy's Argonne National Laboratory, along with collaborators in Turkey and Japan, announced the creation of a compact device that can lead to a portable, battery-operated source of T-rays, or terahertz radiation. This new T-ray source uses high-temperature superconducting crystals grown at the University of Tsukuba, Japan. These crystals comprise stacks of Josephson junctions that exhibit a unique electrical property: when an external voltage is applied, an alternating current will flow back and forth across the junctions at a frequency proportional to the strength of the voltage; this phenomenon is known as the Josephson Effect. These alternating currents then produce electromagnetic fields whose frequency is tuned by the applied voltage. Even a small voltage around two millivolts per junction can induce frequencies in the terahertz range. There is more about the detail of the generation of THz waves from HTS Bi2212 in Chapter 2.

There is a figure for the back and future of the THz sources in the THz region of the em spectrum, after M. Tonouchi published a figure like that (Tonouchi 2007). This figure (figure 1.6) summarized the THz emission power as a function of frequency. The first is optical THz generation, which has spearheaded THz research for the past few decades. The second is the recently developed THz-QCL, which is still being refined. The third is the Intrinsic Josephson Laser (TASER), which is toughed the present and future of the compact-solid state THz source with the large application area. The fourth uses solid-state electronic devices, which are already well established at low frequencies.
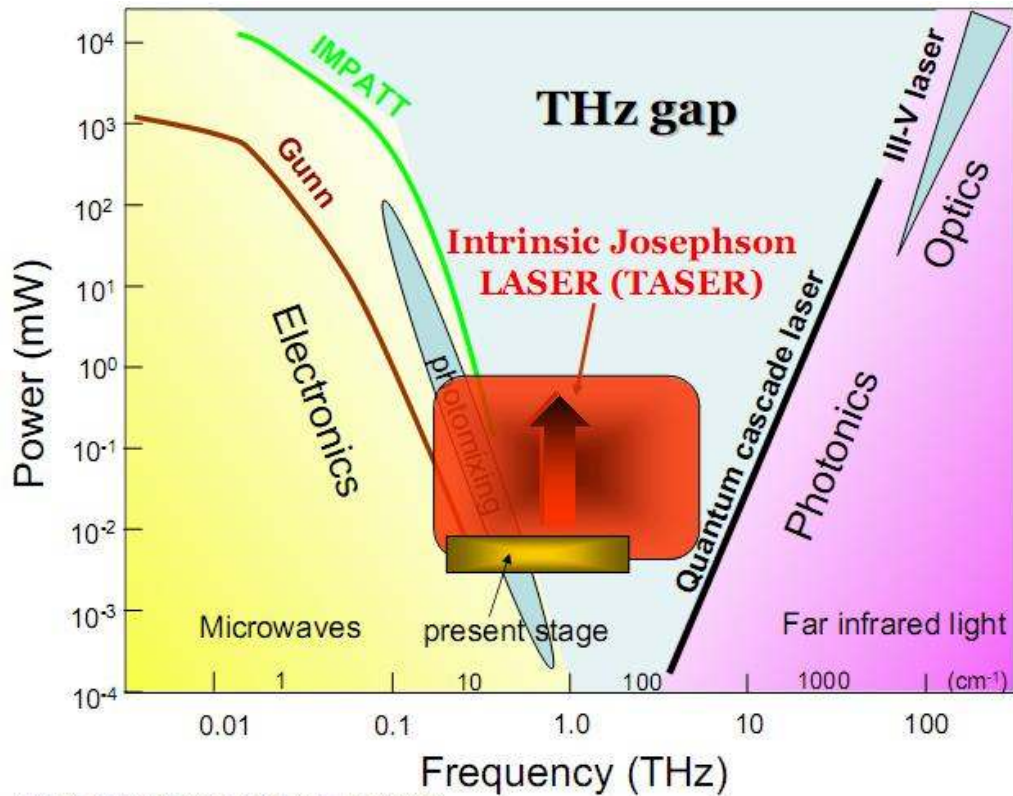
Figure 1.6. THz emission power as a function of frequency of the THz Sources

1.4.2. Applications of Terahertz Radiation

Although THz waves spread over wide area of electromagnetic spectrum, they are in the unexplored region. Nowadays, emission of THz frequency by the ability of the progressive detection and imaging is the one of the research topic, which is the most studied about it. Lots of applications areas are envisioned in this technology arena, which is discuss below are listed as a summary. These are;

- Airport screening of passengers for weapons, explosives, drugs or other contraband
- Secure wireless communications
- Cancer detection
- Imaging in dentistry

- Biochip analysis of DNA, proteins and other biological materials
- Detection of chemical and biological warfare agents
- Detection of land mines and buried explosive devices
- Measuring the water content of food to detect spoilage
- Inspecting finished products through packaging
- Determining the thickness of a layer of paint while it is still wet
- Quality control of insulated wires during manufacture
- Inspecting semiconductor wafers for defects
- Inspecting (and even reading) unopened mail

Medical imaging: Terahertz radiation is non-ionizing, and thus is not expected to damage tissues and DNA, unlike X-rays. Some frequencies of terahertz radiation can penetrate several millimeters of tissue with low water content (e.g. fatty tissue) and reflect back. Terahertz radiation can also detect differences in water content and density of a tissue. Such methods could allow effective detection of epithelial cancer with a safer and less invasive or painful system using imaging. Some frequencies of terahertz radiation can be used for 3D imaging of teeth and may be more accurate and safer than conventional X-ray imaging in dentistry.

Security: Terahertz radiation can penetrate fabrics and plastics, so it can be used in surveillance, such as security screening, to uncover concealed weapons on a person, remotely. This is of particular interest because many materials of interest have unique spectral "fingerprints" in the terahertz range. This offers the possibility to combine spectral identification with imaging. Passive detection of Terahertz signatures avoid the bodily privacy concerns of other detection by being targeted to a very specific range of materials and objects.

Scientific use and imaging: Spectroscopy in terahertz radiation could provide novel information in chemistry and biochemistry. Recently developed methods of THz time-domain spectroscopy (THz TDS) and THz tomography have been shown to be able to perform measurements on, and obtain images of, samples which are opaque in the visible and near-infrared regions of the spectrum. The utility of THz-TDS is limited when the sample is very thin, or has a low absorbance, since it is very difficult to

distinguish changes in the THz pulse caused by the sample from those caused by long term fluctuations in the driving laser source or experiment. However, THz-TDS produces radiation that is both coherent and broadband, so such images can contain far more information than a conventional image formed with a single-frequency source.

A primary use of submillimeter waves in physics is the study of condensed matter in high magnetic fields, since at high fields (over about 15 T); the Larmor frequencies are in the submillimeter band. This work is performed at many high-magnetic field laboratories around the world.

Terahertz radiation could let art historians see murals hidden beneath coats of plaster or paint in centuries-old building, without harming the artwork.

Communication: Potential uses exist in high-altitude telecommunications, above altitudes where water vapor causes signal absorption: aircraft to satellite, or satellite to satellite.

Manufacturing: Many possible uses of terahertz sensing and imaging are proposed in manufacturing, quality control, and process monitoring. These generally exploit the traits of plastics and cardboard being transparent to terahertz radiation, making it possible to inspect packaged goods.

Finally, some images about the some part of the applications of THz radiation area shown in the figure 1.7.

Pictures from Terahertz network (www.thznetwork.org)
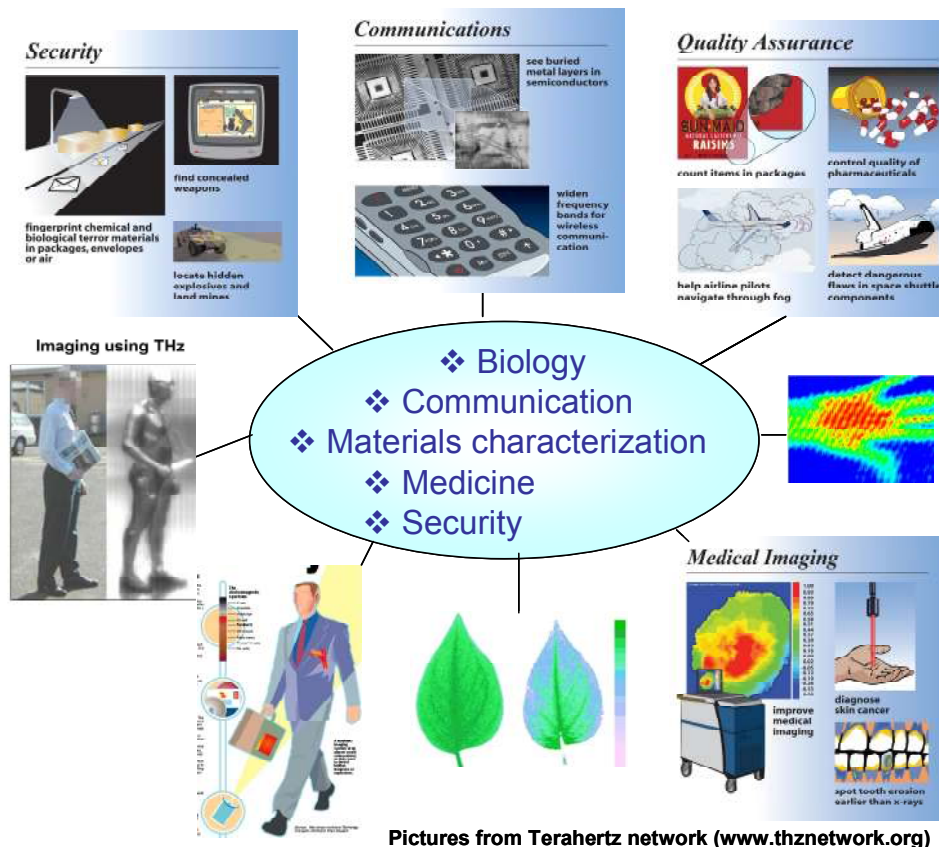
Figure 1.7. Some of the applications of THz radiation: fingerprint chemical and biological terror materials in package, find concealed weapons, widen frequency bands for wireless communication, control quality of pharmaceuticals and detect the human body diseases.

1.5. THz Emitting Mesa

High temperature superconducting $Bi_2Sr_2CaCu_2O_{8+\delta}$ (Bi2212) single crystals have natural junctions called intrinsic Josephson Junctions (IJJs). They play an important role for generation of THz radiation when a static voltage applied along the c-axis of Bi2212 (ac Josephson Effect) (Ozyuzer, et al. 2007). Generation of powerful THz radiation requires mesas with large lateral dimension but there are difficulties in fabrication of perfect rectangular mesa. It should be close to 90 degrees to obtain IJJs with same planar dimensions for synchronization of IJJs (Koshelev 2008).

In this study, the main purpose of our work is fabrication of mesas by using single layer mask (PR) and two different multilayer masks, which are Ta/PR and

15

PR′/Ta/PR for the generation of THz radiation. Thick photoresist layer (single layer mask) shades the lateral dimension of mesa during ion beam etching. Therefore, we patterned multilayer mask on Bi2212 and used selective ion etching as in Nagai, et al. 1991 overcome this problem (Nagai, et al. 1991). In this purpose, mesas fabricated by various experimental processes are anticipated to have smooth rectangular prism shape with large area, high thickness and lateral angle which are related to capability of emitting THz rays. Moreover, the surface and electrical characterizations of the mesas are important for our study. Atomic Force Microscope (AFM), Profilometer and Scanning Electron Microscopy (SEM) were used to analyze mesa height, the lateral angle of the mesa and thickness of the gold layer. In electrical characterizations including R-T and I-V measurements along the c-axis of Bi2212 crystal, the electrical behaviors proper to layered structure of HTSs were investigated. In the bolometer measurements, detection of the emission from the long edge of the mesa was investigated by using Si-Bolometer.

1.6 Organization of the Thesis

The thesis is organized as follows: Chapter 2 introduces the theoretical background, which is about the Bi2212, tunneling, Josephson effect and THz generation from HTS Bi2212 single crystals. In chapter 3, experimental techniques, the Bi2212 single crystal growth, the mesa fabrication and the characterization methods will be described. In chapter 4, AFM, RT and IV and Bolometer measurements results are discussed. Finally, in chapter 5 the results will be summarized and the thesis will be concluded.

CHAPTER 2

THEORETICAL BACKGROUND

2.1 Properties of $Bi_2Sr_2CaCu_2O_{8+\delta}$ Single Crystal

Structural features play important role for the superconductivity in HTSs. All ceramic superconductors are composed of similar building layers, which can be closely related to the classic perovskite ABO_3 structure. One of the layered HTSs is Bi based superconductors. The general formula for the Bi based HTSs can be stated as $Bi_2Sr_2Ca_{n-1}Cu_nO_{2n+4+}\delta$ (BSCCO), n represents the number of perovskite units or, equivalently, the number of consecutive copper oxide layers in the unit cell. There are 3 different phases of the Bi based HTS, which are $Bi_2Sr_2CuO_{6+\delta}$ (Bi2201) for n=1 with $T_c \leq 20$ (Akimitsu, et al. 1987), $Bi_2Sr_2CaCu_2O_{8+\delta}$ (Bi2212) for n=2 with $T_c \approx 95$ K and $Bi_2Sr_2Ca_2Cu_3O_{10+\delta}$ (Bi2223) for n=3 with $T_c = 110$ K (Maeda, et al. 1988) respectively.

More specifically within the Bismuth family, the $Bi_2Sr_2CaCu_2O_{8+\delta}$ (Bi2212) phase is the most used material and many researchers have focused on it since years. Single crystal of high temperature superconductor Bi2212 forms natural superconductor-insulator-superconductor (SIS) layered junctions, which are called intrinsic Josephson junctions (IJJ). Since these multi-junctions are perfectly stacked in Bi2212, they exhibit excellent device characteristics than artificially stacked Josephson junctions (Yurgens, 2000). Due to the layered structures of HTSs, they show anisotropic behaviors such as critical field, London penetration depth, coherence length, resistivity etc.

The Ginzburg-Landau parameter, κ, is larger than 100 for the Bi2212 phase, which means that it indicates strong type II superconducting behavior. Associated with this parameter, it has an extremely short coherence length $\xi_{ab}(0) = 20\text{–}40$ A° and $\xi_c(0)$

=0.1–0.3 A˚ at low temperatures and relatively large penetration depth λ_{ab} =2000 A˚ (Ting Wei-Li 1995).

Bi2212 has a crystal structure in which superconducting CuO_2 layers are in order stacked with insulator blocking Bi-O and Sr-O layers along to the c axis. The nature of the Bi2212 single crystal is based on a set of different layers, which are Cu-O, Bi-O, and Sr-O in the unit cell of the material. There are two models developed to be able to explain the mechanism of this material: multilayer model and proximity model (Yurgens, et al. 1996a) which are represented in Figure 2.1.
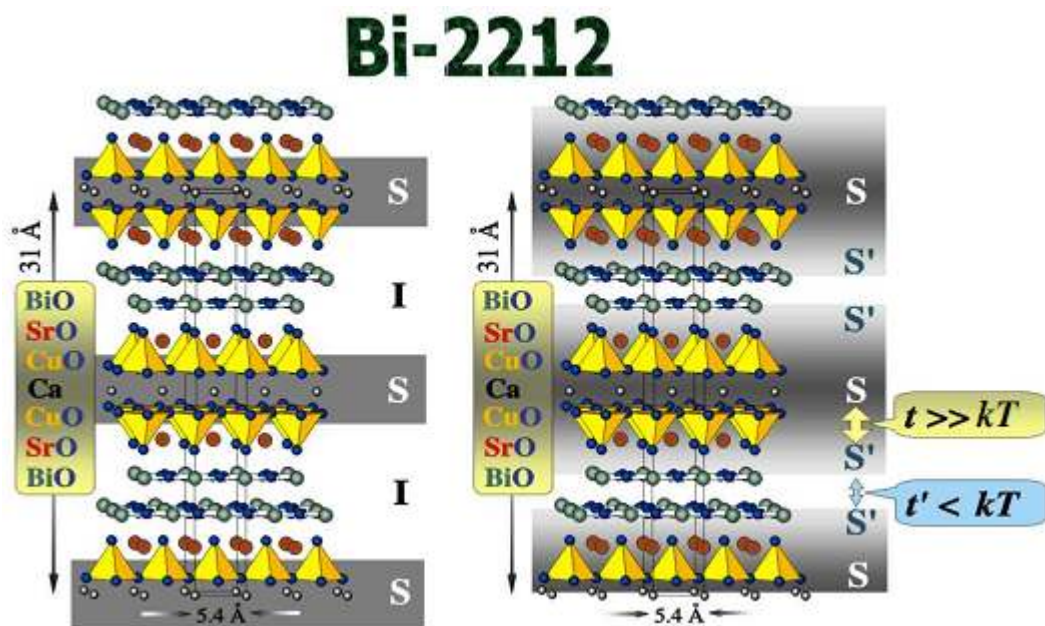
Figure 2.1.   The crystal structure of Bi2212, The left image corresponds to basic multilayer model and the right image defines the proximity model (Source: Yurgens, et al. 1996a)

According to the multilayer model (figure 2.1 (left image)), Bi2212 single crystals act as stacks of Josephson coupled Cu-O double layers with the thickness of 3 A˚ separated by non-superconducting Sr-O and Bi-O layers of thickness 12 A˚. This configuration forms natural Josephson tunnel junctions array going on like SISISIS... inside the single crystal and enables to observe both dc and ac Josephson Effects. Superconducting properties of the multilayered high T_c superconductors stem mainly from the double Cu-O layers in which coupling occurs, while the role of the other layers

can not be defined exactly. It is commonly believed that Sr-O and Bi-O intermediate planes behave as passive spacers or charge reservoirs. As stated above, the superconducting coherence length for Bi2212 in the out of plane direction is approximately 0.1 A°, which is relatively small if compared with the distance between two adjacent CuO layers in the Bi2212 unit cell. According to this point Josephson tunneling of Cooper pairs across the insulating layer is hard (Yurgens, et al. 1996a).

Another accepted model is proximity model (figure 2.1 (right image)), which suggests that not only CuO layers but also Bi-O planes make contribution to superconductivity of the HTS. Some experiments show that Bi-O layers exhibit metal-like or even superconducting features rather than insulating character. According to the proximity effect, there is a strong coupling between the Cu-O and Bi-O layers (S-S') with weak Josephson coupling between neighboring Bi-O layers (S'-S'). Some researchers claim that the reduced energy gap value of Bi2212 is the consequence of the proximity induced superconductivity of the Bi-O layers (Yurgens, et al. 1996a).

The structural anisotropy and existence of the Cu-O planes greatly affect the physical properties of BSCCO family. The single crystals of the anisotropic Bi2212 may be cleaved along ab plane without damaging the basic structure of the crystal. The Bi2212 grains may be aligned better than the grains of other HTSs. For the critical transition temperature, the optimally doped Bi2212 singe crystal has about a 95 K onset critical temperature which is the maximum value of T_c for this material and its transition temperature can be increased by additional oxygen content (overdoping) and decreased by the removal of oxygen with vacuum annealing (underdoping). The most important advantage of Bi2212 is that it can be grown in the way of single crystal without any macroscopic defects or dislocations.

2.2. Tunneling

The phenomenon of tunneling has been known for more than half century ever since the formulation of quantum mechanics. As one of the main consequences of quantum mechanics, a particle such as an electron, which can be described by a wave

function, has a finite probability of entering a classically forbidden region. Consequently, the particle may tunnel through a potential barrier which separates two classically allowed regions. The tunneling probability was found to be exponentially dependent on the potential barrier width. Therefore the experimental observation of the tunneling events is measurable only for the barriers that are small enough. Electron tunneling was for the first time observed experimentally in junctions between two semiconductors by Esaki in 1957 (Esaki 1957). In 1960, tunneling measurements in planer metal-oxide-metal junctions were performed by Giaever. If two conducting materials are brought together and interrupted with an ultra thin insulating layer, different kinds of tunneling junctions such as NIN, SIN, SIS (N: normal metal, I: insulator, S: superconductor) can be created.

For the normal metal-insulator-normal metal (NIN) Tunneling, consider two normal metals are separated by an insulating barrier at T=0 K. Their Fermi levels are aligned as shown in figure 2.2a, so tunneling does not occur. A positive-bias voltage is then applied to one of the metals, lowering its energy levels, as shown in figure 2.2b, so that the electrons are now able to tunnel from the top of the conduction band of the fixed metal to the empty continuum levels of the positively biased metal, as shown in the figure 2.2b. The number of empty levels that can receive electrons is proportional to the bias, so that the current flow is also proportional to it, as shown in figure 2.2c. The magnitude of the tunneling current is, of course, small compared to the current that flows in the absence of the barrier. Such a process satisfies the three conditions for tunneling namely presence of a barrier, energy conservation, and empty target levels (Wesche 1998, Duzer and Turner 1999).
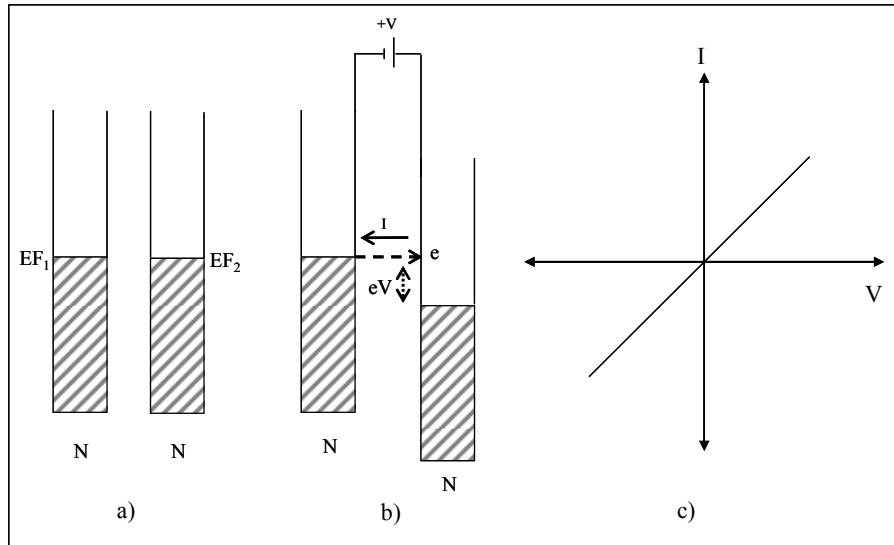
Figure 2.2. Tunneling in NIN junction a) Fermi levels aligned for zero applied voltage, b) application of a positive bias voltage V to metal 2, lowering its Fermi level by eV relative to metal 1 and causing electrons to tunnel from left to right (metal 1 to metal 2), corresponding to current flow opposite in direction to the electron flow, as indicated by the arrows, and c) linear dependence of the tunneling current on the applied voltage.

In addition to normal metal-insulator-normal metal (NIN) tunneling junction, there are also superconductor-insulator-normal metal (SIN), superconductor-insulator-superconductor (SIS) and Intrinsic Josephson Junction (IJJ) (multiple stacks of SIS) tunneling junctions.

2.2.1 NIS Tunneling

An insulating barrier between a normal metal and a superconductor is NIS junction. NIS tunneling processes shown as schematically the in figure 2.3, where the top three diagrams are the semiconductor representation and the middle diagrams sketch the boson condensation representation.

In the unbiased cases of figure 2.3b and 2.3e tunneling does not occur, because there is not any way for energy to be conserved by electrons tunneling to empty target levels. This is also true for the range $-\Delta/e<V<+\Delta/e$ of biases. For a positive bias, $V \geq \Delta/e$, electrons can tunnel from the conduction band of the normal metal to the empty

states above the gap of the superconductor, as shown in figures 2.3c and 2.3f. The figures appear similar in both representations, because Cooper pairs do not participate. For a negative bias, V≤-Δ/e, the process must be considered more carefully since the explanation is different in the two representations. In the boson condensation picture shown in figure 2.3d tunneling involves the breakup of a Cooper pair, with one electron of the pair tunneling down to the top of the normal metal conduction band and the other jumping upward to the quasiparticles energy band of the superconductor. Thus the paired electrons separate to create quasiparticles in the superconductor and transfer a conduction electron to the normal metal, with energy conserved in the process. In the semiconductor representation, only the electron that is transferred to the normal metal is taken into account, as shown in figure 2.3a. This electron leaves behind it a hole in an otherwise filled band; it is this hole which constitutes the quasiparticles. Figure 2.3g shows how the experimentally measured current flow between the metal and the superconductor depends on the bias (Wesche 1998).
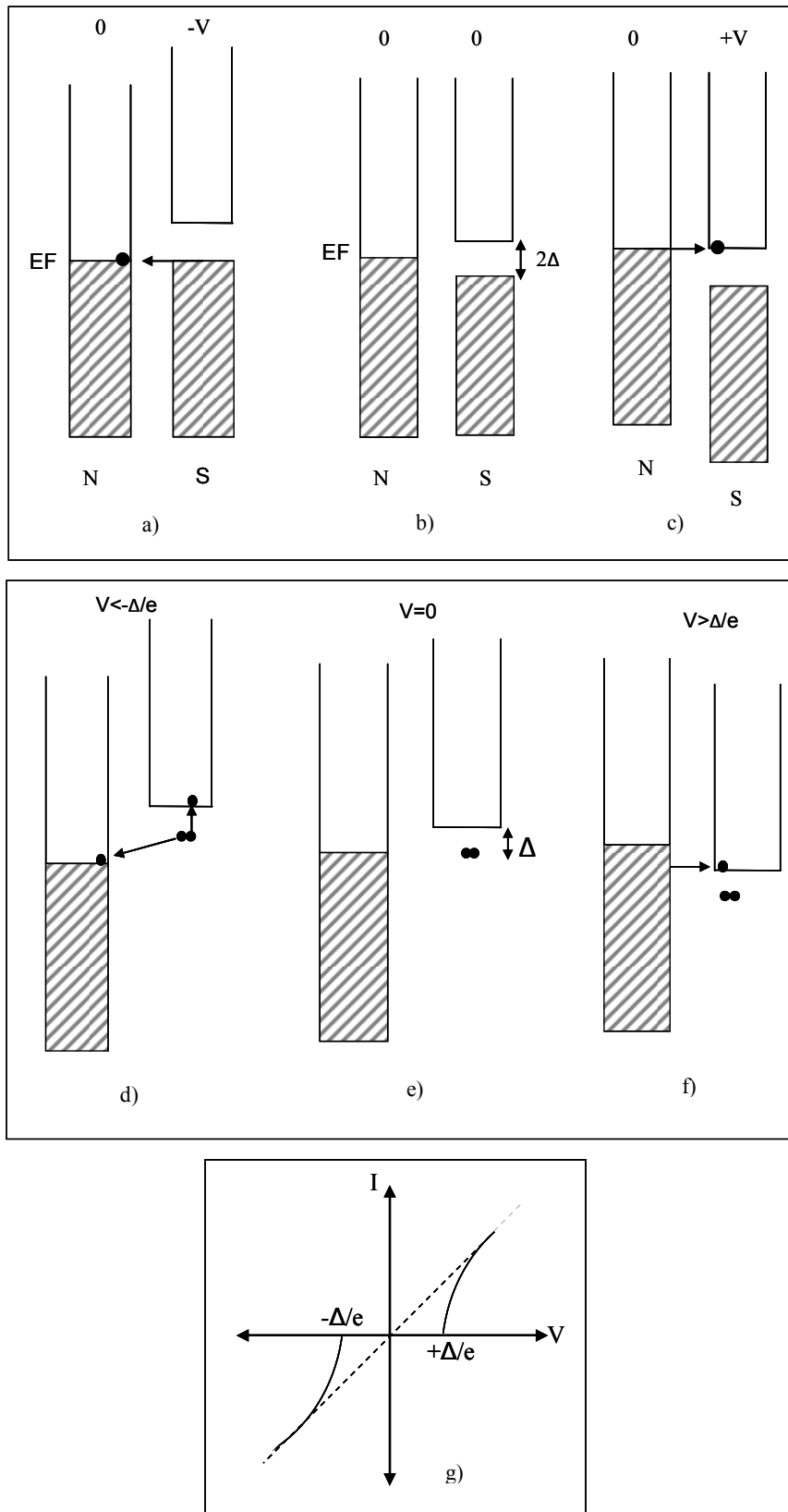
Figure 2.3.   The SIN tunneling process with representation of Bose condensation and
semiconductor and its current-voltage (I-V) characteristic at T= 0 K

In order to calculate the tunneling current, the one dimensional density of state in normal state N_n (E) and the density of states of quasiparticles excitations in superconductor state N_s (E) must be known. For the case of $\Delta < E' \leq eV$, it is given by Equation 2.1 at T= 0 K,

$$I_{sn}(T=0) = \frac{2\pi e}{\hbar} \int_{-\infty}^{\infty} \left| T^2 \right| \, N_n(E'-eV) \, N_s(E') \left[f(E'-eV) - f(E') \right] dE' \qquad (2.1)$$

In this equation, [T^2] is the tunneling matrix element and f (E, T) = $[1+\exp (E/ k_B T)]^{-1}$ is the Fermi-Dirac function. According to BCS theory, the density of states rate on both sides of the insulating barrier is given by Equation 2.2. It provides us to make an assumption between I-V characteristic and the density of states of quasiparticles in superconductor, N_s (E).

$$\frac{N_s}{N_n} = \begin{cases} 0 & |E| < \Delta \\ \dfrac{E}{\sqrt{E^2 - \Delta^2}} & |E| \geq \Delta \end{cases} \qquad (2.2)$$

Since N_n (E) is essentially constant near the Fermi level, the tunneling characteristic corresponds directly to the density of states of quasiparticles excitations N_s (E). The deviation of Equation 2.1 to the voltage, tunneling conductance dI/dV is proportional to the density of states of the superconductor. Using Equations 2.1 and Equation 2.2 and calculating the integral, the expression of dI/dV can be written as Equation 2.3 where G_n is the normal tunneling conductance.

$$\left(\frac{dI_{sn}}{dV} \right)_{T=0} = \begin{cases} G_n |V| / \left[V^2 - (\Delta/e)^2 \right] & |eV| \geq \Delta \\ 0 & |eV| < \Delta \end{cases} \qquad (2.3)$$

2.2.2 SIS Tunneling

In Superconductor-insulator-superconductor (SIS) tunneling spectroscopy, the focus of the experiments is on single electron (quasiparticle) tunneling which directly addresses the issue of unconventionality including temperature dependence of the gap size, gap symmetry, pseudo-gap and pairing mechanism. Therefore tunneling in HTSs with their large anisotropic properties and thermal fluctuation represents a large research field including the observation of many new effects experimentally.

S–I–S tunneling occurs through the processes depicted in figure 2.4 for the two representations. Over the range of biases $-2\Delta/e<V<+2\Delta/e$ an electron in the semiconductor representation can tunnel from the superconducting state of one superconductor to become a quasiparticle in the normal state of the other, as shown in figures 2.4a and 2.4c. As the bias voltage increases beyond the range $-2\Delta/e<V<+2\Delta/e$, the current increases abruptly in magnitude and then approaches its normal metal value, as indicated in figure 2.4d. The current-voltage characteristic for two identical superconductors is, of course, anti-symmetric about the point V=0. By anti-symmetric we mean that when $V\rightarrow-V$ we will have $I\rightarrow-I$. Note that the onset of tunneling for SIS junctions occurs at $V=\pm2\Delta/e$, which is twice the value for the NIS case.
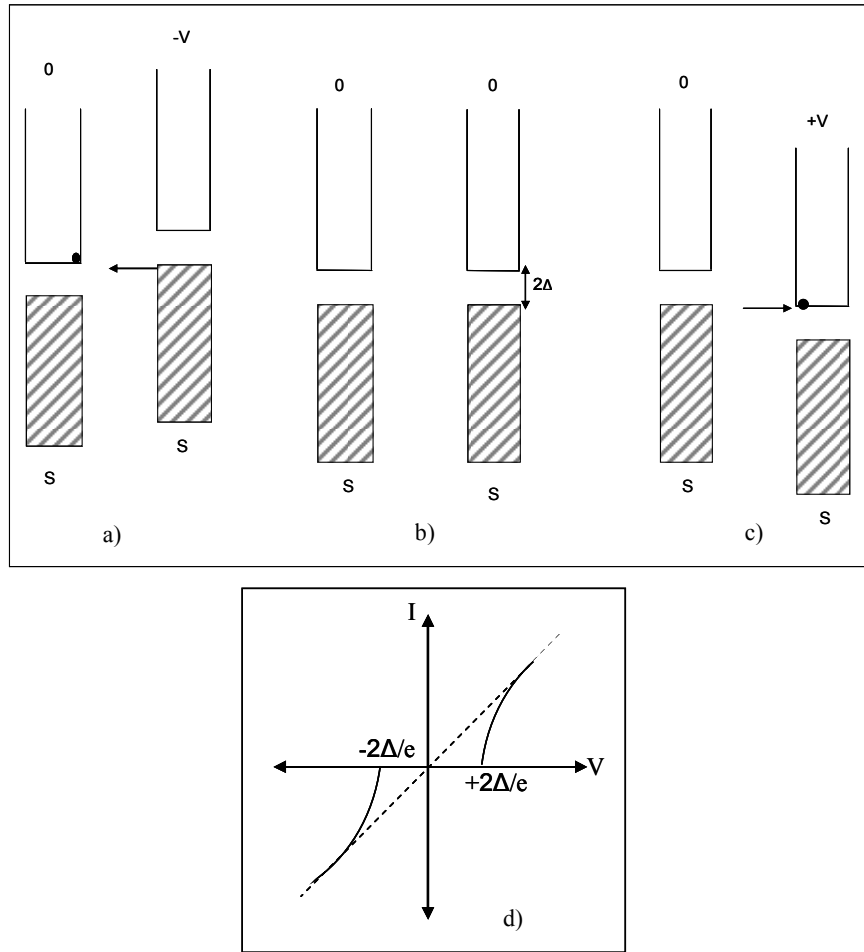
Figure 2.4.   Superconductor to superconductor tunneling at absolute zero. The semiconductor representation shows a) superelectron tunneling for V<-2Δ/e, b) zero tunneling current for bias voltages in the range -2Δ/e<V<2Δ/e. The current–voltage characteristic is given in d). The arrows show the electron tunneling directions, which are opposite to the current flow directions. The sketches are drawn with the superconductor on the left grounded.

Figure 2.4 was drawn for the case of T =0 K. For a finite temperature there will be some quasiparticles in each superconductor, so that a small tunneling current will flow for bias voltages below 2Δ/e, as shown in figure 2.5 in the boson condensation representation (a) and in the semiconducting representation (b). The current–voltage characteristic is given in figure 2.5c.
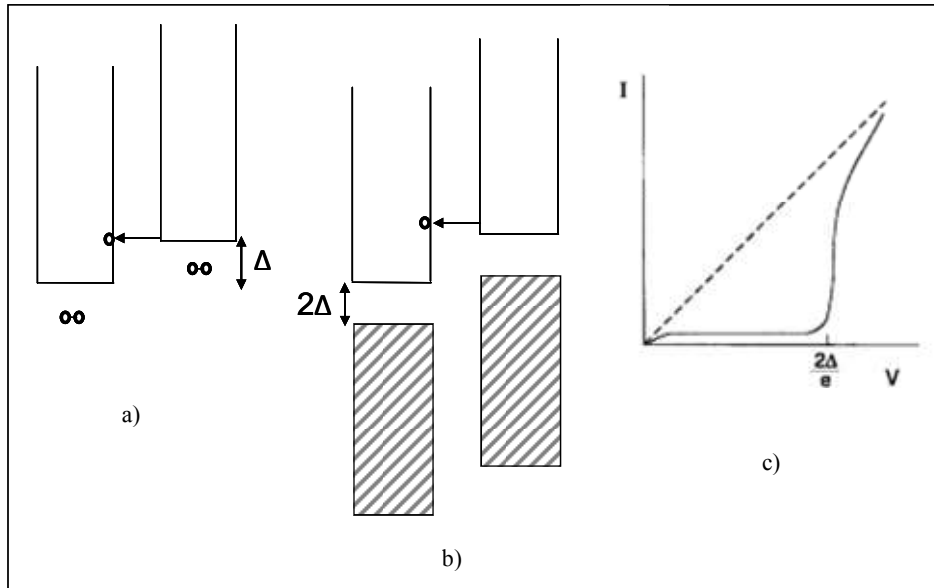
Figure 2.5. SIS tunneling at finite temperatures, T>0. The semiconductor representation a) and boson condensation representation b) show finite tunneling between upper quasiparticle levels sparsely populated by thermal excitation. The current–voltage characteristic c) shows a small current flow for 0 <V<2Δ/e, and the usual larger current flow for 2Δ/e<V.

One of two representations of single tunneling between two identical superconductors, Bose condensation representation is shown in figure 2.6. In order to start electron tunneling, applied voltage that causes shifting the Fermi level of the second superconductor connected to the positive pole of a battery to lower value is increased until the value of 2Δ/e. Thus Cooper pair breaking become possible in first superconductor and one of electron belong to pair can tunnel to the empty (quasi-particle) energy state of second superconductor. Since releasing energy from pair breaking is equal and greater than the energy gap value of first superconductor, the second electron of broken pair is excited to the quasi-particle energy state of first superconductor. At voltage V= -2Δ/e direction of tunneling reversely changes (Schmidt 1997).
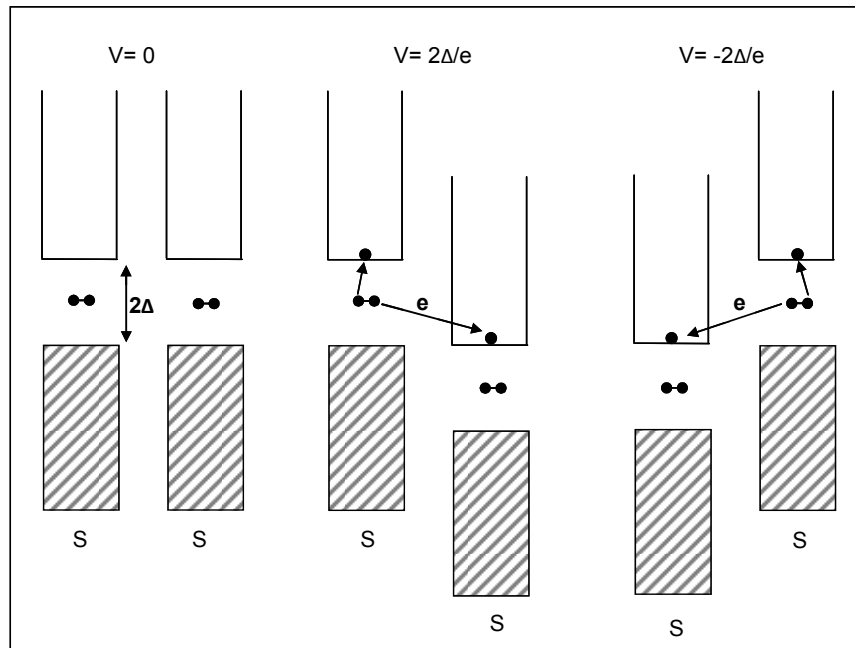
Figure 2.6. Bose condensation representation of single electron tunneling between two identical superconductors

In SIS tunneling spectroscopy, apart from single electron tunneling, Cooper pair tunneling through a very thin insulating layer is possible when applied voltage is zero. In 1962 B. D. Josephson predicted that the pair tunneling current is depended on the difference of phases of the effective wave functions on the two sides of the junction and the phase difference is both temporally and spatially variable (Josephson 1962). Although Cooper pairs tunneling through the barrier as particles with a spatial extension ξ_c is seen to be difficult, it can be well understood as the tunneling of the wave function describing the collective of the Cooper pairs. When the energy associated with coupling exceeds the thermal fluctuation energy, Cooper pairs can tunnel through the barrier without energy loss. Apart from single electron tunneling, there are no excitation and bias across the junction. The Josephson current is carried by Cooper pair and flows without resistance until the critical current value I_c of the SIS junction. After the critical current value I_c is exceeded, voltage and current jump to values on the I-V quasi-particle tunneling characteristic (Duzer and Turner 1999). I-V characteristic of the SIS junction is shown in figure 2.7.
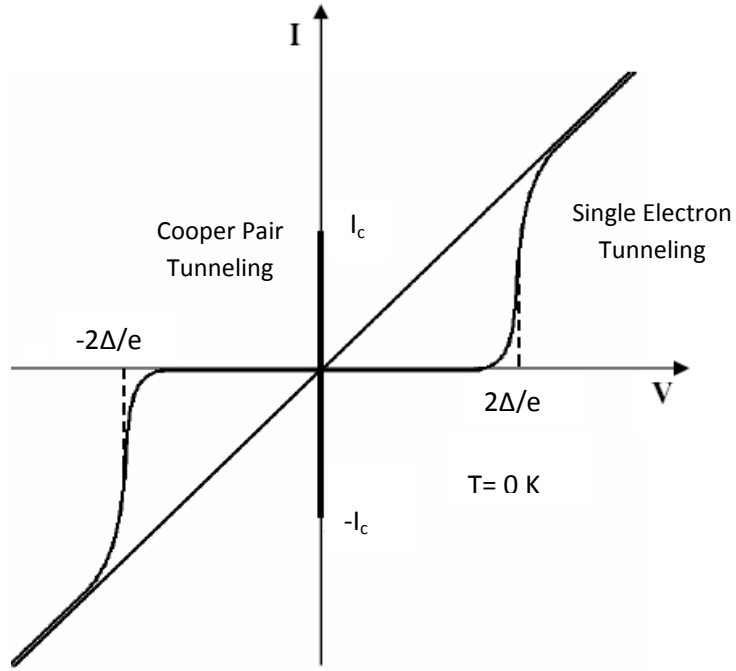
Figure 2.7. I-V characteristic of SIS junction with quasi-particle and Cooper pair tunneling at T= 0 K

In SIS junction, the tunneling conductance and the convolution of the density of states function of superconductor are proportional each other. The SIS tunneling current I_{ss} at T=0 is given by Equation 2.4.

$$I_{SS} = \frac{G_n}{e} \int_{-\infty}^{\infty} \frac{|E' - eV|}{\sqrt{[(eV - E')^2 - \Delta^2]}} \frac{|E'|}{\sqrt{(E'^2 - \Delta^2)}} [f(E' - eV) - f(E')] \, dE \qquad (2.4)$$

where G_n is normal tunneling conductance when tunneling occurs between two identical superconductors. Tunneling current, I_{ss} at voltage V= 2Δ/e is

$$I_c = \frac{1}{2} \pi \left(\frac{G_n}{e} \right) \Delta_{(0)} \qquad (2.5)$$

29

which is known as Josephson current. However, I-V characteristic seen in figure 2.6 will change due to thermal excitation when temperature starts to rise from absolute zero. Thus both DOS and energy gap decrease with temperature (Duzer and Turner 1999).

Superconductor energy gap structure in HTS cuprates is depended on not only temperature but also direction. While the energy gap in conventional superconductors is a constant in k space (s wave symmetry), HTSs with d wave pairing symmetry have anisotropic energy gap on the Fermi surface. Simple d-wave DOS defined by BCS type interaction of a two dimensional superconductor is given by

$$N_s(E,k) = \text{Re}\left\{\frac{E - i\Gamma}{\sqrt{(E - i\Gamma)^2 - \Delta(k)^2}}\right\} \tag{2.6}$$

where Γ is a smearing parameter to account for quasi-particle lifetime and the k dependent energy gap, $\Delta(k) = \Delta \cos(2\varphi)$ with maximum value of gap, Δ and polar angle in k-space φ (Won and Maki 1994). Temperature dependent of energy gap is given by below equation where k_B is the Boltzmann constant (Bardeen, et al. 1957).

$$\Delta(T) = 3.2 \, k_B \, T_c \, (1 - T/T_c)^{1/2} \tag{2.7}$$

2.2.3 Intrinsic Josephson Junction Tunneling

In the IJJ tunneling spectroscopy, c-axis tunneling of highly anisotropic layered HTSs such as Bi2212 is the most important in the limitations on their possible theories, due to their natural stacks of SIS multi-junction with the thickness of 1.5 nm. Therefore IJJ is not only an interesting subject for research by itself, but also a powerful tool to understand the nature of HTSs including physics of vortices in superconducting electronic applications. I-V characteristic of layered HTSs along the natural IJJ stacks

includes several branches due to the individual switching of each junction from Josephson state to quasiparticle state when the bias current exceeds the individual critical current of each junction (Yurgens 2000). Thus each of the junctions acts as one of the single branch in large gap voltage of all junctions and the branches are almost vertical these voltages.

In order to understand the IJJ tunneling of Bi2212, it will be easy to explain them on graphs including experimental I-V data. I-V graph along to c-axis of Bi2212 and dI/dV-V graphs at 4.2 K published by Ozyuzer et al. 2005 can be seen in the figure 2.8. In this study, comparison of I-V characteristics of IJJ and SIS junctions observed from the same crystal and differences in their energy gap values and I-V characteristic features are first realized. In figure 2.8a seven quasiparticle branches at the I-V graph corresponding to seven individual IJJs and in figure 2.8b dI/dV belong to the same data are seen respectively. Since it has seven branches, tunneling conductance peak, is divided into seven in order to obtain the value of $2\Delta/e$. If comparison in figure 2.8c between the value of Δ obtained from IJJ I-V data and energy gap Δ of SIS junction is considered, underestimate value of Δ in IJJ tunneling measurement is observed. The reason of lower energy gap value is excessive temperature than the bath temperature at local heating area in IJJ stacks. While they are observed SIS and SIN junction I-V measurements, the heating effect causes the absence of dip and hump feature in IJJ. Influences of the heating effect and non-equilibrium on tunneling measurement are unwanted negative characteristic of IJJ in Bi2212, because they suppress the superconductivity at local areas on Bi2212. Beside the absence of dip and hump feature, sharp conductance peaks in IJJ tunneling characteristic rather than peak in SIS junction are seen. The temperature dependence of the energy gap has been also investigated in the study and the values of Δ obtained from both SIS junction and IJJ decreasing with increasing temperature was observed. The gap feature above T_c continues with expression of a pseudo-gap as a characteristic property of HTSs (Ozyuzer, et al. 2005). The strong temperature dependence of energy gap and pseudo-gap feature of Bi2212 superconductor was observed in many studies.
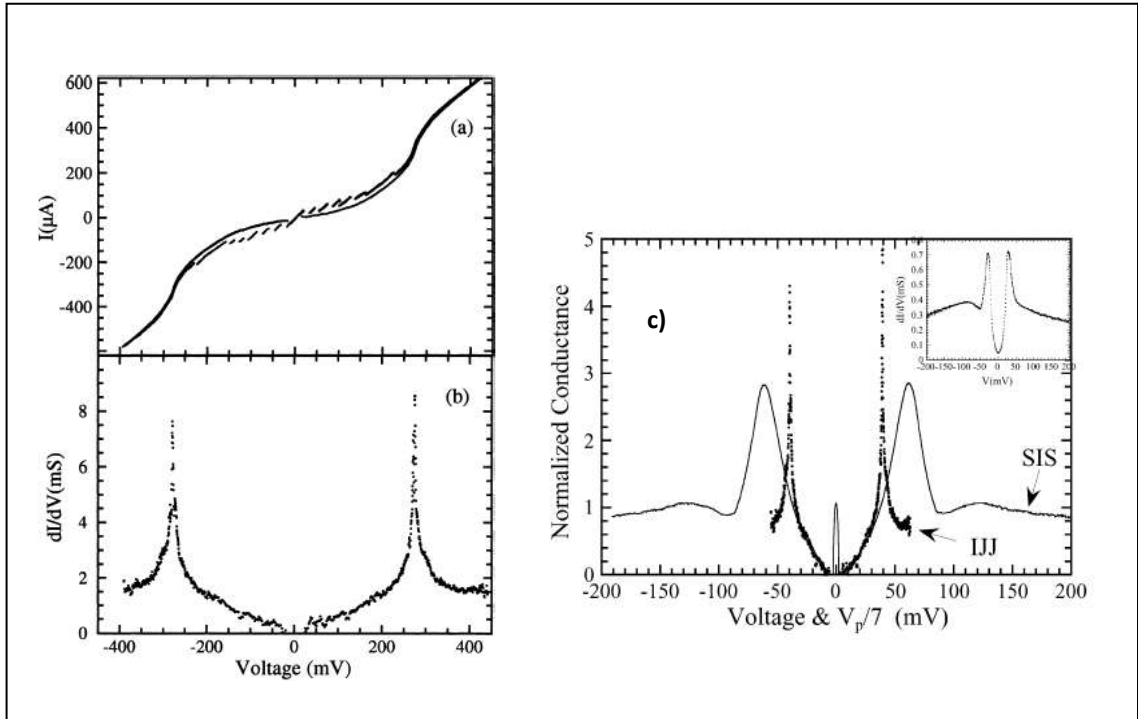
Figure 2.8. Tunneling characteristics of Bi2212 at 4.2 K with quasiparticle branches (a) I-V (b) dI/dV (c) Comparison of normalized conductance of SIS and IJJ (Source: Ozyuzer, et al. 2005)

2.3 Josephson Effect

The most important result of the BCS theory is the postulation of the superconducting energy gap Δ. After the theory of superconductivity was published in 1957, major experimental works was intended to the direct observation of the gap. A very successful method was to study the tunneling of quasiparticles through an insulating barrier (Nicol, et al. 1960, Giaever 1960). The paper explained the tunneling results by using an elegant particle conservation technique which was published by Cohen (Cohen, et al. 1962). Based on this work, Josephson was able to address the tunneling of Cooper pairs instead of normal electrons (Josephson 1973). In his undeveloped work (Josephson 1962); he discovered a phenomenon which soon after was known as the Josephson Effect. To observe the Josephson Effect, the superconductor is cooled until the electrons are bound to one another in pairs, called cooper pairs, because of interactions with phonons. These cooper pairs are very weakly

bound fermions. Two bound fermions are a system with an integer spin, so a cooper pair is a boson and bosons can flow into the same quantum mechanical state and become a superconductor. Josephson predicted that if two superconducting metals are coupled by a thin insulating layer, these cooper pairs could flow across an insulating barrier and then a stationary supercurrent I occur. This is called the **DC Josephson Effect**. This current is present at zero voltage (V=0) and depends on the phase difference $\phi = \theta_2 - \theta_1$ of the superconducting wave functions on both sides of the barrier as

$$I_s = I_c \sin \phi \tag{2.7}$$

The proportionality constant I_c is usually called the critical current. It depends on the properties of the superconducting materials and the barrier. Although the dc Josephson current was already observed (but erroneously attributed to microscopic shorts) in the early tunneling experiments (Nicol, et al. 1960, Giaever 1960), the final experimental confirmation was due to Anderson and Rowell (Anderson and Rowell 1963), one year after Josephson's publication. Ambegaokar and Baratoff (Ambegaokar 1963a, Ambegaokar and Baratoff 1963b) computed the maximum Josephson current I_c as

$$I_c(T) = \frac{\pi}{2e} \frac{\Delta(T)}{R_n} \tanh\left(\frac{\Delta(T)}{k_B T} \right) \tag{2.8}$$

where R is the normal state resistance of the tunnel barrier and $\Delta(T)$ is the temperature-dependent energy gap, as given by the BCS theory. From equation 2.8 follows that at low temperatures, the critical current I_c is related to the normal tunnel resistance R_n as

$$I_c(0) = \frac{\pi}{2e} \frac{\Delta(0)}{R_n} \tag{2.9}$$

where Δ is given in eV.

The dc Josephson current occurs for zero voltage drops between the superconductors. For nonzero voltage, Josephson predicted an oscillating current, where the oscillation frequency is given by

$$\frac{\partial \phi}{\partial t} = \frac{2\pi}{\Phi_0}V,$$ (2.10)

and the current magnitude is otherwise given by equation 2.7. From equation 2.10 we see that a voltage drop of 1mV across the barrier will result in an oscillating current with a frequency of ω=3.035 10^{12} s^{-1} or $f = \omega/2\pi = 483.1\text{GHz}$, manifesting itself by the emission of electromagnetic radiation. This so-called **AC Josephson effect** was first observed in indirect experiments by Shapiro (Shapiro 1963) and directly in the radiation measurements by Giaever (Giaever 1965)

2.3.1 Derivation of the Josephson Equations

Josephson predicted quantum tunneling of cooper pairs through an insulating barrier between two superconductors. Quantum mechanics dictates that the wave function amplitudes of the Cooper pairs will satisfy the following Schrodinger equations on each side of the insulating barrier.

Let us consider two superconducting bulks described by two macroscopic wave functions $\Psi_1(r) = \sqrt{\rho_1}e^{i\theta_1}$ and $\Psi_2(r) = \sqrt{\rho_2}e^{i\theta_2}$, separated by an insulating layer (figure 2.9). Here ρ_1 and ρ_2 denote the density of Cooper pairs in the two bulks and, θ_1 and θ_2 their phases. In the symmetrical case, the material on both sides is assumed to be the same under zero magnetic fields.
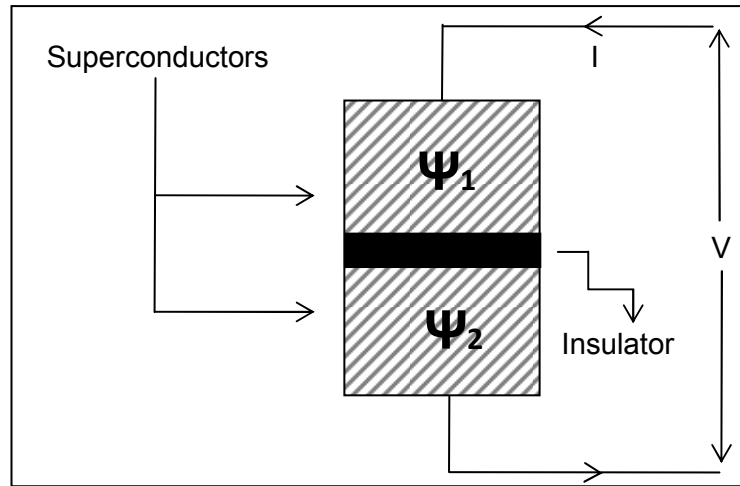
Figure 2.9. Sketch of an S-I-S Tunnel Josephson junction

Josephson predicted quantum tunneling of cooper pairs through an insulating barrier between two superconductors. Quantum mechanics dictates that the wave function amplitudes of the Cooper pairs will satisfy the following Schrodinger equations on each side of the insulating barrier:

$$i\hbar \frac{\Psi_1}{\partial t} = U_1 \Psi_1 + K\Psi_1$$
$$i\hbar \frac{\Psi_2}{\partial t} = U_2 \Psi_2 + K\Psi_2$$

(2.11)

where Ψ is the wave function representing the cooper pairs, U is the potential energy, and K is characteristic of the junction, which couples the two sides of the insulator to each other. Now, assuming zero magnetic fields in the vicinity of the experiment, but an applied voltage V, the potential energy across the barrier is give by

$$U_2 - U_1 = qV$$

(2.12)

If I take the midpoint to be my zero potential, then, plugging in my potentials, my equations are

$$
\begin{aligned}
i\hbar \frac{\Psi_1}{\partial t} &= +\frac{qV}{2}\Psi_1 + K\Psi_1 \\
i\hbar \frac{\Psi_2}{\partial t} &= -\frac{qV}{2}\Psi_2 + K\Psi_2
\end{aligned}
\tag{2.13}
$$

Let me assume that the wave function on each side of the barrier takes the form

$$
\begin{aligned}
\Psi_1(r) &= \sqrt{\rho_1}\, e^{i\theta_1} \\
\Psi_2(r) &= \sqrt{\rho_2}\, e^{i\theta_2}
\end{aligned}
\tag{2.14}
$$

Where ρ is the charge density on each side of the barrier, and θ is the phase of the wave function, which is normally thought of as an unphysical quantity; however, as we shall see, the Josephson effect shows that the phase has a physical effect on the system. So, let me define ϕ to be the difference between the phases

$$
\phi = \theta_2 - \theta_1
\tag{2.15}
$$

Then plugging my wave functions into Schrodinger equations, and equating real and imaginary parts, I get the following set of equations:

$$\dot{\rho}_1 = \frac{2}{\hbar} K \sqrt{\rho_1 \rho_2} \sin \phi$$

$$\dot{\rho}_2 = \frac{2}{\hbar} K \sqrt{\rho_1 \rho_2} \sin \phi$$

$$\dot{\theta}_1 = \frac{K}{\hbar} \sqrt{\frac{\rho_2}{\rho_1}} \cos \phi - \frac{qV}{2\hbar} \qquad (2.16)$$

$$\dot{\theta}_2 = \frac{K}{\hbar} \sqrt{\frac{\rho_1}{\rho_2}} \cos \phi + \frac{qV}{2\hbar}$$

Notice that $\dot{\rho}_1 = -\dot{\rho}_2$, which describes the current which would start flowing between the barriers, such that

$$J = \frac{2K}{\hbar} \sqrt{\rho_1 \rho_2} \sin \phi = J_0 \sin \phi \qquad (2.17)$$

where $J_0 = 2K\rho/\hbar$. Here we assume that the charge density is equal on both sides of the barrier, which is a good physical assumption. By taking the derivative of ϕ we see that

$$\dot{\phi} = \dot{\theta}_1 - \dot{\theta}_2 = \frac{qV}{\hbar} \qquad (2.18)$$

which, after integrating over time, is given by

$$\phi(t) = \phi_0 + \frac{q}{\hbar} \int V(t) dt \qquad (2.19)$$

Note that because we are talking about cooper pairs tunneling through, the charge, q, is given by

$$q = 2q_e \qquad (2.20)$$

Now, if we supply zero voltage, V=0, we see that $\phi = \phi_0$, which is a constant. Plugging into our expression for $J = J_0 \sin\phi$, we see that the current is a constant. So, with no voltage drop, we see a constant current, which has a maximum value of $J_0 = 2K\rho/\hbar$. This is exactly the DC effect that Josephson predicted. Now, instead, let's apply a voltage

$$V = V_0 + v\cos(\omega t) \qquad (2.21)$$

where v << V_0, and ω is very large, which is a large DC voltage with a high frequency, small amplitude AC voltage superimposed. Then

$$\phi = \phi_0 + \frac{q}{\hbar}V_0 + \frac{qV}{\hbar\omega}\sin(\omega t) \qquad (2.22)$$

Using the approximation that

$$\sin(x + \phi x) \approx \sin x + \phi x \cos x \qquad (2.23)$$

we get an expression for our current that looks like

$$J = J_0 [\sin(\phi_0 + \frac{q}{\hbar}V_0 t) + \frac{qv}{\hbar\omega}\sin(\omega t)\cos(\phi_0 + \frac{qV_0 t}{\hbar})] \qquad (2.24)$$

The first term will time average to zero, since $\hbar$ is so small and, therefore, the frequency is so large. The second term will also go to zero unless ω is tuned such that

$$\omega = \frac{q}{\hbar}V_0 \qquad (2.25)$$

Then using the trigonometric identity that

$$\sin a \cos b = \frac{1}{2}[\sin(a+b) + \sin(a-b)] \qquad (2.26)$$

we see that

$$J = J_0 \frac{v}{2V_0}[\sin(\phi_0 + \frac{2qV_0 t}{\hbar}) + \frac{qv}{\hbar\omega}\sin(\phi_0)] \qquad (2.27)$$

Again, the first term will be time averaged to zero due to its high frequency, but the second term is constant, such that

$$J = \frac{K\rho v}{V_0 \hbar}\sin\phi_0 \qquad (2.28)$$

which is a constant. This is the cause of the Josephson AC effect. It is predicted that the

I-V plot of this current will be a series of steps, each with a width of $\frac{q}{h} = \frac{2e}{h}$. So this

experiment gives a precise measurement of ratio of e to h.

2.4. THz Waves Generation from Bi$_2$Sr$_2$CaCu$_2$O$_{8+\delta}$

Recently many people at science and technology are interested in the electromagnetic waves in terahertz (THz = 10^{12} Hz) frequency range (0.1-10 THz) because of their important application areas including physics, biology, chemistry, astronomy, medicine etc… Electromagnetic waves with frequency below and above the THz frequency range are widely generated by semiconducting electronics based on high-speed transistors and the photonics based on the semiconducting laser respectively. However, in this frequency range there are still lacks of THz sources and difficulties in its generation although their functional advantages in many application areas entail the evolution of the THz sources in science (Bae and Lee 2006).

Recently, the research on THz radiations sources with high power, low cost and portable has been increasing. Since they are planned to use in technological areas, they should be continuous, coherent and frequency tunable as well. Therefore the research has gone towards the novel THz sources which include technology of HTSs layered structure. One of the several reasons making HTSs suitable candidate for the generation of THz radiation is their layered structure which enables the propagation of electromagnetic wave by unique excitation called Josephson plasma oscillations and frequency of the Josephson plasma is between THz ranges (Tachiki 1994).

Since the Josephson plasma frequencies of high T_c cuprates range from subterahertz to 10 terahertz region, which lie in the terahertz gap region, the possibility of the terahertz EM wave emission from intrinsic Josephson junctions (IJJ's) has been discussed for a long time, more than a decade by various authors. So far mostly radiation from the flux flow of the Josephson vortices was discussed in the literature. The inductive interlayer coupling typically promotes formation of the triangular vortex lattice. However, to generate noticeable outside radiation oscillations induced by the

moving lattice have to be in phase in different layers, which is realized only if the moving vortices form a rectangular lattice. No regular way to prepare such a lattice is known at present. In addition, it seems to be unstable in most of parameter space (Artemenko and Remizov 2000). A. E. Koshelev suggest that the synchronization of the Josephson oscillations by radiation field in the simplest case, as dc magnetic field is not applied and only radiation itself introduces the in-plane phase gradients (Bulaevskii and Koshelev 2007). The emission from a single junction is weak, so many such junctions emitting in phase at the same frequency can produce useful emission power. Stacks of junctions with unsurpassed packing density occur naturally in the layered high-temperature superconductor $Bi_2Sr_2CaCu_2O_{8+\delta}$. This material composed of superconducting CuO-layers that are coupled through the intrinsic Josephson Effect (Kleiner, et al. 1992), can sustain high voltages across the junctions and holds the potential for very intense, coherent radiation that covers the THz gap. However, the mainly requirement for the producing useful radiation from Bi2212, namely achieving synchronization of the high-frequency oscillations of all the junctions in the stack, has so far been a major challenge preventing the realization of this potential. Numerous approaches for synchronizing the junctions have been considered, such as applying a magnetic field to induce coherent Josephson vortex flow (Irie, et al. 1998) or inserting the BSCCO crystal into a microwave cavity (Madsen, et al. 2004). However, the far-field radiation power obtained from BSCCO is limited to the pW range (Batov, et al. 2006).

Ozyuzer et al. show that THz radiation power in the μW range can be produced using a method by which the phase of the emission from the atomic scale Josephson junctions in BSSCO is synchronized by a standing electromagnetic wave that is formed by multiple reflections in the cavity formed by the side surfaces of the crystal, exactly as in a laser. Electromagnetic waves inside a BSCCO crystal propagate as Josephson plasma modes (Kleiner, et al. 1994), which resemble the guided modes in an optical waveguide. The average electric field on the side surfaces cancels in all but the in-phase mode, so only this mode produces noticeable emission (figure 2.10a and b).
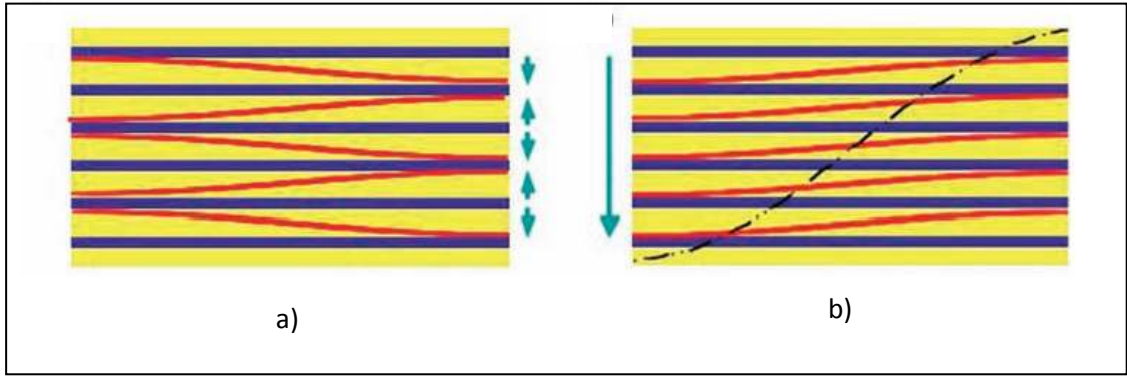
Figure 2.10. Schematics of the anti-phase (a) and of the in-phase (b) mode. The blue and yellow layers are the CuO layers and Bi-Sr-O layers. The red waves represent the alternating electric field. In the anti -phase mode the electric field on the long side face largely cancels, resulting in negligible emission. For the in-phase mode, the electric fields from each junction add to create an intense standing wave (black dashed line) and strong emission (Source: Ozyuzer, et al. 2007)

Resonances that occur on the long dimension of the mesa incur sign changes of the electric field on the long side faces and do not contribute to the emission in a substantial way. In the in-phase mode, the coherent superposition of the electromagnetic waves from each junction creates a macroscopic coherent state in which the radiation power increases as the square of the number of junctions.

The general mechanism of the experiment of Ozyuzer et al. for the emission of THz radiation is as follows. When an external current is applied along the c axis, the ac Josephson current in the resistive state excites a cavity resonance mode of Josephson plasma wave in the sample. The excited standing wave of Josephson plasma is converted to a terahertz em wave at the mesa surfaces and the em wave is emitted into the vacuum space (figure 2.11).
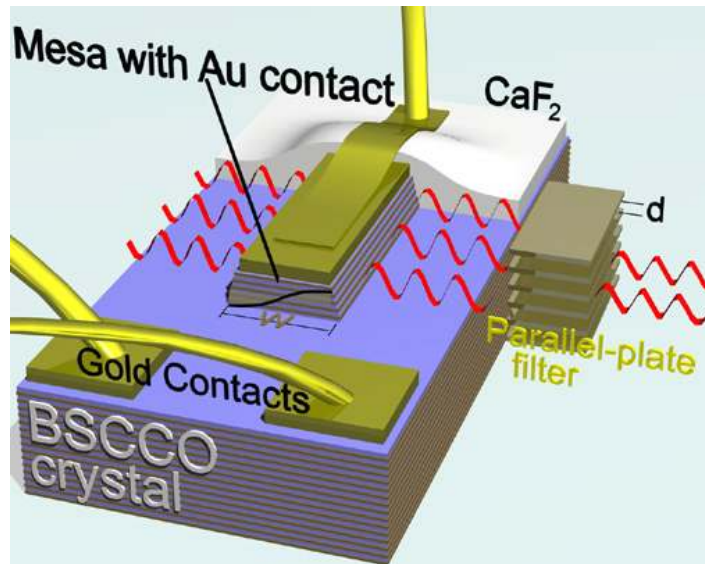
Figure 2.11. Our schematic of mesa and electrical contacts on Bi2212 for emission of THz radiation (Source: Ozyuzer, et al. 2007)

Ozyuzer et al. report in the Science letter that more than 500 junctions can be made to oscillate in phase, producing continuous wave coherent radiation power up to ~0.5 μW at frequencies up to 0.85 THz. The available power is potentially much larger, because there is evidence that 20 μW of power are pumped into the observed THz cavity resonance. The emission persists up to temperatures of ~50 K. In contrast to previous studies, emission does not require the application of a magnetic field, considerably simplifying the design of superconducting THz sources. In fact, a single applied dc current leads to the efficient excitation of continuous coherent THz radiation. Their experimental results (Ozyuzer, et al. 2007) are summarized as follows;

- The mesa samples have an in-plane area of 40–100 μm x 300 μm and a thickness of ~1 μm; that is, the in-plane dimensions are on the order of λ_c, the c-axis magnetic penetration depth, which is the length scale of the transverse Josephson plasma, and the mesas contain 600–700 intrinsic junctions.
- The strong emission is observed first near the unstable point of the retrapping current in the uniform voltage branch as the bias current is decreased below the critical current I_c.

- The emission is also observed in the other branches when the bias current is further decreased below the transition points to lower branches. In this case the power of emitted electromagnetic waves is proportional to N^2, N being the number of junctions in the voltage state, indicating that the coherent emission takes place.

- The emitted EM waves are highly monochromatic ones.

- The emitted power is ~0.5 µW, which is much stronger compared with the emission from the single-junction systems (~pW) (Langenberg, et al. 1965).

The bolometric measurements were obtained while simultaneously recording I-V measurements through c-axis of Bi2212. When bias voltage decrease, radiation power is detected by bolometer. In order to distinguish electromagnetic wave from thermal radiation, they used polarize property of THz emission. On the other hand thermal radiation peaks were detected by bolometer because of heating of mesa at the highest currents. Moreover, if Bi2212 single crystal has high critical current value, heating effect at high current occurs and blocks the emission from mesa. Also large mesa area they used is a different reason to heat superconducting mesa. To solve this problem they used Bi2212 with low critical current value.

In this study (Ozyuzer, et al. 2007), depending of emission frequency on mesa dimensions was demonstrated and obtained results are very agreement with frequency of fundamental cavity resonance. This frequency is given by,

$$f = \frac{c_0}{2nw} \tag{2.9}$$

where w is width of mesa and n is refractive index of Bi2212. The maximum frequency that is 0.85 THz was obtained from mesa whose width of 40 µm. Number of IJJs is corresponding to emission power of radiation because emission power from one individual IJJ is very low. It is emphasized that power is proportional with the square of the number of coherently oscillation of IJJ. Therefore mesas with high thickness were fabricated (Ozyuzer, et al. 2007).

After the Ozyuzer et al. work, of course, many questions remain open, such as whether different cavity modes can be excited (to increase the accessible frequency range and tunability of a given sample), what their stability might be, and the precise mechanism of excitation. The experiment by Ozyuzer et al. will clearly stimulate the field, and interesting results are sure to follow, possibly filling the terahertz gap (Kleiner 2007).

For the high power emission of THz waves, both experimental and theoretical studies have been improved. Recently, Hu (Hu and Lin 2008), Lin (Lin and Hu 2008), and Koshelev (Koshelev 2008) proposed the following new mechanism. When the inductive interaction between the superconducting CuO layers in BSCCO is strong, static kink structures arise in the phase difference of superconducting order parameter between the superconducting layers. The phase kinks induce cavity resonance modes of the Josephson plasma. This is a new dynamic state caused by the nonlinear effect special in the IJJ system. However, details of the mechanism have not yet been clarified, although it is important for designing the terahertz em wave emitters with use of IJJ.

CHAPTER 3

EXPERIMENT

3.1 Motivation

High temperature superconducting $Bi_2Sr_2CaCu_2O_{8+\delta}$ (Bi2212) single crystals have natural junctions called intrinsic Josephson Junctions (IJJs). They play an important role for generation of THz radiation when a static voltage applied along the c-axis of Bi2212 (ac Josephson effect) (Ozyuzer, et al. 2007). Generation of powerful THz radiation requires mesas with large lateral dimension but there are difficulties in fabrication of perfect rectangular mesa. It should be close to 90 degrees to obtain IJJs with same planar dimensions for synchronization of IJJs (Koshelev 2008). The main purpose of our work is fabrication of mesas by using single layer mask (PR) and two different multilayer masks, which are Ta/PR and PR′/Ta/PR for the generation of THz radiation. Thick photoresist layer (single layer mask) shades the lateral dimension of mesa during ion beam etching. Therefore, we patterned multilayer mask on Bi2212 and used selective ion etching as in Nagai et al. works (Nagai, et al. 1991) overcome this problem. In this purpose, mesas fabricated by various experimental processes are anticipated to have smooth rectangular prism shape with large area, high thickness and lateral angle which are related to capability of emitting THz rays. Moreover, the surface and electrical characterizations of the mesas are important for our study. Atomic Force Microscope (AFM), Profilometer and Scanning Electron Microscopy (SEM) were used to analyze mesa height, the lateral angle of the mesa and thickness of the gold layer. In electrical characterizations including R-T and I-V measurements along the c-axis of Bi2212 crystal, the electrical behaviors proper to layered structure of HTSs were investigated. In the bolometer measurements, detection of the emission from the long

edge of the mesa was investigated by using Si Bolometer. In this chapter, all of experimental processes will be described including, the crystal growth, experimental techniques, mesa fabrication and the characterization methods step by step.

3.2 Growth of Bi2212 Single Crystals

There are many processes in production of the Bi2212 superconductor which include such as sintering and melting the superconductor compounds. Although the fabrication of HTSs by sintering process is easy, this method is only preferred for the bulk HTSs and these superconducting materials have porous structure and random arrangement of superconducting grains. Therefore it is difficult to obtain a smooth structure including the uniform orientation of the superconducting crystal completely on the bulk HTSs (Michishita, et al. 1996). In order to produce the layered HTSs with the high quality and c-axis aligned structure, the researchers use the melting processes including the KCl flux method (Katsui 1988), vertical Bridgman method (Ono, et al. 1988) self-flux method (Shishido, et al. 1989, Tanaka, et al. 2001), melt-textured growth method (Jin, et al. 1988), the laser-heated pedestal growth method (Feigelson, et al. 1988) and travelling solvent floating zone method (TSFZ) (Takekawa, et al. 1988)

3.2.1 Self-flux Method

Bi2212 single crystals were grown by the self-flux method using an alumina crucible with a cap. Starting powders (Bi_2O_3, $SrCO_3$, $CaCO_3$, CuO) were weighed in the atomic ratio of Bi: Sr: Ca: Cu = 2:2:1:2, and elaborately ground and mixed in an agate mortar with a pestle, then placed into an alumina crucible. First, we calcinated the grinded powders at 800 °C for 51 h. The aim of the calcination process is to discharge the carbon in raw materials of $SrCO_3$ and $CaCO_3$ as CO_2. After the calcination process, we reground the powders, and then calcined powders put into the alumina crucible. In

order to control the pressure in the crucible, shaped die steel was set on the cap of the crucible to apply 250 g load. Although this is a basic method, we can easily change the pressure in the crucible. Then, the crucible with an alumina cap was placed in an electric furnace. The Bi2212 single crystal growth process and heat treatment program are shown in figure 3.1. In the heat Treatment program, the alumina crucible is rapidly heated in a furnace to 960 °C, and then maintained at 960 °C for 10 h. Then, it is slowly cooled down to 800 °C at a rate of 1 °C/h, and subsequently cooled at 20 °C/h to the room temperature (Koseoglu, et al. 2009).

There is also another process for the growth of single crystal in the self flux, we used, In this process, Bi_2O_3, $SrCO_3$, $CaCO_3$, CuO were weighed in the atomic ratio of Bi:Sr:Ca:Cu = 2:2:1:2 again and then put in to the alumina crucible as seen in the figure 3.2. After that, the crucible was placed in an electric furnace. The growth process and used heat treatment program of the electric furnace is shown in the figure 3.2. The alumina crucible is rapidly heated in a furnace to 990 °C, and then maintained at 990 °C for 10 h. Then, it is slowly cooled down to 790 °C at a rate of 1 °C/h, then cooled down to 590 ° C at a rate of 40 ° C/h and finally subsequently cooled at 20 °C/h to the room temperature. The optical image of the broken crucible is like that (Koseoglu, et al. 2009).
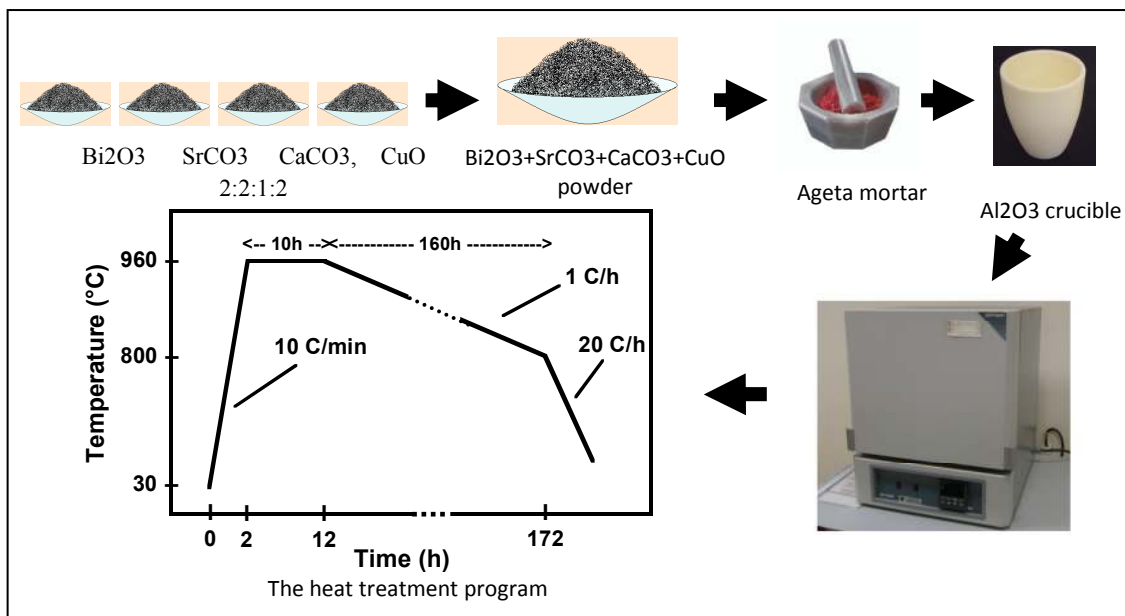
Figure 3.1. Bi2212 single crystal growth process and heat treatment program
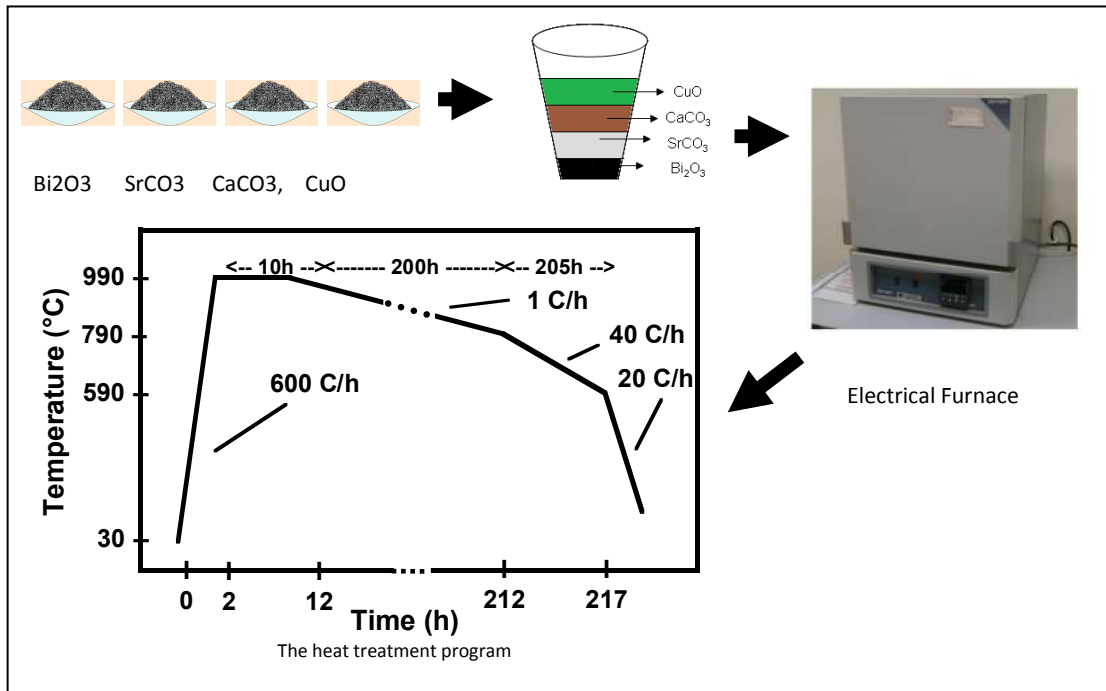
Figure 3.2. Another Bi2212 single crystal growth process and heat treatment program

After the growth, the crystals were separated by carefully shattering the alumina crucible for measurement of the superconducting properties. Plate like Bi2212 single crystals were harvested from the grown crystals with a razor blade and the edge of the crystal was cut with the size of 2x2 mm^2 by a razor blade. Then, we cleaved the single crystal with Scotch tape, as observed under the optical microscope. Figure 3.3 shows the optical image of the broken crucible. As seen in the figure, the plate-like single crystals grown around a center of the crucible.
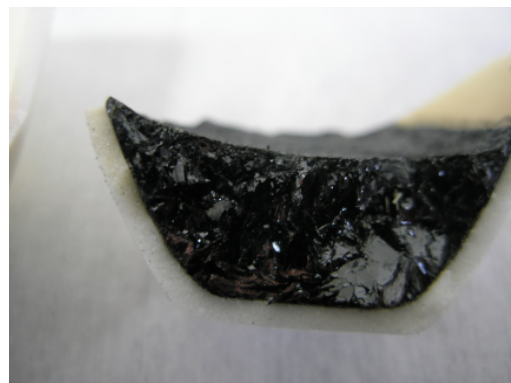
Figure 3.3. Optical photo of broken crucible

In figure 3.4, X-ray diffraction (XRD) patterns of the grown crystals by self flux method and TSFZ method were shown. The sharp (00l) peaks in the XRD results of the crystals grown by self-flux are assigned to Bi2212 superconductor phase. As we compare the XRD peaks of the crystals grown by self-flux and TSFZ method, they have same (00l) peaks. But there are some unidentified peaks in the figure.
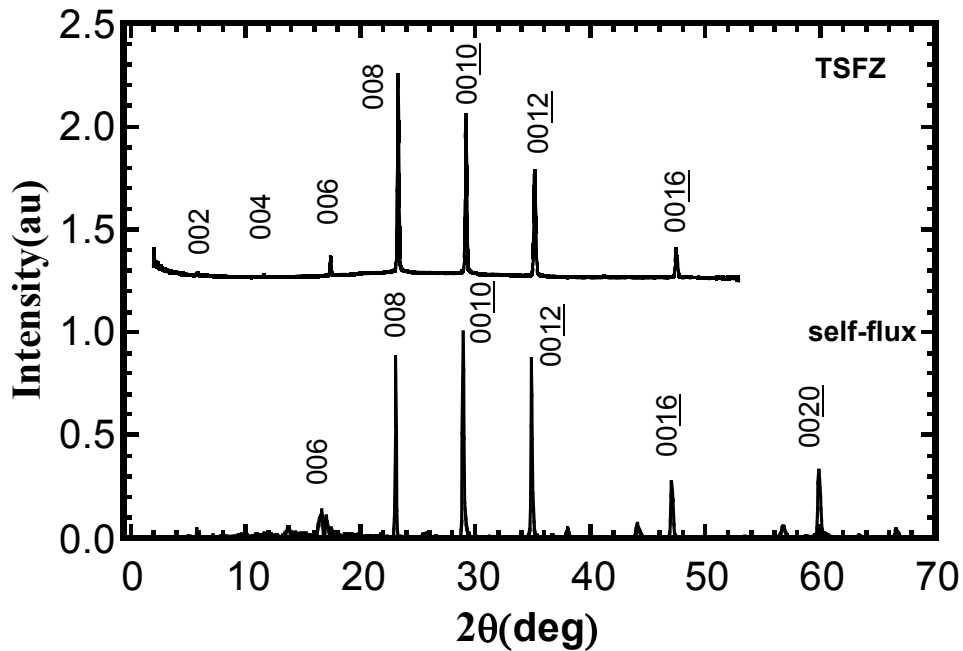
Figure 3.4. X-ray (00l) diffraction patterns of Bi2212, TSFZ data are obtained from Kurter M.Sc. Thesis 2005

3.2.2 TSFZ Method

The high quality single crystals of Ca-rich Bi2212 are used in our studies. We have prepared it from D.G. Hinks at Argonne National Laboratory, and also we grow by self flux method at IZTECH. Hinks 's crystals were grown by the traveling solvent floating zone method and in order to obtain underdoped Bi2212 superconductors the single crystals can be annealed in argon gas flow (Ozyuzer, et al.2003).

The traveling solvent floating zone (TSFZ) method which is one of the melt processes is used to obtain high quality single crystal of HTS. During the process the

layered superconducting structures with high purity are fabricated without contamination, because it is a crucible-free technique and compounds are heated by IR radiation in optical system. Growth of better crystals with large size dimensions and uniform aligned structure than the bulk structure of this materials is the most important property of the fabricated materials by the TSFZ. For anisotropic electrical measurements, it is very important to fabricate a smooth uniform structure (mesa) with required sizes on the growth materials, so the perfect crystals are preferred. It makes TSFZ very important in superconducting devices (Michishita, et al. 1996).

This technique generally includes an optical system focusing the light emitted by halogen lamp to the melting zone in the image furnace. Since the superconducting compounds are only heated by focusing light, there is no other material used near the melting zone in order to conduct the heating to compounds. Experimental configuration including two ellipsoidal reflectors and halogen lamps are seen in figure 3.5 (Revcolevschi and Jogoude 1997).
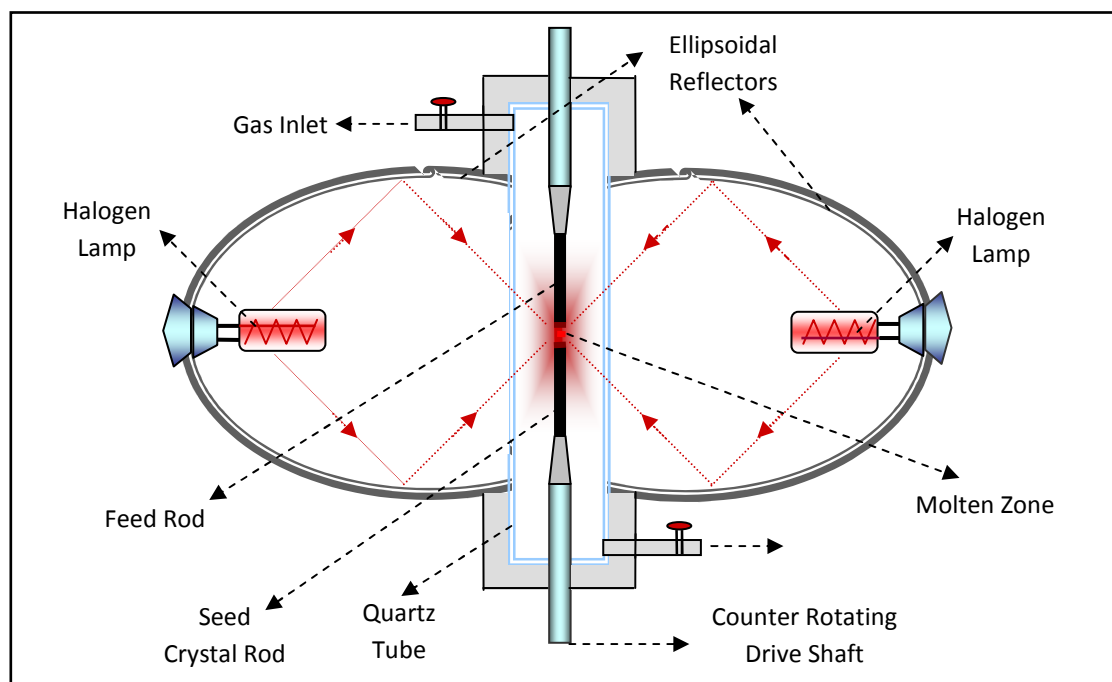
Figure 3.5.   Double ellipsoid image furnaces for crystal growth with floating zone method (Source: Simsek 2008)

Two halogen lamps located at one of the two focal points of the each ellipsoid chamber emit radiations that are focused by ellipsoidal reflectors to the other common focal point of each ellipsoid in which is molten zone. Before the floating zone process, by using calcination and sintering processes, the superconducting bulk material formed as a rod is prepared. To use as the feed and seed crystal rods in ellipsoidal furnace, the superconducting rod is divided into two pieces. Then they are coaxially mounted inside the quartz tube and their junction is in the center of the common focus point of each ellipsoid. The junction of two rods which is in molten zone which is heated by halogen lamps so they begin to melt. By obtaining refractory oxide single crystals, the rods are moved downwards at fixed speed. Thus superconducting crystal is solidified with unidirectional growth. During the growth, feed rod and seed crystal rods are rotated to obtain the homogeneous aligned crystal structure. The superconducting layered single crystal rod with Bi2212 phase whose growth direction is parallel to [110] a-b plane is obtained at the end of the TSFZ. The crystals have not only a layered structure with a-b alignment along to growth direction but also c-axis alignment in the transverse section. The crystal growth in the quartz tube is performed in O_2 gas flow to supply oxygen to crystal. The pressure of O_2 is used as one of the growth parameters since it is affected the growth temperature and stabilization of the molten zone (Michishita, et al. 1996).

3.3 Experimental Techniques

My thesis is about fabricating Bi2212 mesa with 1 μm height and high lateral angle, and THz radiation from the fabricated mesa. So, there are some used experimental techniques in my thesis such as Thermal Evaporation, Metal Deposition by DC Magnetron Sputtering, Optical Photolithography and Reactive Ion Beam Etching. After the fabrication we characterized the mesas by electrical (R-T and I-V) and bolometric measurements, which their detail will be given in section 3.4.

3.3.1 Thermal Evaporation

The vacuum thermal evaporation deposition technique consists in heating until evaporation of the material to be deposited. The material vapor finally condenses in the form of thin film on the substrate surface and on the vacuum chamber walls. Usually low pressures are used, about 10^{-6} or 10^{-5} Torr, to avoid reaction between the vapor and atmosphere. At these low pressures, the mean free path of vapor atoms is the same order as the vacuum chamber dimensions, so these particles travel in straight lines from the evaporation source towards the substrate. This originates 'shadowing' phenomena with 3D objects, especially in those regions not directly accessible from the evaporation source. Besides, in thermal evaporation techniques the average energy of vapor atoms reaching the substrate surface is generally low (order of kT, i.e. tenths of eV). This affects seriously the morphology of the films, often resulting in a porous and little adherent material. In thermal evaporation techniques, different methods can be applied to heat the material such as, resistance heating (Joule effect) or bombardment with a high energy electron beam, usually several KeV, from an electron beam gun (electron beam heating).

Schematic of our vacuum thermal evaporation system can be seen in the figure 3.6. It provides to obtain gold layer without damaging to Bi2212 surface. This technique includes evaporation of the material in filament boat heated by high current source and re-condensation of the material with vapor state onto cooler substrate. Generally it needs high temperatures to evaporate the material and in our system it is carried out by passing large current through the filament boat. The value of the current necessary for evaporation temperature changes with respect to filament boat resistance (its sizes). It is between 190 and 200 A for our filament boat. Deposition and thickness of film on the substrate are controlled by shutter and it also provides to get good quality thin films which have not contamination coming from other materials in the boat at the starting of evaporation. Moreover, for the good quality film evaporation should be done in vacuum around 10^{-6} Torr. In order to reach high vacuum, turbo molecular pump with back pumping is used in our system. Thickness of the deposition is measured by thickness monitor and shutter is closed when required thickness reaches. The thickness monitor

was calibrated for gold (Au) and the evaporated thickness of the gold film is twice of the thickness monitor screen value, seen in the figure 3.7.
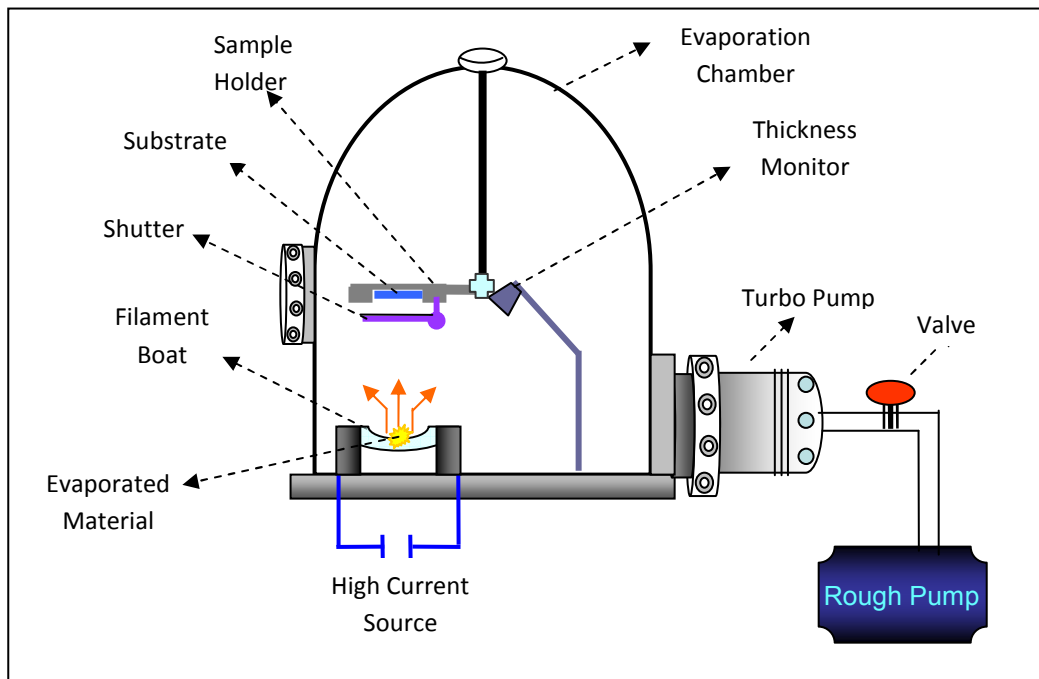
Figure 3.6. Schematic representation of our vacuum thermal evaporation system
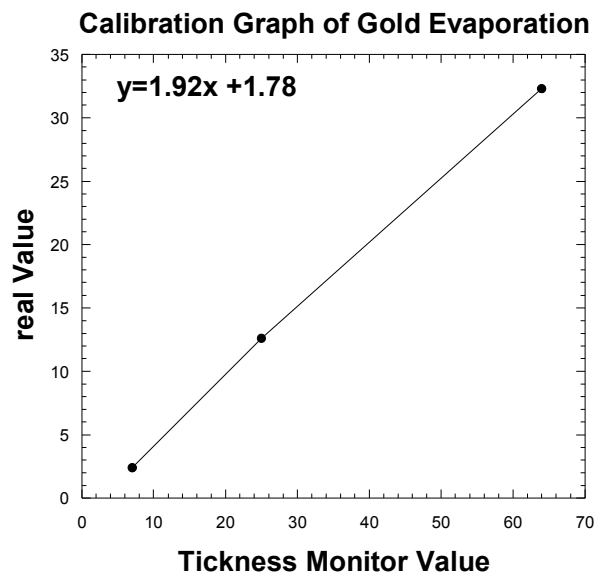
Figure 3.7. Calibration graph of the gold evaporation

3.3.2 Metal Deposition by DC Magnetron Sputtering

In dc magnetron sputtering the cathode (to which the target material is attached) is held at a large negative voltage relative to the substrate and walls of the chamber. Argon plasma is ignited in the chamber by field emission of electrons from the cathode. The magnetron (a configuration of magnets situated underneath the target) serves to confine electrons close to the target surface, thereby increasing ionization in this region (Figure 3.8). Positively charged Ar ions are then accelerated towards the cathode, dislodging atoms from the target and leading to the build up of a thin film on the substrate (Figure 3.9).
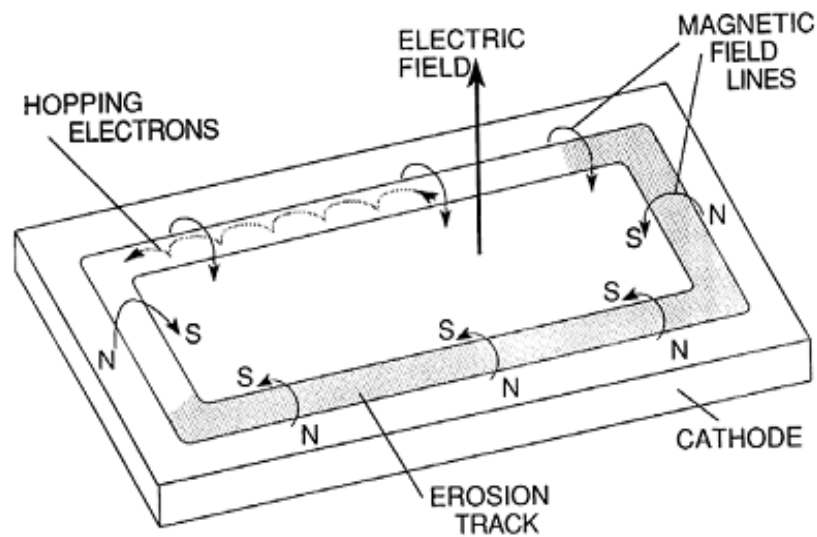
Figure 3.8. Applied field and electron motion in the planar magnetron
(Source: Ohring, 2001)
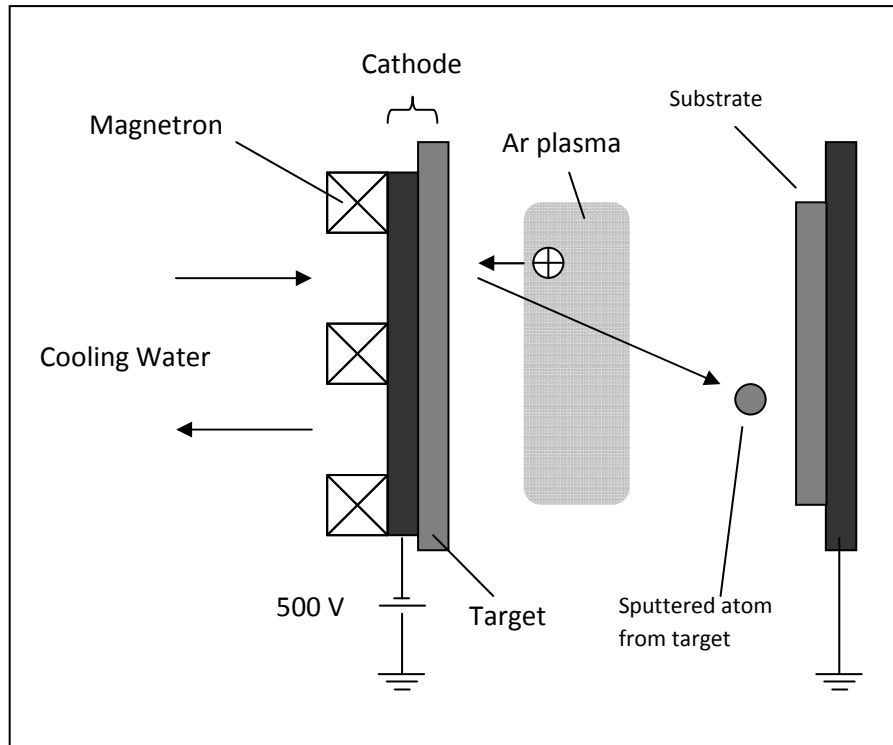
Figure 3.9. Schematics of the DC magnetron sputtering process

In figure 3.10, a new magnetron sputtering head configuration is shown. E field is created between shield and target material. Rare magnets create the constant magnetic field. The bias voltage is not used. This configuration is used in our magnetron sputtering system.
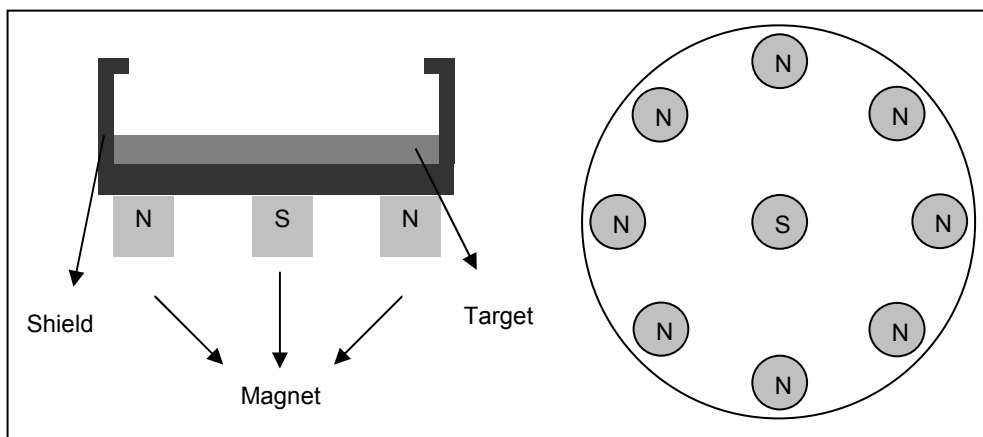
Figure 3.10. A view of magnetron sputtering configuration

Magnetron sputtering system that is used in experiment is a High-Vacuum system shown in figure 3.4. A rough pump and a turbo molecular pump (TMP) were used to approach a high vacuum region. To measure base pressure of the system, a thermocouple and a cold cathode gauge were used. Magnetron sputtering system has 4 guns with a water cooling channel, gas entrance and power connections. To measure pressure of the vacuum chamber during the deposition, a MKS type Baratron was used. Gas flow was controlled by a MKS mass flow controller. A gate valve with a stepper motor was connected to the system in front of TMP. An Advanced Energy dc Power supply was used. The figures 3.11 and 3.12 represent the picture of used magnetron sputtering system in our thin film laboratory and schematic of the magnetron sputtering system.

Figure 3.11. Picture of the magnetron sputtering system
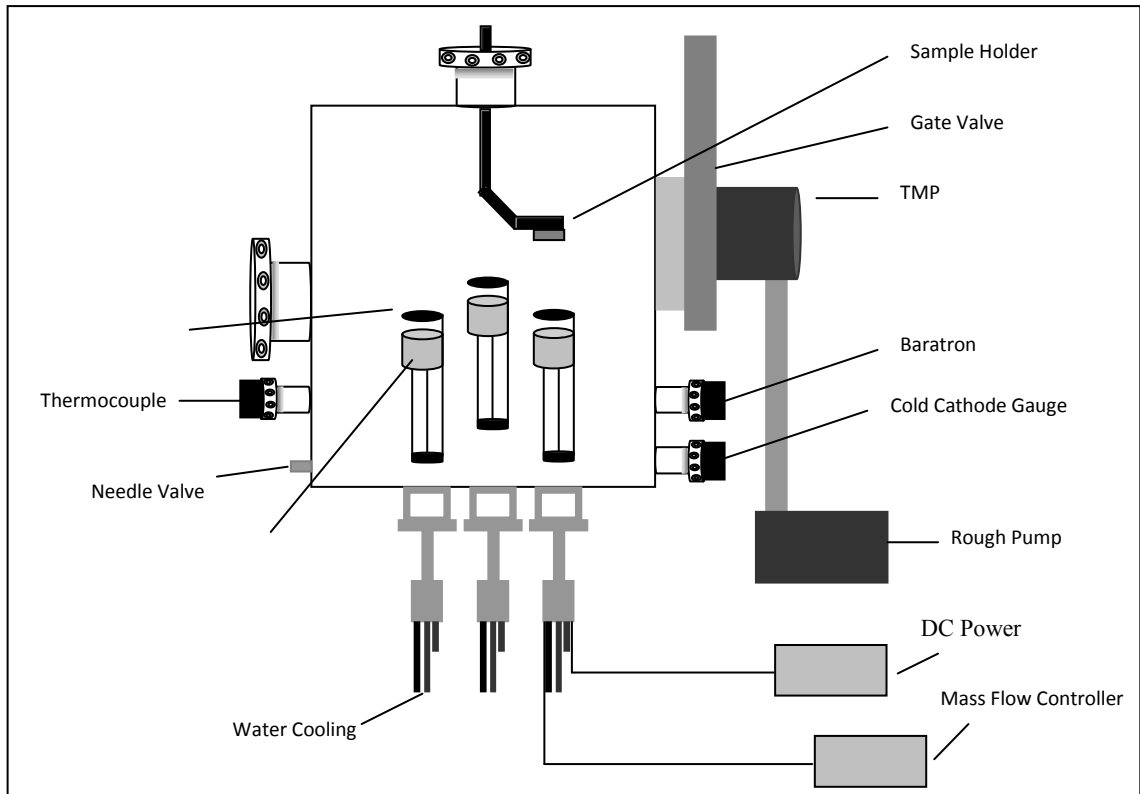
Figure 3.12. Schematic of the Magnetron Sputtering System

System was pumped by using two different vacuum pumps, these are rough pump (below to 10^{-3}Torr) and a TMP (below 10^{-6}Torr). The base pressure was below 2.0×10^{-6}Torr. Ar gas (purity 99.99%) was used as an inert gas. After reached to base pressure, 40 sccm Ar gas was flowed to the chamber by using a mass flow controller. At the beginning of my thesis, firstly deposition rate of Ta is determined using the Argon ions. Deposition rate of Ta is 9.3 nm per minute (Figure 3.13).

Depositions were done in two steps, the first one is a pre-sputtering step and the second one is a thin film deposition step. To remove contamination of target surface a pre-sputtering step was performed. In this process, during the 5 minutes pre-sputtering, the shutter of the magnetron sputter head was closed. Then, shutter was opened and the deposition of Ta film on to the sample continues 8 minutes and 34 seconds for the 80nm Ta deposition at room temperature. The deposition parameters are shown in the table 3.1. Substrate distance from the target surface was constant for all experiments. After deposition steps, the pressure of the chamber was reached to atmosphere pressure to remove the substrate holder from the chamber.

Table 3.1. Ta deposition parameters

Power Supply	20 W – 339 V – 54 mA
Gas Flow	40 sccm Ar
Baratron	3.24 mTorr
Valve Position	100% Open

Calibration Graph of Ta Sputtering

y=9.16x +1
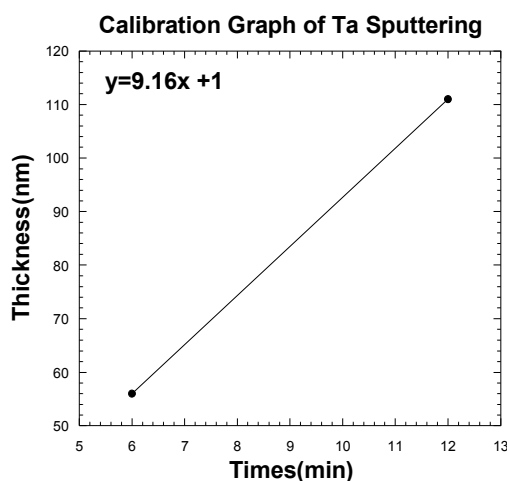
Figure 3.13. Calibration graph of DC Magnetron sputtering of Ta

3.3.3 Optical Photolithography

Optical lithography is a process used in microfabrication to selectively remove parts of a thin film or the bulk of a substrate. It uses light to transfer a geometric pattern from a photo mask to a light-sensitive chemical photoresist, or simply "resist" on the substrate. A series of chemical treatments then engraves the exposure pattern into the material underneath the photoresist. In a complex integrated circuit for example, modern CMOS, a wafer will go through the photolithographic cycle up to 50 times.

Optical lithography shares some fundamental principles with photography, in that the pattern in the etching resist is created by exposing it to light, either using a projected image or an optical mask. This step is like an ultra high precision version of

the method used to make printed circuit boards. Subsequent stages in the process have more in common with etching than to lithographic printing. It is used because it affords exact control over the shape and size of the objects it creates, and because it can create patterns over an entire surface simultaneously. Its main disadvantages are that it requires a flat substrate to start with, it is not very effective at creating shapes that are not flat, and it can require extremely clean operating conditions.

Since PR is sensitive to light, these processes are done in dark room and the typical procedure for photolithographic patterning was as follows:

❖ Sample was placed on the resist spinner and covered with 3 drops of AZ 1505 photoresist using a pipette.

❖ The spinner was rotated at 4.5 V by using power supply for 25 s giving a 1.5 µm layer of resist.

❖ The sample was removed from the spinner chuck and baked to harden the photoresist at the 90°C in the drying oven for 30 minutes.

❖ The edges of the sample exposed with UV light in the homemade mask aligner for 15 seconds using a removal mask.

❖ The exposed resist was developed away in a solution of developer of sodium hydroxide (NaOH) with concentration of 0.2 M (development time ~25 s). The sample was then rinsed in distilled water and dried with flow of N_2, then inspected under yellow light in an optical microscope.

❖ Finally, the mesa shaped patterned samples were exposed UV light for 10 seconds for the blanket exposure and hard baked at the 115°C in the drying oven for 40 minutes, which solidifies the remaining PR to make more durable layer for the reactive ion beam etching.

❖ If the results were unsatisfactory the resist was removed with acetone and the process repeated.

3.3.4 Reactive Ion Beam Etching

To pattern the mesa or micro fabrication in the other research field, there are well known two processes such as, wet and dry etching. Disadvantage of wet etching is the undercutting caused by the isotropy of the etching. The purpose of dry etching is to create an anisotropic etching. It means that the etching is unidirectional. An anisotropic etching is critical for high-fidelity pattern transfer.

Instead of End Hall type ion beam etching system that was used in our earlier works, we designed new ion beam etching system which is requiring low volume vacuum area, operate in low vacuum value (10^{-2} Torr) and has sample holder-source distance that is suitable for ion beam source standard, in order to obtain high etching rate. New ion beam etching source is cold cathode type. The picture and top view schematic of new ion beam etching system is shown in figure 3.14 and 3.15.

The comparison between the etching rates and parameters of old ion beam system and new ion beam system can be seen in table 3.2 and 3.3. Our earlier studies showed us the etching rates of Au and Bi2212 are nearly same so as it can be seen in the tables we used etching rate of Au instead of Bi2212. The reason of why we found etching parameters of Ta in these tables is that it was used to form mesa with another material, apart from the photoresist (PR), which was used for the patterning the mesas. The thickness of photoresist is high and its edges are not smoothly perpendicular so during the etching, the edges of etched shape are like the curvature edges of mesa. Hence the smooth rectangular shape is not obtained. Furthermore, photoresist is etched with ions rapidly.

Figure 3.14. The image of our ion beam etching system
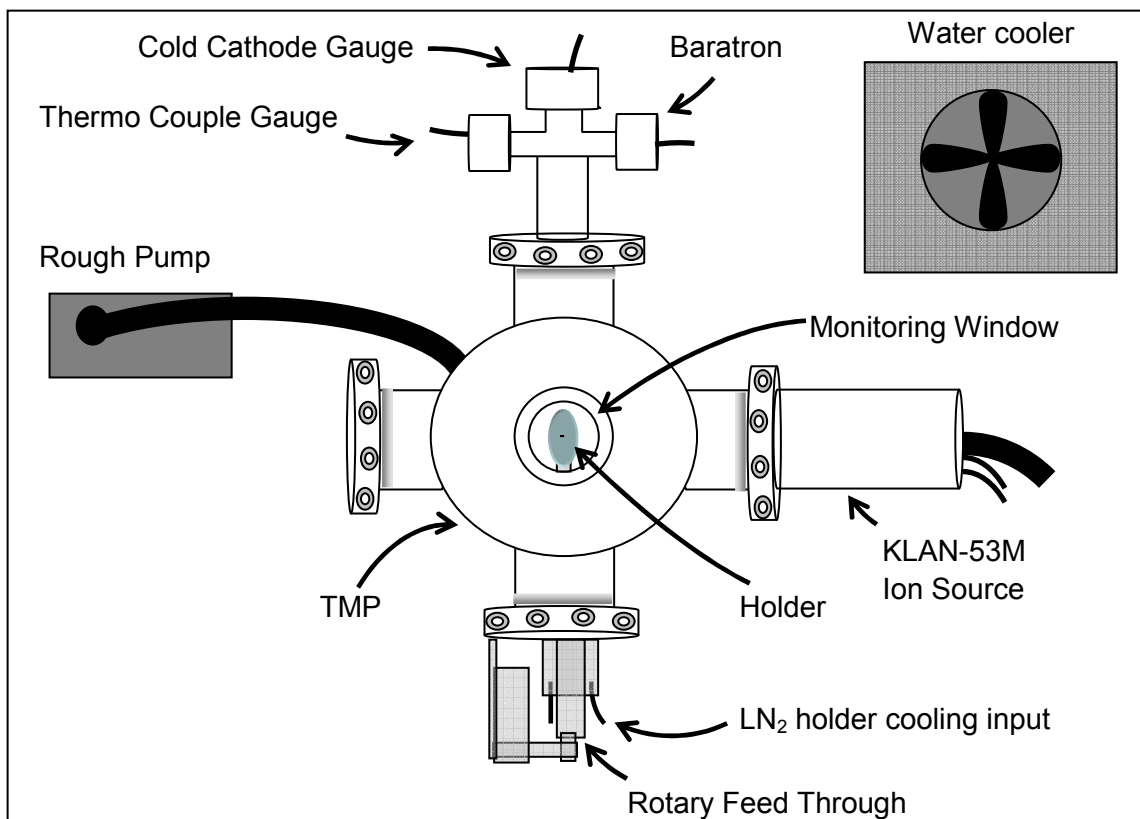
Figure 3.15. Top view schematic representation of our ion beam etching system

Table 3.2. Etching rates of old ion beam system

End Hall Type IBS	Au	Ta
Ar Plasma	10.0 nm/min	1.30 nm/min
N2 Plasma	2.77 nm/min	0.21 nm/min
	Ion Beam Etching (Ar)	Ion Beam Etching (N$_2$)
Base Pressure	<3 x10-6 Torr	<3 x10-6 Torr
Ion Beam Controller	700 V-50 mA-32 W	700 V-40 mA-27 W
TMP	0.73 A-53 W- 56 KRPM	0.67 A-49 W- 56 KRPM
Gas Flow	30 sccm (Ar)	40 sccm (N$_2$)
Working Pressure (Baratron)	2.66 mTorr	3.27 mTorr

Table 3.3. Etching rates of new ion beam system

Cold Cathode IBS(new)	Au	Ta	Photoresist(PR)
Ar Plasma	16 nm/min	0.75 nm/min	-------
N$_2$ Plasma	10 nm/min	0.45 nm/min	-------
Ar+O$_2$ Plasma	------	------	41 nm/min
	Parameters for Ar Etching	Parameters for N$_2$ Etching	Parameters for Ar+O$_2$ Etching
Discharge	50 V – 0.7 A	70 V – 0.5 A	60 V – 0.7 A
Cathode	320 V – 0.45 A	280 V – 0.35 A	380 V – 0.45 A
Acceleration	400 V – 1 mA	300 V – 1.5 mA	300 V – 1.5 mA
Ion Beam	300 V – 38 mA	400 V – 32 mA	500 V – 32 mA
Neutralizer	13 A – 38 mA	13 A – 32 mA	14.5 A – 32 mA
Gas Flow	2.7 sccm Ar	3 sccm N$_2$	2.7sccm Ar + 5sccm O$_2$
Cold Cathode Gauge	5 x10^{-4} Torr	3.8 x10^{-4} Torr	4x10^{-4} Torr

Diagram of ion source KLAN-53M together with power supply SEF-53M is shown in figure 3.16. The ion source consists of a cold hollow cathode (CHC), a discharge chamber, ion optics and a cathode neutralizer. The CHC contains a hollow frame with cooling jacket, a magnet system, igniting and output electrodes, and also gas

tube. The discharge chamber contains a frame, an anode and a magnet system. The ion optics includes screen and accelerator grids and also a ring grounded electrode. The neutralizer is an immersed filament. The power supply includes a discharge power unit (DhPU), a cathode power unit (ChPU), an ion beam power unit (BPU), an accelerator power unit (APU), a neutralizer heating power unit (NhPU) and a neutralizer coupling power unit (NcPU). Basic principle of operation of ion source is as follow:

At a gas and water feed to CHC, and also at a feed of voltage from ChPU between the igniting (output) electrodes and a cathode frame, an independent glow discharge with magnet field appears in the CHC. Primary electrons appear on the walls of the cathode due to a secondary ion-electron emission. Then they oscillate into the CHC and ionize atoms of operating gas. Ions appeared in the result of ionization fall down on cathode walls.

At a feed of voltage from DhPU between igniting (output) electrodes and the anode, electrons appeared in the result of ionization move through an orifice of the CHC in the discharge chamber being accelerated on a difference of potentials between cathode and chamber plasmas. A low pressure dependent discharge with magnet field appears in the discharge chamber. Electrons from the cathode and plasma electrons ionize atoms of operating gas that is introduced into the chamber through the cathode orifice. All electrons come to the anode finally. Ions from the discharge plasma fall down on walls of the discharge chamber and in holes of the screen grids of the ion optics.

At a feed of positive potential (from BPU) to the anode and at a feed of negative potential (from APU) to the accelerator grid, ions are being accelerated passing through holes in grids of the ion optics and are forming an ion beam.

At heating of the filament of the neutralizer (with help of NhPU) and at feed of a bias to the filament (with help of NcPU) appeared electrons move to an ion beam and provide a neutralization of a space charge of the ion beam.

DIAGRAM OF ION SOURCE KLAN-53M

AND POWER SUPPLY SEF-53M
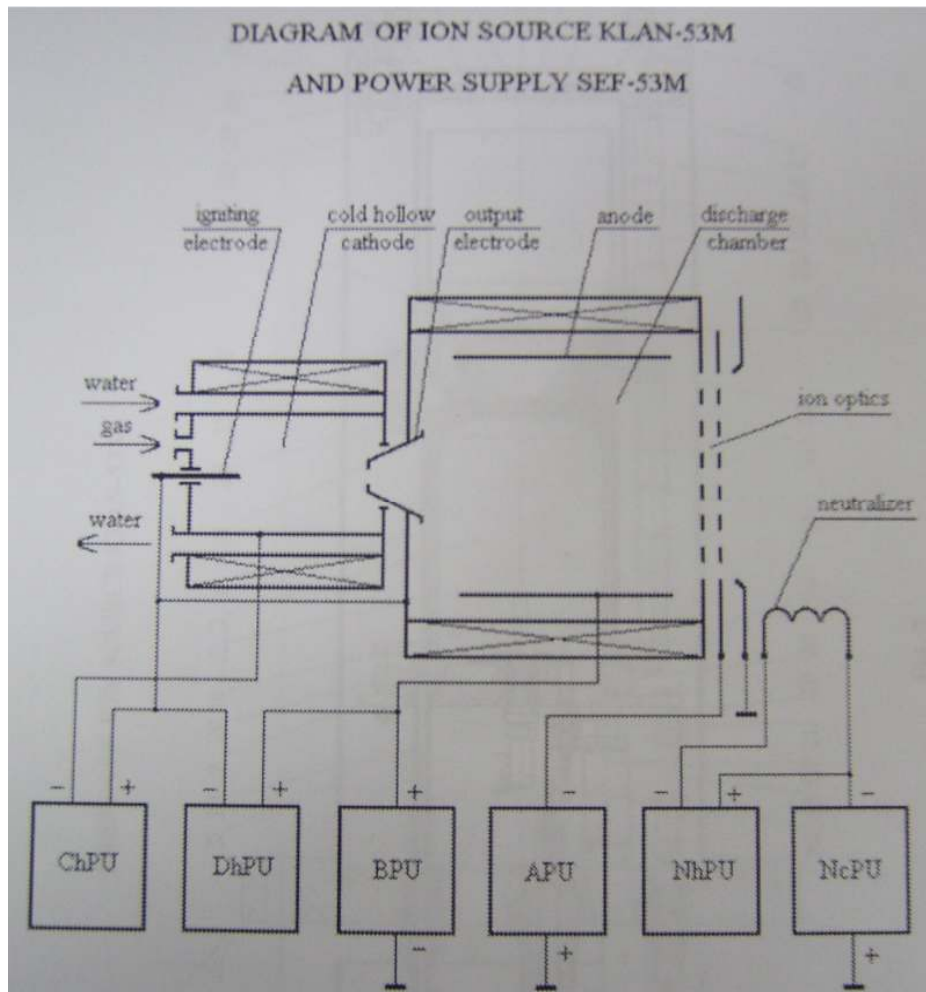
Figure 3.16. Schematics diagram of ion source KLAN-53M with power supply SEF-
53M

Since high vacuum is necessary to increase mean free path of ion beam, it
increases the possibility of etching on crystal without lost of their energies by colliding
with each other and other atoms in the chamber. Therefore turbo molecular pump with
back pump is used to reach the high vacuum that is 10^{-7} Torr for our system. The angle
between incident ion beam and sample surface was used 22.5^{o}, 45° and 67.5^{o}, and the
sample mounted to the sample holder to be the crystal whose long size of the PR pattern
along to the center of the sample holder. In fact, the samples position is not important,
because our sample holder is rotated with the rotary feed through. Since the heating
occurred on sample due to the long etching time may affect the superconducting
properties of Bi2212 single crystal, sample holder was cooled during the etching by
liquid N_2. We can approximately measure the temperature on the superconducting

crystal during the etching by using the thermocouple on the sample holder surface; it is almost -170°C.

3.4 Mesa Fabrication

In order to form mesa structure on the smooth surface of Ca-rich Bi2212 single crystals which contain natural intrinsic Josephson junction (IJJ) stacks along the c-axis, there are many experimental processes which are needed to be attentiveness. The mesa on superconducting Bi2212 single crystal with size of 40, 60, 80 and 100x300 μm^2 has been obtained using experimental techniques, which are described previous sections.

First of all, the single crystal from smooth a-b surface is glued onto a sapphire substrate by silver epoxy shown in figure 3.17a. Since direction of the normal vector of substrate is same with c-axis of Bi2212 crystal, the height of mesas fabricated on Bi2212 surface as a matchbox is lied along to c-axis of the crystal and its electrical measurements reveal c-axis behaviors of Bi2212 with IJJ. Here the reason of using the silver epoxy and sapphire substrate is their perfect thermal conductors because differences between crystal temperature and measured temperature on cold-head by sensor affect electrical results on mesa. Moreover since crystal needs to cool during the electrical measurement, it is much important that materials between crystal and cooling head are good thermal conductor to measure crystal temperature correctly and decrease local heating on crystal. In order to get a fresh and smooth surface on Bi2212, the crystal was mechanically cleaved with adhesive tape (Figure 3.17b). The adhesive tape is completely spread out on crystal then pulled out carefully until we get smooth fresh surface on Bi2212. After the cleaving process, gold layer with thickness of 50 to 100 nm is immediately deposited by a thermal evaporation technique on the fresh surface of the crystal in order not to lose clean fresh surface in the course of time (Figure 3.17c).
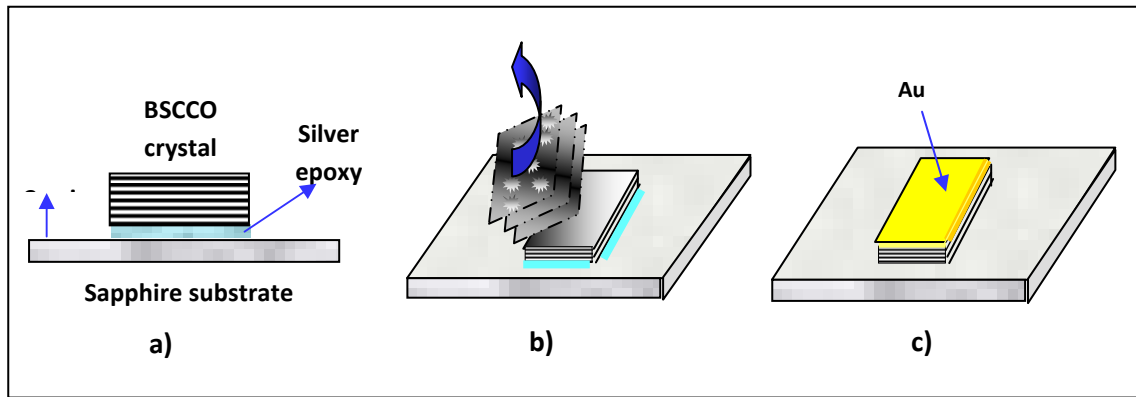
Figure 3.17. The steps in the beginning for the mesa fabrication a) Adhesion crystal on substrate b) Cleaving crystal c) After gold layer deposition on crystal

The gold material is not only good conductor but also protects the crystal surface from water and chemicals during the photolithography process. Moreover since it is non-reactive material, gold layer protect surface from oxidation.

In this thesis, to fabricate mesa I used three different masks that is single layer mask (PR) and two different multilayer masks, which are Ta/PR and PR′/Ta/PR. In the all three mask, all experimental steps are the same until the gold evaporation. After the gold evaporation, the experimental steps have different procedure.

After the gold evaporation, for the Ta/PR multilayer mask, Ta metal was deposited by DC magnetron sputtering as described in the experimental techniques, and for the PR′/Ta/PR multilayer mask, firstly photoresist was coated onto the gold layer as described in the first two steps of the photolithograph process in the experimental techniques but for this photoresist layer (PR′) the spinner was rotated at 6 V for 25 s giving a 750 nm layer of resist and then hard baked in the drying oven at the 200°C in the drying oven for 40 minutes to get strongest photoresist layer, secondly as the same with Ta/PR multilayer, Ta metal was deposited onto the PR′ layer. The aim of the using Ta/PR and PR′/Ta/PR multilayer masks is that it was used to form mesa with another material, apart from the photoresist (PR), which was used for the patterning the mesas. The thickness of photoresist is high and its edges are not smoothly perpendicular so during the etching, the edges of etched shape are like the curvature edges of mesa. Hence the smooth rectangular shape is not obtained. Furthermore, photoresist is etched with ions rapidly.

For the single layer mask after the gold evaporation, for the Ta/PR and PR′/Ta/PR multilayer masks after the Ta deposition, the next step in the mesa fabrication is optical photolithography which is used in micro fabrication to patterns photoresist (PR) layer on the gold layer and Ta layers of crystals. Thus selective areas without regions protected by PR layer are etched down by ion beam while PR patterns protect mesa areas from etching. Photolithography includes several steps in sequence as I stated before, summaries as in the figure 3.18.

After the preparation mesa shaped PR pattern, sample is mounted in to the ion beam etching system that produces ion beam accelerated through the surface of sample to etch down some area unprotected by PR layer on crystal. For the all three mask the etching procedure is different, but technique and the parameters are same.
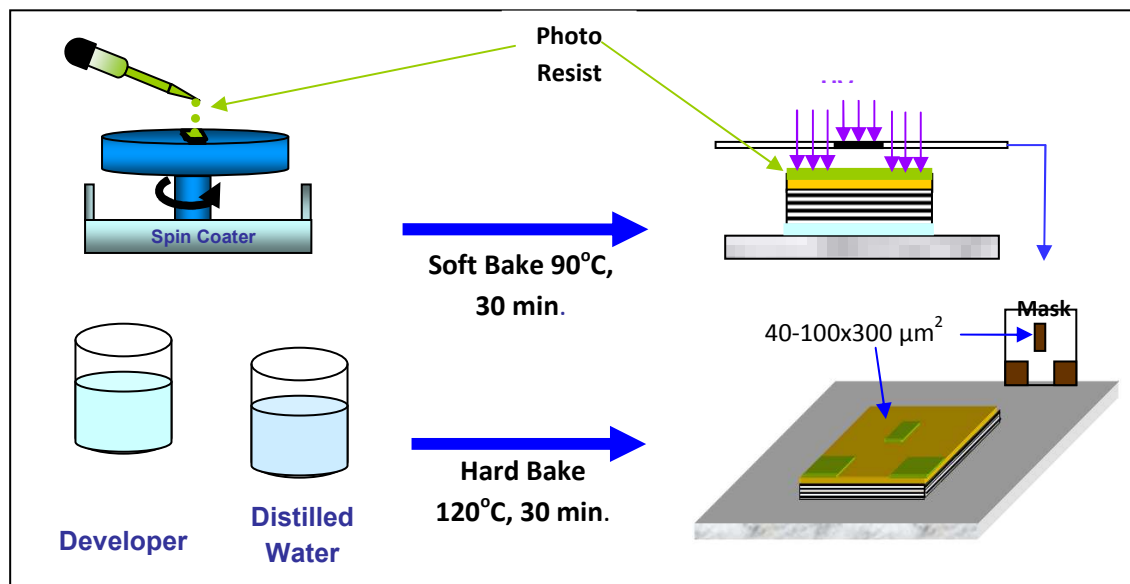
Figure 3.18. The schematic representation of photolithographic processes

For the **single layer mask (PR)**, reactive ion beam etching process was applied to the mounted sample (Bi2212/Au/PR) with Ar plasma until the PR layer onto the Au layer of mesa was removed. For the **Ta/PR multilayer mask**, reactive ion beam etching process was applied to the mounted sample (Bi2212/Au/Ta/PR) with Ar plasma until the Ta and Au layers out of the mesa was removed, then by using N_2 plasma, etching of Bi2212 was continue to get the Bi2212 mesa until the Ta layer onto the Au layer of mesa was removed. We used N_2 plasma for the etching of Bi2212, because the etching

rates of Ta is smaller than Bi2212. This provides us to fabricate taller (≈1μm) and high lateral angle mesas. For the **PR′/Ta/PR multilayer mask**, reactive ion beam etching process was applied to the mounted sample (Bi2212/Au/PR′/Ta/PR) with Ar plasma until the Ta and Au layers out of the mesa was removed then with Ar+O2 plasma the PR′ layer onto the out of mesa was removed and then etching of Bi2212 with N_2 plasma was continue to get the Bi2212 mesa until the Ta layer onto the PR′ layer of mesa was removed. After the Ta layer was etched, the sample has taller mesa with high lateral angle and at the top of the mesa, there are PR′ layer. To etch the PR′ layer, etching was ended with Ar+O2 plasma until the PR′ layer onto the Au layer of mesa was etched. Before and after the etching process, schematic views of the samples are shown in the figure 3.19.
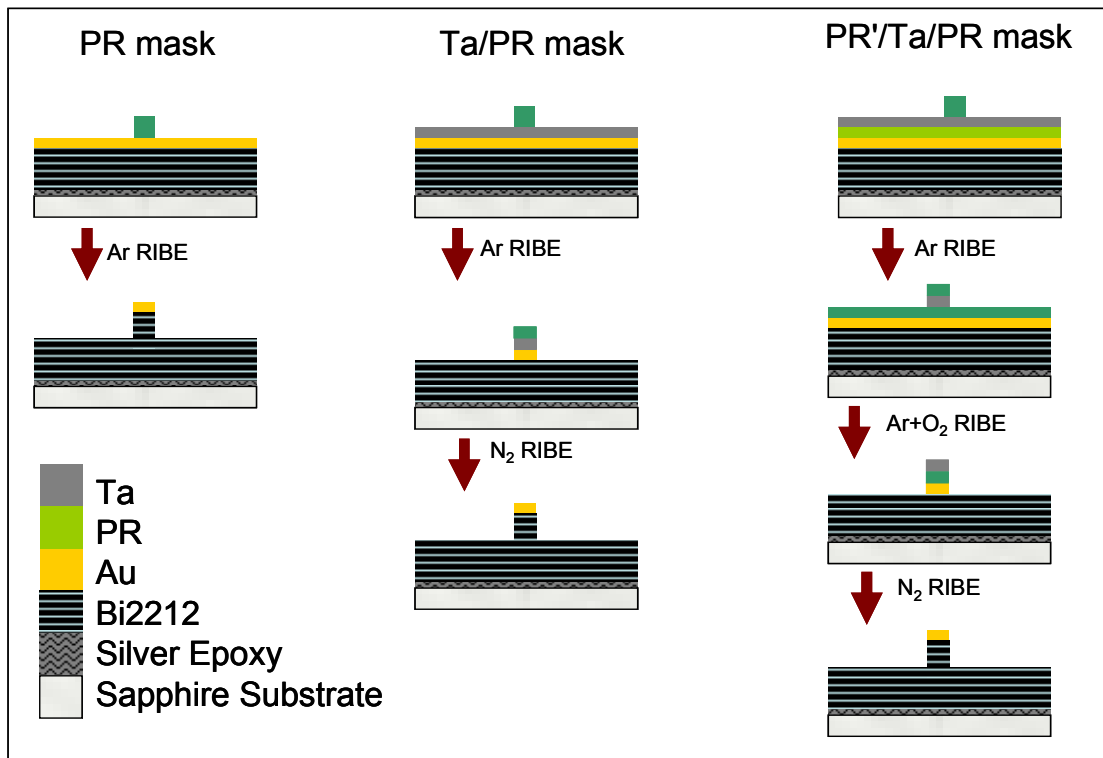
Figure 3.19. Schematic views of the samples before and after the etching process

Because of the difficulties in making a contact on small area of the mesa, we use a different contact technique including several processes. Firstly CaF_2 insulating layer is deposited by evaporation onto crystal and small area of the mesa in which are not covered by a mask (Figure 3.20a). Then a shadow mask whose split lying along the

mesa and insulating layer is placed on substrate and a gold stripe with width of 50 μm is deposited by evaporation on insulating layer and mesa (Figure 3.20b). Finally three gold probe wires belong to I-V are connected by silver epoxy on two patterns and mesa. The final seen of the mesa and contact on mesa is common probe for measurements of current and voltage can be seen in the figure 3.20c and d.
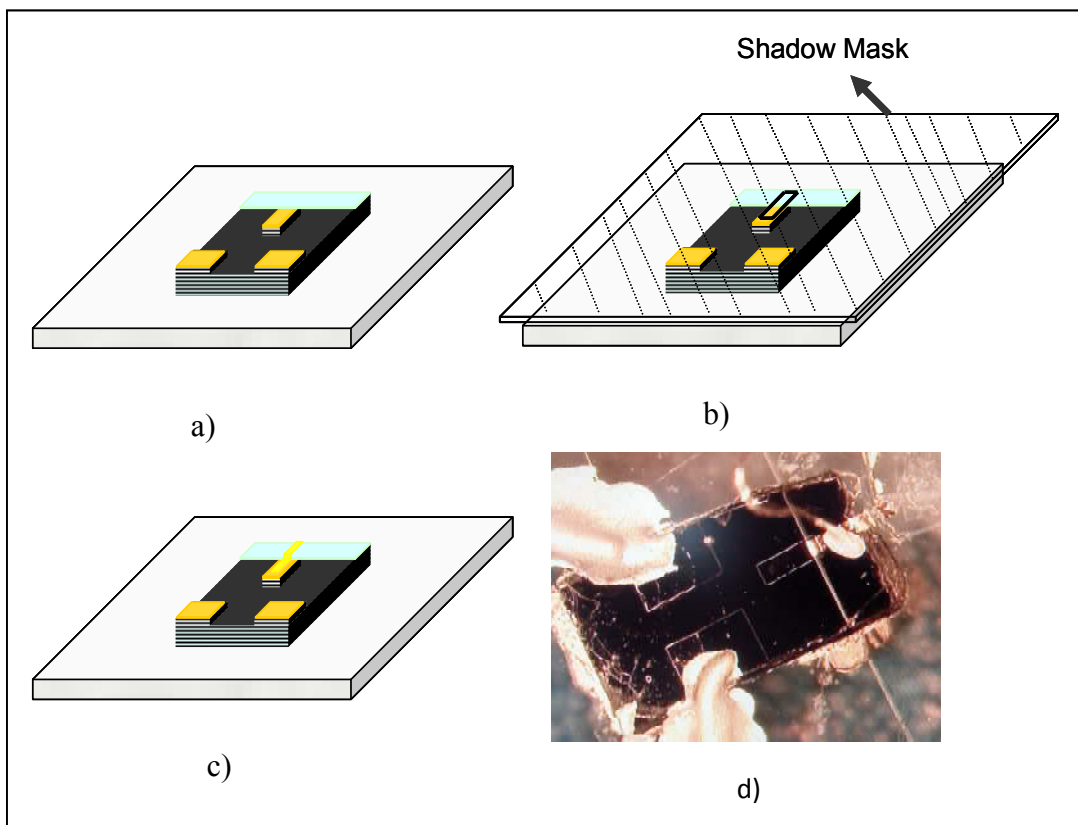
Figure 3.20. The three point contact technique on small area of the mesa a) CaF_2 deposition onto crystal and small part of mesa b) Gold stripe deposition on mesa and CaF_2 layer c) Final Seen d)The three probe contact.

3.5 Characterization Methods

3.5.1 Height Measurements by AFM, Profilometer and SEM

To measure the deposited thin films thicknesses onto the Bi2212 single crystal surface and the mesa height after the fabrication of mesa, we used AFM, Profilometer and SEM. We can measure the thicknesses of thin films and mesa height and lateral angle by using AFM. However, we must also use SEM to measure the a-axis of the mesa, as we measure the height of the mesa (c-axis) by using profilometer, because the measurements by profilometer is accuracy just for height (c-axis) measurements.

Tapping mode was used at AFM measurements that were done in center for materials research of Izmir Institute of Technology (IZTECH) and Application nanotechnology laboratory of IZTECH Physics Department. Some advantages of the tapping mode are that lateral resolution of this mode on sample with soft surface is the most improved in other modes of AFM and it also minimizes surface distortion (Martin, et al. 1987). At surface topographic images of AFM, color contrast such as variation from brightness to darkness is used to determine rough structure on surface. Beside 2-D surface topographic analyses of mesa, 3-D image, step height and lateral angle of fabricated mesa have been analyzed by using raw AFM data.

In the profilometer and SEM measurements, profilometer measurements were done in the IZTECH physics department, but SEM measurements were done in the Physical Institute III at Erlangen University. From the profilometer measurements, we can determine the height of mesa and deposited thin films. From the SEM measurements we can determine the a-axis distance of the mesa to calculate the lateral angle of the mesa by equation 3.1.

$$\theta(lateral \quad angle \quad of \quad mesa) = \tan^{-1}\left(\frac{profilometer \quad data \quad (c-axis)}{SEM \quad data \quad (a-axis)}\right) \qquad (3.1)$$

Heights of the fabricated mesas have been measured by AFM but this height includes also gold layer thickness. In order to learn only mesa height we need to subtract it from measured thickness of mesa with gold layer, so it is necessary to measure gold layer thickness on mesa. On the other hand, it is not possible to measure gold layer thickness on mesa, so before the starting evaporation we mount clean glass near the sample in evaporator. Although we know the thickness of the evaporated gold layer by thickness monitor, we measure it. Since same gold layer thickness onto both crystal and glass are deposited at end of the evaporation, we measure gold layer thickness on ditch in which lightly scratching only gold layer by needle in the profilometer or AFM measurements.

For the PR and the Ta layers thickness, at the beginning of my thesis I calibrated them. I can do the same deposition or coating, whenever I did deposition of Ta or coating PR by using the calibration parameters.

3.5.2 R-T, I-V and Bolometer Measurements by THz Cryostat System

THz cryostat system (or continuous flow cryostat system) seen in figure 3.21 is used in order to decrease temperature of the crystal below T_c and measure the superconducting behaviors and the bolometric measurements of the Bi2212 crystal. The system includes a vacuum loading cryostat, a Si bolometer, chopper, instruments and computer. For cooling the crystal, liquid He transfers from external reservoir to copper cold finger inside cryostat. The sample temperature on cold finger is controlled by heater and temperature sensor that are interfaced by a temperature controller. It is very important to not only investigate temperature dependence of I-V characteristic of IJJs but also emission detection from the mesa at different temperatures. The system also has optical cryostat to detect the radiation emitted from samples. It has turbo molecular pumping system that pumps between cold finger and shield of the cryostat until ultra high vacuum. Due to the good thermal isolation, temperature of sample can be decreased to 4.2 K.
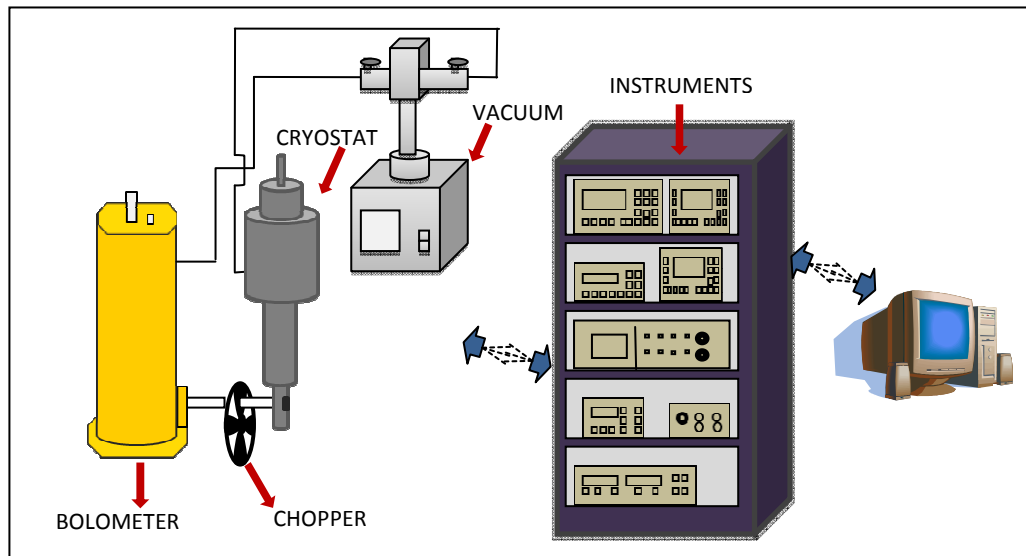
Figure 3.21. The schematic of our THz cryostat system

We have done resistance versus temperature (R-T) and current versus voltage (I-V) measurements on mesa and the schematic representation of our experimental setups for the measurements is shown in figure 3.22. The setups are interfaced with a computer and controlled by Lab-view program that contains serial instrument control, data analysis and data storage. In addition its graphical programming tool provides to see drift of the experimental result during the measurement and it has a block diagram form that allows creating program for the measurements.

During the variations of temperature between room temperature and 4.2 K, simultaneously changing mesa resistance values with temperature are measured using the experimental setup seen in the figure 3.22.a and it includes current source, voltmeter and temperature controller which are interfaced with a computer. The variations at voltage and temperature are measured by voltmeter and temperature controller respectively. Since applied current along to mesa height is constant during the measurement, experimental data is analyzed and stored such as R-T by Lab-view program. In order to acquire accurate data, current with both positive and negative direction are rapidly applied by current source and at same temperature resistance is measured twice. Thus average resistance versus temperature is used. Since a good thermal isolation with vacuum between cold head and shield at cryostat can not be well

created, there is a problem in thermal equilibrium between crystal and cooling head. Therefore for the accurate data, measurement during the increasing temperature is considered for R-T.
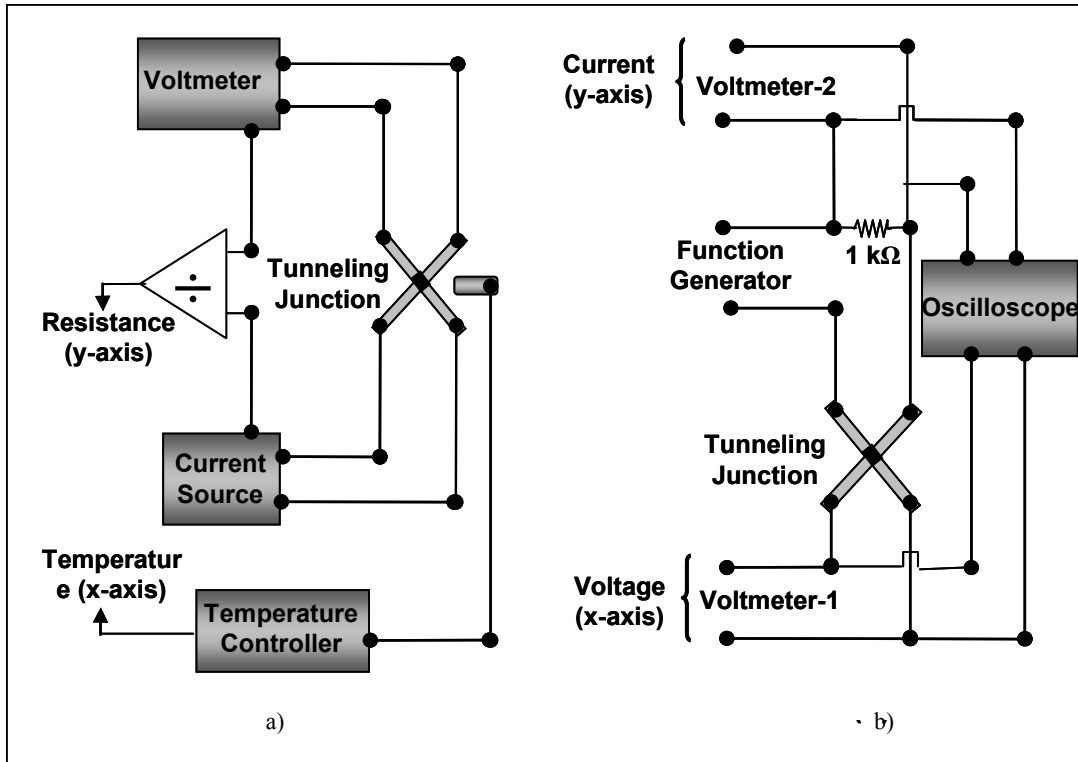
Figure 3.22. Schematic representations of our experimental setups a) R-T b) I-V measurements (Source: Simsek, 2008)

Figure 3.22.b shows I-V experimental setup interfaced with a computer. This setup includes two voltmeters to measure voltage of mesa including all junctions and applied current on resistance serially connected to circuit between function generator and mesa. Function generator is used to apply current with required frequencies and amplitudes. Sample temperature is kept constant by heater in cryostat and the amount of Helium gas flow which are controlled by temperature controller during the I-V measurement. In order to take a good I-V measurement with hysterical behavior and much quasi-particle branches, current with low frequency (5 mHz) is applied while its amplitude is gradually increasing until obtaining whole hysterical curve including normal state. Oscillator provides to see the voltage jump value and I-V drift before starting to measurement. Thus data including current versus voltage and constant

temperature is obtained by Lab-view program. I-V measurements have been done at various temperatures.

The bolometric measurements were obtained while I-V measurements through c-axis of Bi2212 are simultaneously recording. When bias voltage decrease, the experiments of detection of emission from long side of mesa on Bi2212 by bolometer have been considered. A continuous flow cryostat system was used to perform the bolometric experiments in wide temperature range. The sapphire substrates were mounted on cold finger in cryostat as its long side of mesas was opposite the window of optical cryostat. Because our Si bolometer is able to detect the discontinuous radiation, chopper between cryostat window and bolometer was mounted to modulate emission of radiation to pulse. The chopping frequency for our measurements is 140 Hz. The Si Bolometer is cooled by liquid He for its operation temperature. Output signal from bolometer is amplified by lock-in amplifier and it refers to emission power of radiation emitted from mesa. Our first purpose is to observe emission peak from sample during I-V measurement, so the system is as enough as to give information us about whether crystal structure, tunneling characteristic of whole IJJs and mesa lateral dimensions are available for THz emission. Since our proposed method on synchronization of IJJs in mesa for obtaining THz emission needs DC voltage applied through the tall mesa (Ozyuzer, et al. 2007). This DC voltage values corresponding with emission peak of all IJJs were scanned by bolometric measurement during I-V measurements through the tall mesa. Therefore two measurements were simultaneously recorded. At the measurements, used devices which are function generator, voltmeter, temperature controller and lock-in amplifier are interfaced by a computer and controller by Lab-view program.

CHAPTER 4

RESULTS AND DISCUSSION

Generation of powerful THz radiation requires mesas with large lateral dimension but there are difficulties in fabrication of perfect rectangular mesa. It should be close to 90 degrees to obtain IJJs with same planar dimensions for synchronization of IJJs (Koshelev, 2008). The previous study lateral angles of fabricated mesas are very low by using single layer (PR) mask. It seems such a main problem in generation of THz emission because low lateral angles means that mesas are trapezoid geometric shape. The main purpose of our work is fabrication of mesas by using single layer mask (PR) and two different multilayer masks, which are Ta/PR and PR′/Ta/PR for the generation of THz radiation. Thick photoresist layer (single layer mask) shades the lateral dimension of mesa during ion beam etching. Therefore, we patterned multilayer mask on Bi2212 and used selective ion etching as in Nagai et al. 1991 overcome this problem. In this purpose, large and tall mesas on Ca rich Bi2212 mesas fabricated by using vacuum thermal deposition, optical photolithography and reactive ion beam etching technique, which are anticipated to have smooth rectangular prism shape with large area, high thickness and lateral angle which are related to capability of emitting THz rays.

In the Electrical characterizations of mesas, R-T and I-V measurements were done to get information about superconducting and temperature dependence of tunneling behaviors in IJJs. Moreover their temperature dependences are analyzed in these electrical characterizations. In a study by Kadowaki, et al. (2006) published that THz radiation power was investigated at various temperatures and it was found that emission power from IJJs in Bi2212 changes with temperature. It was also claimed in another study done by (Ozyuzer, et al. 2007). They have obtained that coherent THz emissions with some powers exists at different temperatures in superconducting state.

Therefore I-V measurements of fabricated mesas at various temperatures were analyzed before bolometric detection of emission.

One of the parameters in detection of THz radiation emitted from IJJs stacks is temperature, so bolometric measurements were repeated at different temperature in the same mesa. These measurements on emission peak detection from long side of mesas were simultaneously recorded with I-V measurements. These measurements were allowed to be repeated severally at constant temperatures because bolometric output peaks should be reproducible for each scanning of bias voltage decreasing toward to zero. Thus it is clearly said that they are emissions from Bi2212 single crystals.

4.1. Results of Thickness Measurements on Mesas

Heights of the fabricated mesas have been measured by AFM but this height includes also gold layer thickness. In order to learn only mesa height we need to subtract the gold layer on the Bi2212 mesa from measured thickness of mesa with gold layer. Therefore the gold layer was deposited approximately 50-100 nm, which is known from the thickness monitor value and profile measurements.

The c-axis of Bi2212 single crystal is laid along the mesa height, so number of IJJs along the mesa height is obtained after fabrication processes. Since it is known that thickness of an IJJ is 1.5 nm, the number of IJJs in mesa is calculated from mesa height. For example, mesa with height of 1μm contains approximately 670 IJJs. Therefore thicknesses of the fabricated mesas were analyzed by atomic force microscope (AFM).

The figures below give an idea about the structure of both the edges directly see the ion beam and place under the shadow of the ion beam. As the edges directly see the ion beam have smooth surface, other edges show rough structure. Moreover, for the HC06, the angle between the edges and the surface is about 35° (for the left (3, labeled in the figure 4.1) and 75° (for the right (1, labeled in the figure 4.1) and it shows that the cross section of the mesa is not etched as a rectangular shape, it has a irregular shape and using multilayer instead of a single layer provides higher lateral angle of the mesa. This etching can occur from the use of our parameters of our ion beam and also under

the effects of layer structure of the Bi2212. AFM views of the other samples are shown below and AFM analysis results are given in the table 4.1.
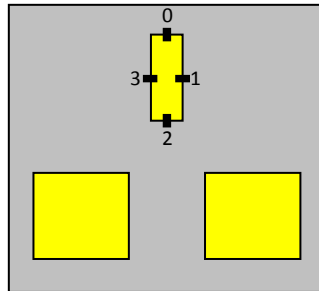
Figure 4.1. Labeled codes of mesa edges

If we compare the figure 4.2 and 4.3, it is seen that the lateral angles of AFM results and the SEM results are same. The AFM height measurements are used because we cannot measure height from the SEM images. So only the AFM measurements are given then. The figure 4.4 - 4.7 is the AFM measurements of the Bi2212/Au/PR/Ta multilayer mesas as we found the lateral angles. Figure 4.8 is the AFM study of Bi2212/Au/Ta structural multilayer. As it is seen from the table 4.1, using multilayer instead of single layer indicates a distinctive increase of the lateral angle, and this is the proof of the approaching nearly rectangular mesa.
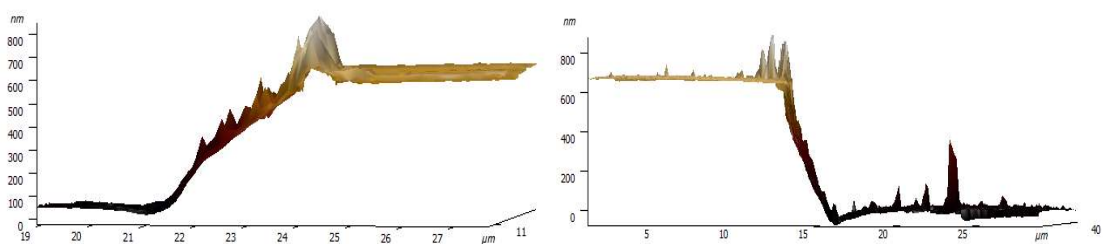
Figure 4.2. AFM measurement of HC09 (Bi2212/Au)
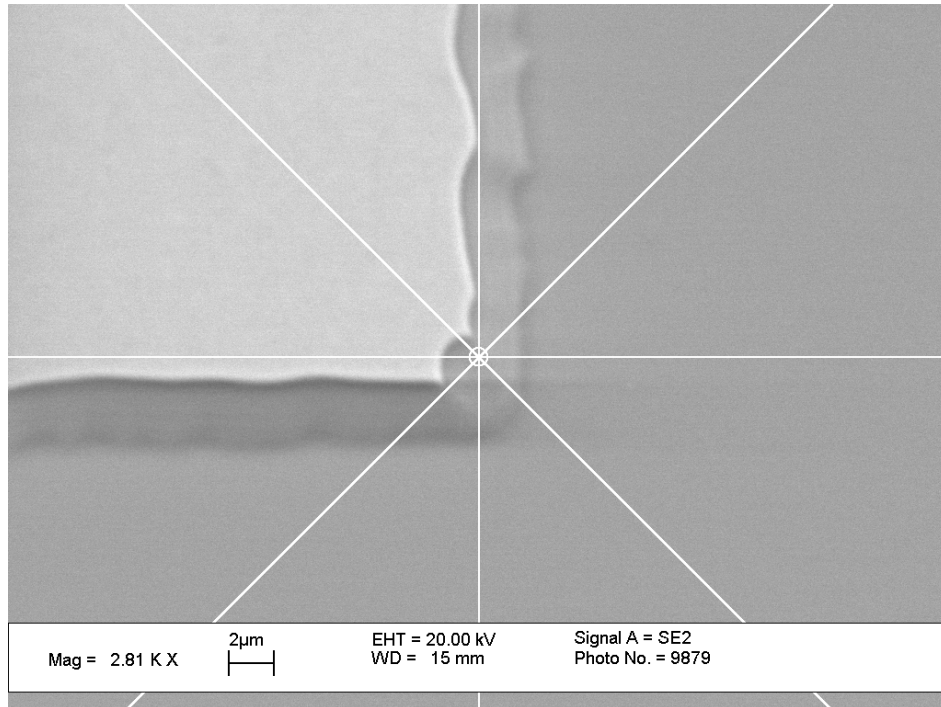
Figure 4.3. Top view SEM image of HC09. Pyramid structure at the edges can be clearly seen
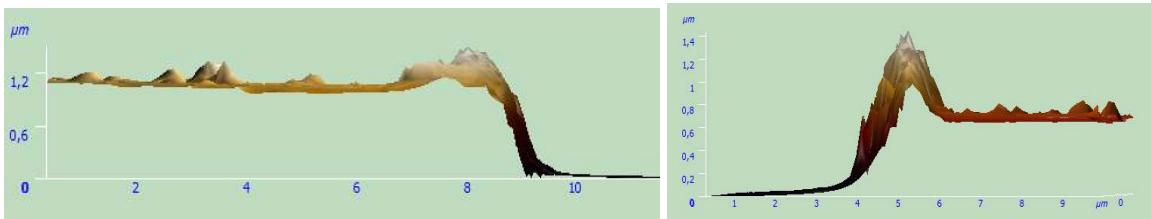
Figure 4.4. AFM measurement of HC06 (Bi2212/Au/PR/Ta)
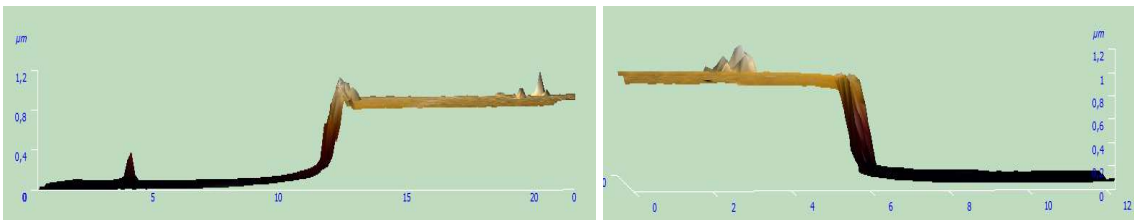
Figure 4.5. AFM measurement of HK6 (Bi2212/Au/PR/Ta)
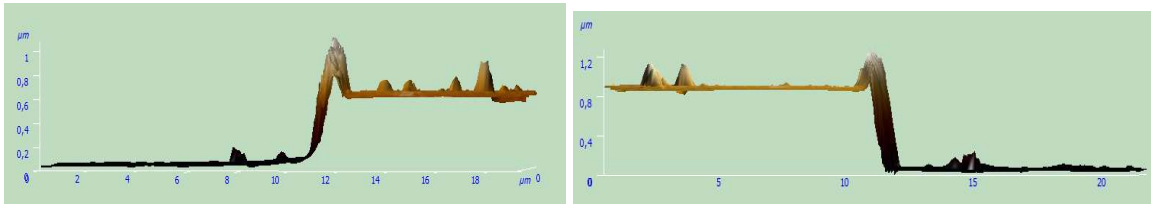
Figure 4.6. AFM measurement of HK7 (Bi2212/Au/PR/Ta)
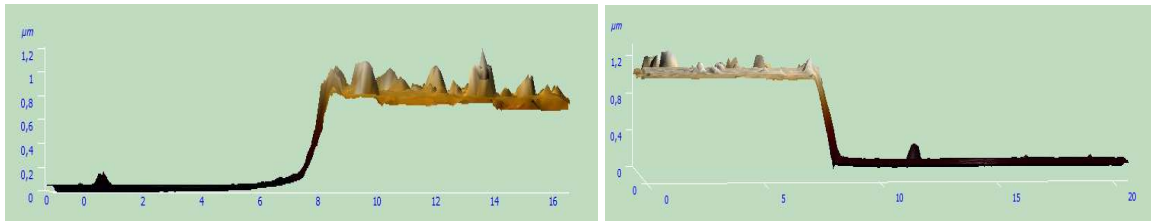
Figure 4.7. AFM measurement of HC07 (Bi2212/Au/PR/Ta)
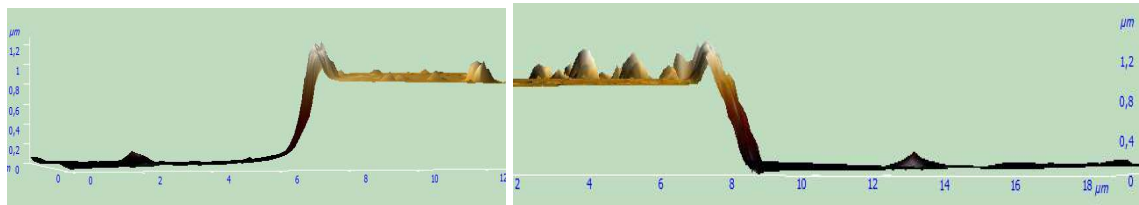
Figure 4.8. AFM measurement of SG12–1 (Bi2212/Au/Ta)

Table 4.1. Results of AFM analysis

Mesa height and lateral angle	Edge 1	Edge 3
HC09 (Bi2212/Au)	570 nm - 12°	650 nm - 13°
HC06 (Bi2212/Au/PR/Ta)	860 nm - 75°	770 nm - 35°
HK6 (Bi2212/Au/PR/Ta)	850 nm - 65°	810 nm - 45°
HK7 (Bi2212/Au/PR/Ta)	830 nm - 58°	580 nm - 45°
HC07 (Bi2212/Au/PR/Ta)	930 nm – 50°	820 nm - 42°
SG12–1 (Bi2212/Au/Ta)	860 nm - 51°	870nm - 52°

4.2. Electrical Results

4.2.1. Temperature Dependence of c-axis Resistance in Bi2212

We have measured resistance versus temperature through the height of the mesas by using THz Cryostat systems (continuous flow He cryostat systems). The temperature dependence of c-axis resistances of Bi2212 and phase transition from the normal conductor to superconductor are seen in Figure 4.9, Figure 4.10, Figure 4.11 and Figure 4.12 for the sample of the HC09, HC12, SG10-8 and SG12-3 respectively.

Firstly the sharp phase transitions to superconducting state are seen in R-T figures. Transition temperatures and their transition width values (ΔT) are shown in Table 4.2. Although all of Bi2212 superconducting single crystals used for mesa fabrication are in underdoped region, there are differences in their transition temperatures. Moreover, Annealed grown crystal by self flux method at 450°C for 10 hours is optimally doped region.

The oxygen doping rate in Bi2212 crystal changes its transition temperature. Oxygen doping rate can be different inside each of the crystal or changed by some heating processes at mesa fabrication. In a previous study done on same crystal, the critical temperatures (T_c) of as grown crystals have been published to be about 72-74 K. In underdoped region, T_c of Ca rich Bi2212 single crystal (as grown crystal) was demonstrated to be about 62 K. If we examine our T_c values, the transition temperatures are for the as grown crystals 44 K and 54 K, for grown crystals by self flux method 70 K and 76 K (Table 4.2). It is seen from phase diagram of Bi2212 that they are in underdoped region instead of optimally doped SG12-3.

From the 300 K to T_c, characteristic behaviors of temperature dependent resistance of as grown Bi2212 single crystal along the c-axis are seen in these figures. That is, the exponential increasing resistance from room temperature to T_c was well observed and the variations at mesa resistances are shown in (Table 4.2). For all fabricated mesas, the ratios of R_{Tc}/R_{300K} are between 3.5 and 5, but only the ratios of R_{Tc}/R_{300K} in the SG12-3 it is 0.94, which is optimally doped region.

Table 4.2. Variation of resistance of mesa on Bi2212 single crystal and their transition temperature

	R_{300K} (Ω)	$R_{Tc(in)}$ (Ω)	$R_{Tc(zero)}$ (Ω)	$T_{c(in)}$ (K)	$T_{c(zero)}$ (K)	R_{Tc}/R_{300K}	ΔT (K)
HC09(PR) (60x100 μm^2)	17.1	67.7	3.31	59.2	44	3.9	15.2
HC12(PR) (60x100 μm^2)	84.5	446.7	231.09	72.8	53.6	5.2	19.2
SG12-3(Ta/PR) (80x100 μm^2)	6.16	5.8	2.47	81.6	76	0.94	5.6
SG10-8(PR′/Ta/PR) (60x100 μm^2)	19.2	84.5	22.6	77.7	69.8	4.4	7.9

From the critical temperatures to low temperatures, increasing in resistance is unusually seen on all R-T graphs. This case is not a temperature dependent electrical behavior proper to superconducting crystal. It result from three probe contact method that is not generally preferred to four point contact method for accurate measurement because there is one contact probe on mesa which is used for both applying current and measuring voltage and it causes the resistance at superconducting state. However four point contact is very difficult to fabricate on mesa and it is required some experimental processes with technical equipments. It is also found in a paper published by (Yurgens, et al. in 1997).

In R-T graph of HC12, contact resistance is clearly seen below T_c as we compare the other R-T graph. In order to minimize contact resistance, samples can be annealed at 350°C, but it was not generally preferred since oxygen doping level in Bi2212 does not change. There are several reasons of contact resistance. Firstly it may be caused by resistance of silver epoxy connected gold wire to patterns on Bi2212, because this conducting adhesion is obtained by mixing two equal composites. If they are not mixed well, its conductance will be low. The other reason is the interface between gold layer and surface of Bi2212. This kind of contact resistance increase at low temperature, because the interface behaves tunneling barriers and temperature dependence of barrier height is dominant in contact resistance. Therefore in R-T graphs, we see increasing in resistance from T_c to low temperatures.
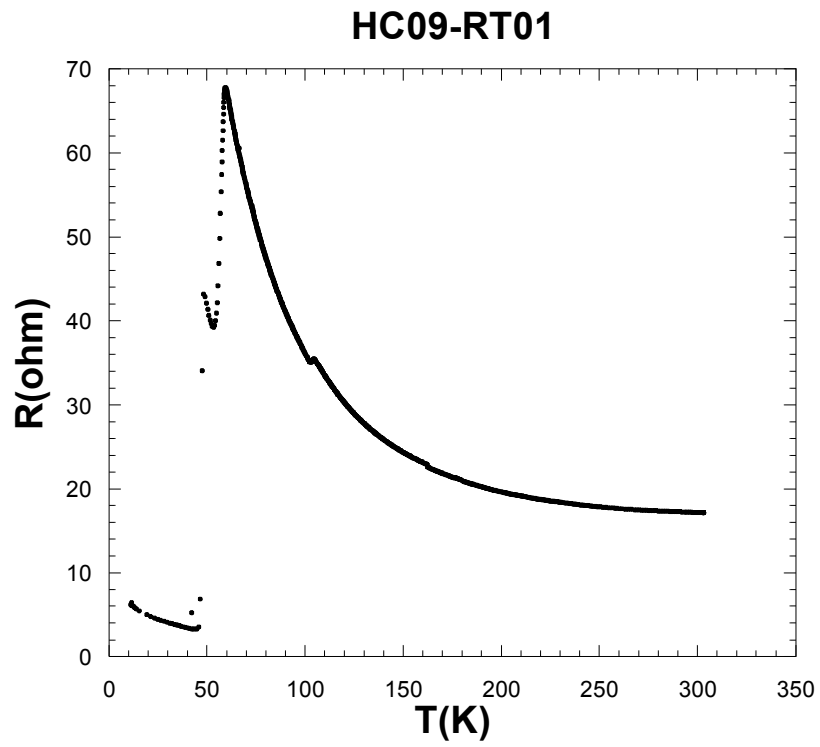
HC09-RT01

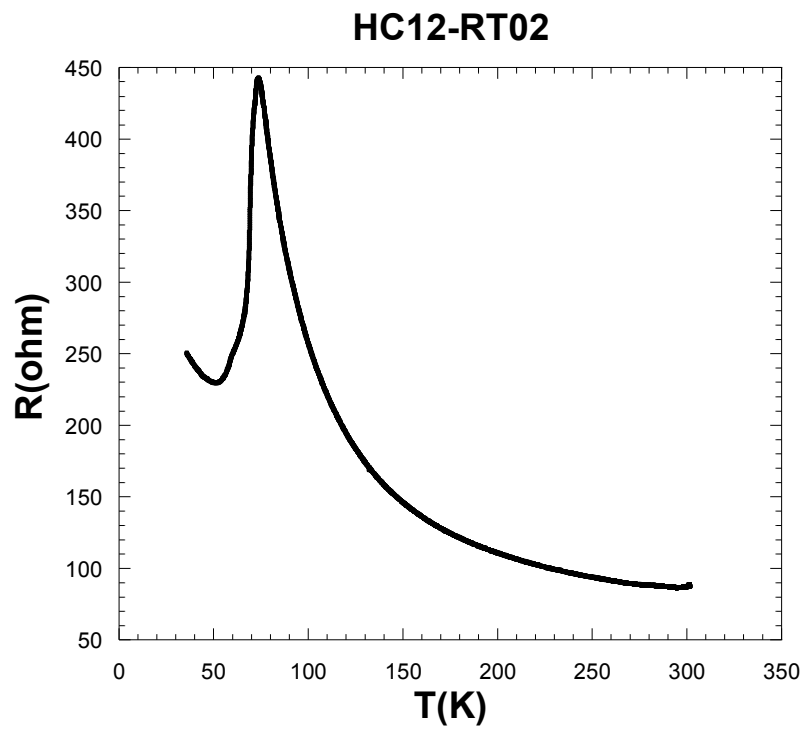Figure 4.9. Variation of resistance versus temperature of HC09

HC12-RT02

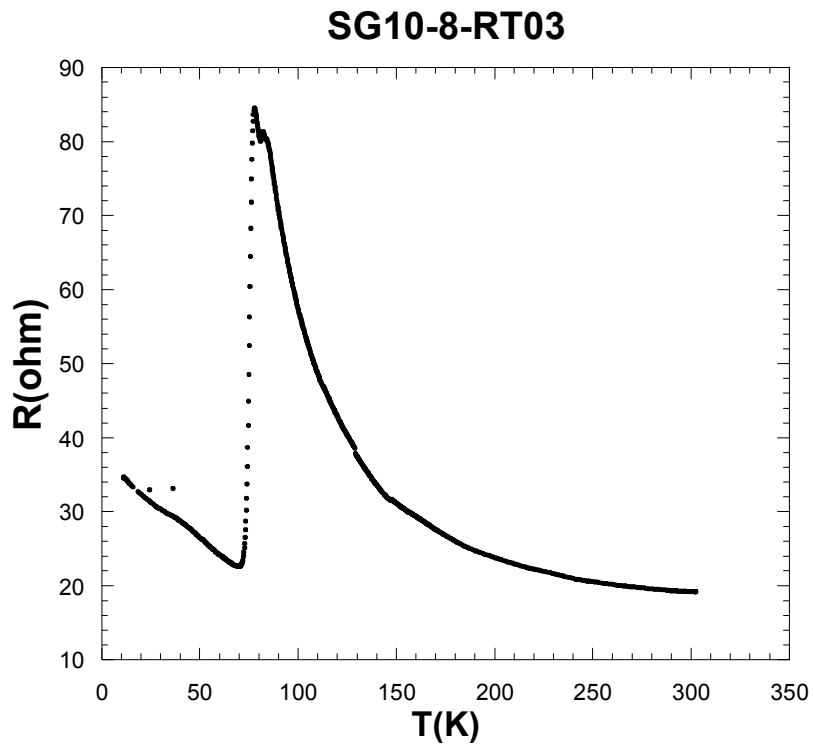Figure 4.10. Variation of resistance versus temperature of HC12

SG10-8-RT03

Figure 4.11. Variation of resistance versus temperature of SG10-8
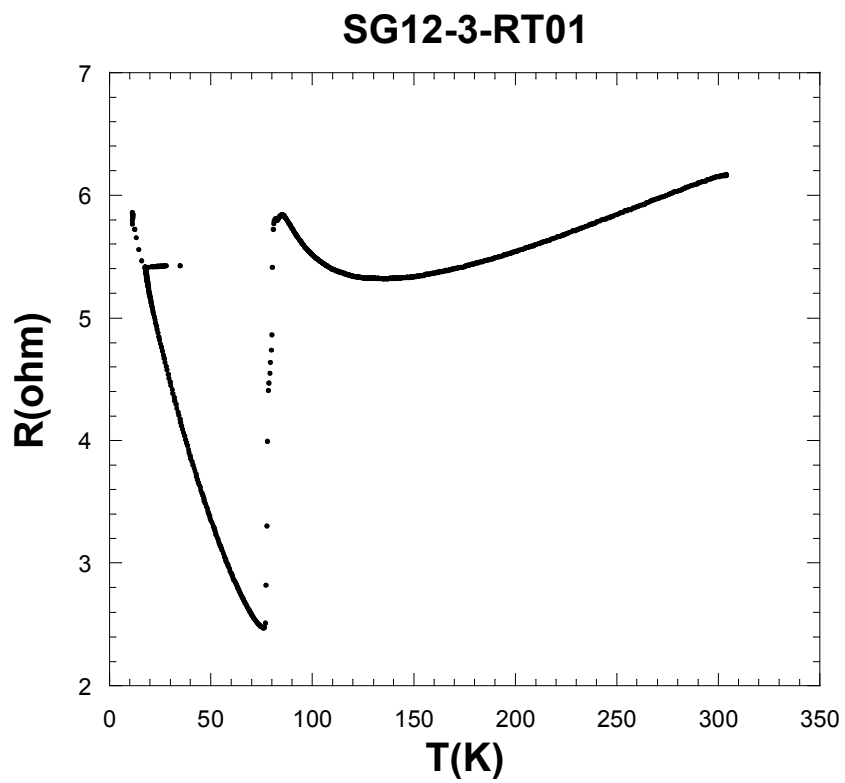
SG12-3-RT01

Figure 4.12. Variation of resistance versus temperature of SG12-3

4.2.2. Tunneling Characteristic of Bi2212 Single Crystal

In our I-V measurements of c-axis of Bi2212, the quasiparticle branches and large hysteretic behavior can be seen when temperature is below its T_c. They are characteristic of c-axis tunneling behaviors of anisotropic superconducting material of Bi2212. The fabricated mesas include number of IJJs, so I-V measurements exhibit tunneling behaviors including the contributions of whole stacks of IJJs. The voltage jumps corresponding to quasiparticle branches are seen in these I-V graphs. While bias voltage increases these branches appear such a voltage jumps until all IJJs are completely in normal state. During the sweeping of bias voltage negatively and positively from zero voltage, each branch occurs when individual IJJ is switched from Josephson state to quasiparticle state by bias current exceeding its I_c. Therefore it is strongly expected that branches are observed as many as the number of IJJs (Yurgens 2000).

Josephson current with hysteresis behavior is seen at zero bias and it only occurs from cooper pair tunneling while all IJJs are in superconducting state. The hysteretic behavior of Josephson current results from switching the current from cooper pair tunneling to quasiparticle tunneling (Ozyuzer, et al. 2000). After exceeding of Josephson current, I-V data traces on quasiparticle branches that are one by one corresponding IJJs. The voltage value on which all of IJJs start to pass into normal state is called as total conductance peak of IJJs. For example, if we want to find superconducting energy gap corresponding to an individual SIS Josephson junction, the voltage values in I-V data should be divided by the number of IJJs (Yurgens 2000). While decreasing bias voltage, I-V data does not trace these branches because there is a transition from normal state to superconducting state. Therefore large hysteric I-V curve with many branches are obtained.

In order to obtain as much as more quasiparticle branches in I-V, the swept frequency should be low while ac bias current on mesa is swept negatively and positively by function generator. In our measurement, it was between 0.1 and 5 mHz to catch more branches and has triangle wave form. Especially, increasing bias voltage, ac current with low swept frequency were used because branches can be appears during

increasing bias voltage negatively and positively. Also the output amplitude of function generator was gradually increased in order not to allow the heating in mesa due to high bias current. Thus without encountering influence of joule heating, branches were obtained step by step increasing output amplitude of function generator. In order to learn maximum output amplitude for mesa before starting the experiment, oscilloscope was used.

Less quasiparticle branches are seen in our measurements. Sometimes it may be due to measurement problem such high swept frequency and quick increasing in amplitude of function generator output but general aspect of our I-V measurement reveals heating effect. In figure 4.13, disorder and branching of total conductance peak in the nearby 750 mV is an evidence of heating in mesa. Since our superconducting crystal has poor thermal conductivity, there are problem in distribution of heating during the applied bias current. Thus local heating occurs on crystal and if its temperature rises above critical temperature, superconducting state is destroyed at some regions.

I-V measurements of HB09 (figure 4.13) and HC12 (figure 4.14) have been done at same temperature and their mesa sizes same (800 nm). However, if we compare two I-V graphs, it is seen that the quasiparticle branches of HC09 is more than HC12. Their critical Josephson current values are between 7-9 mA.
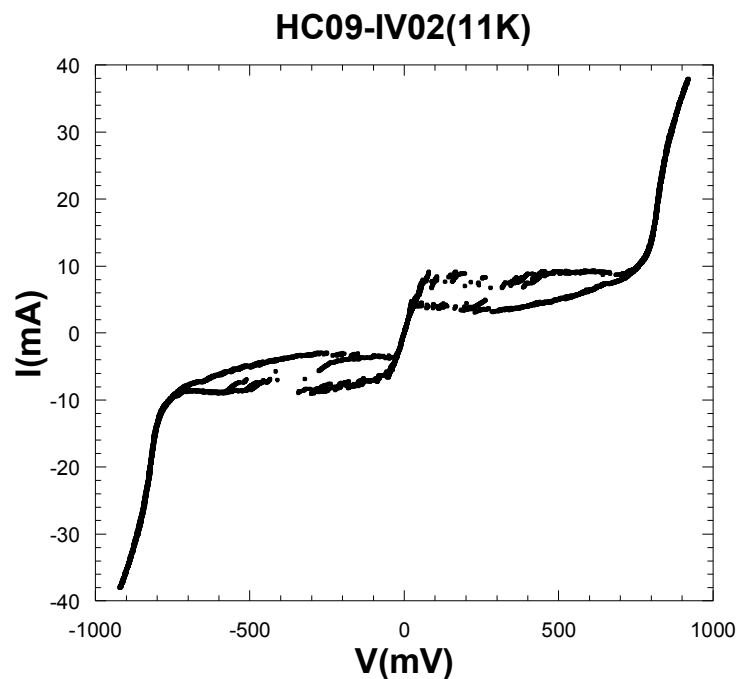
HC09-IV02(11K)

Figure 4.13. I-V measurement of HC09

HC12 IV01(11K)
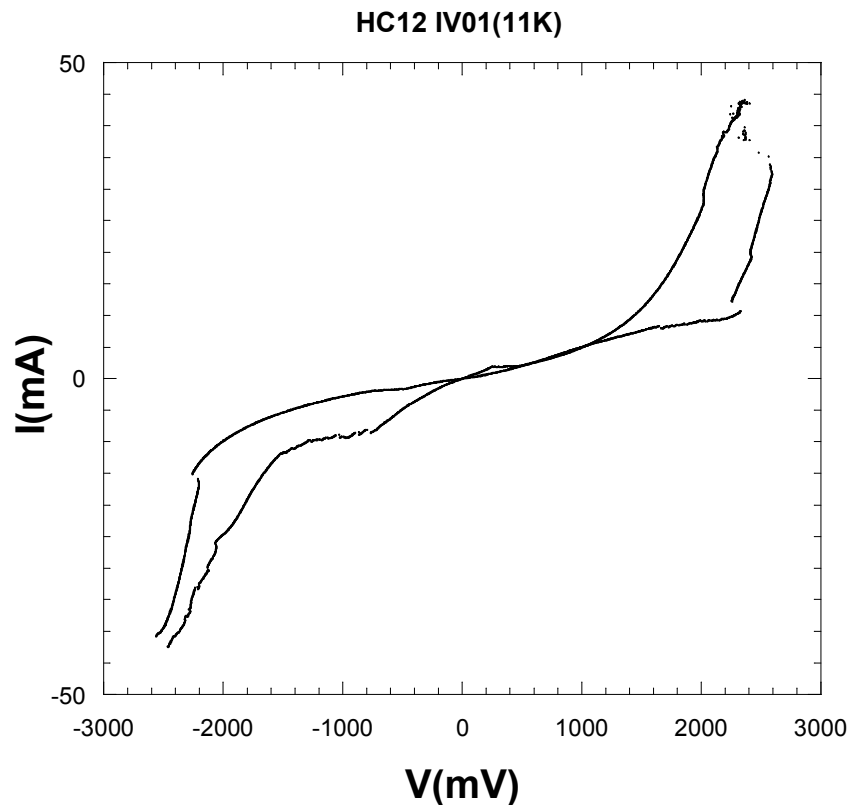
Figure 4.14. I-V measurement of HC12

Temperature dependence of c-axis tunneling characteristic of Bi2212 single crystals was analyzed by I-V measurements done at some constant temperatures. The tunneling behaviors from superconducting state to normal state are seen in figure 4.15 which for the HC09. In the superconducting I-V data, it is generally seen that total conductance peak value decreasing with increasing temperature. It is compatible with temperature dependence of energy gap of BCS theory mentioned in introduction part. For this reason, decreasing in individual energy gap reveals reducing in total conductance peak of IJJ stacks. That could be intrinsically observed in spite of the presence of Joule heating in large number of IJJs. Above T_c, the energy gap feature and other superconducting behavior such a Josephson current are disappeared but there is an interesting result seen in I-V measurements of same mesa at different high temperatures. It is nonlinearities in I-V that is corresponds to increasing c-axis resistance with decreasing temperature. It is presented such pseudo-gap behaviors that are precursor of superconductivity and defines unusual pre-formed of pairs above T_c (Yurgens 2000). It has been observed in underdoped and overdoped Bi2212 single crystals. While it is very

hard to observe presence of pseudo-gap in heavily doped Bi2212, feature of this gap is known as an underdoped behavior (Ozyuzer, et al. 2002).
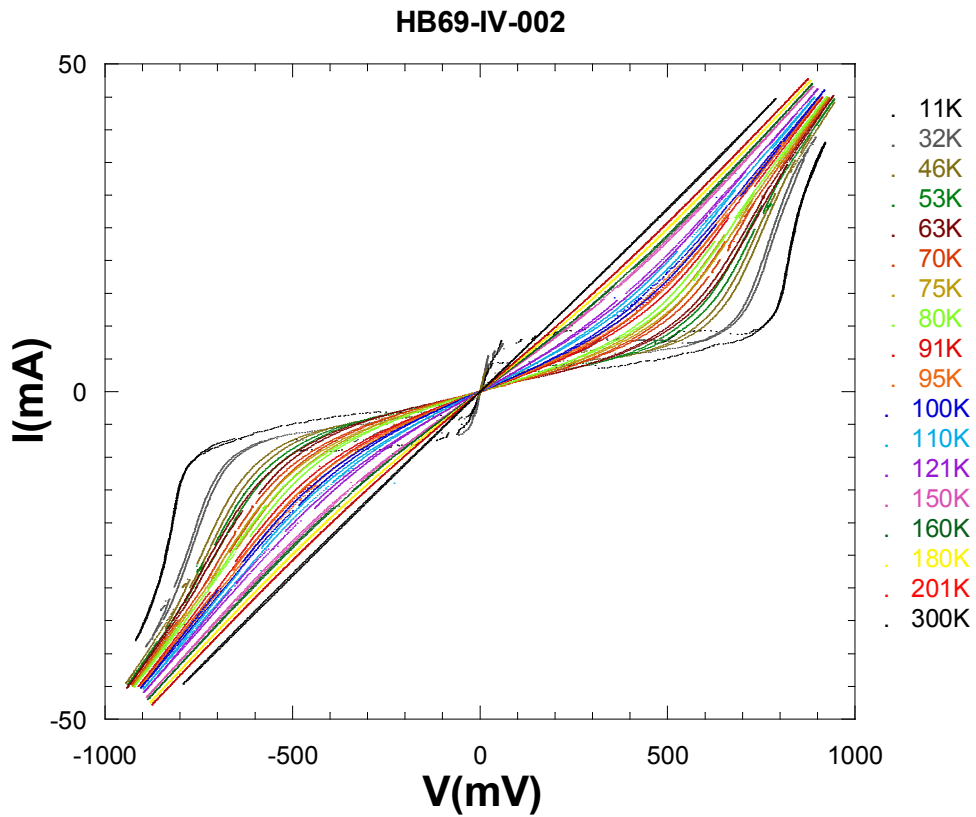

Figure 4.15. Temperature evolution of I-V characteristic of HC09

We also sketched the R-T graph of HC09 from the Temperature evolution of I-V characteristic of HC09 in the figure 4.15. It is almost same with the real R-T results of HC09 such as $T_c (0)$ =46 K and $R_{300 K}$=17.2 Ω, seen in the figure 4.16.

RT from IV Datas of HC09
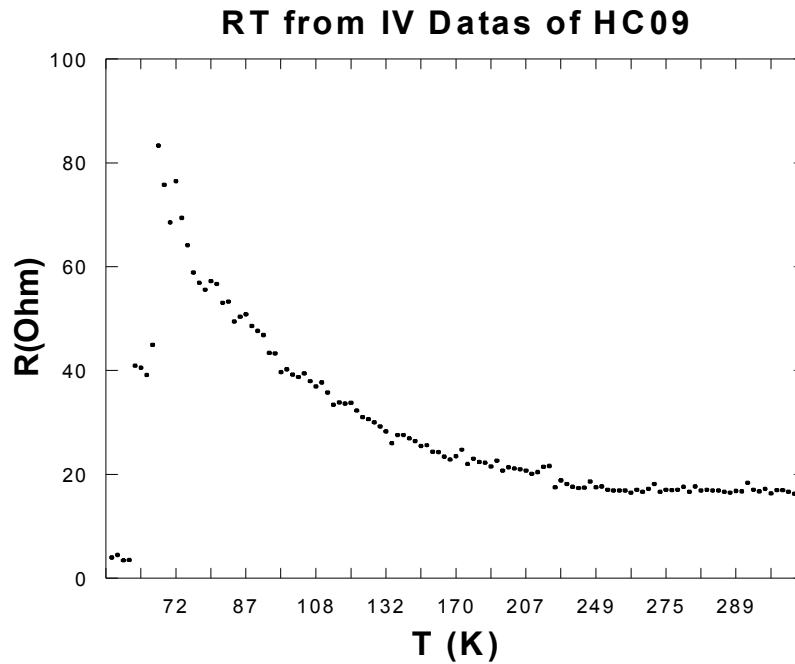
Figure 4.16. R-T graph from Temperature evolution of I-V characteristic graph of HC09

4.3. Bolometric Detection of Radiation from Mesa

All of electrical measurements of mesa were to characterize the superconducting material of Bi2212 single crystal for investigation of THz radiation. The experimental measurements on electrical behaviors of the superconducting material were not only instructive to understand the properties of HTSs, but also to investigate whether they satisfy our radiation considerations from Bi2212. The required mesa dimensions and experimental configurations for THz radiation from Bi2212 were mentioned in chapter 2 and their capabilities in THz emission have been demonstrated in a paper by (Ozyuzer, et al. 2007). A significant radiation at THz frequency range was obtained out of long edge of mesa on Bi2212 single crystal in zero magnetic fields. It results from oscillating current due to voltage drop across the IJJs and it is based on ac Josephson effect. Because of the radiation frequency proportional to the voltage, Josephson junctions are used such a voltage-frequency converter (Josephson 1962). Thus a superconductor with large energy gap provides significant radiation at THz frequency

range. In this study, tall mesas were fabricated, because larger number of IJJs provides more power radiation with better efficiency.

In these measurements, according to our emission consideration, since it is expected that the radiation from long edge of tall mesa is emitted and detected by bolometer while bias voltage decreases, swept frequency of ac current applied by function generator was reduced when it started to decrease. It provides not to skip the synchronization voltages of all junctions. Thus it was allowed to scan detection of radiation at each voltage. In order to ensure the emission from superconducting mesa structure, bolometric output peaks should be reproducible for each scanning of bias voltage decreasing toward to zero. Therefore I-V measurements were allowed to be repeated severally.

Against the influence of variation at ambient temperature on output signal of bolometer, the system was thermally isolated to reduce the background of spurious count. After background was subtracted by lock-in for sensitive detection, bolometric measurements were recorded together with I-V simultaneously. Our bolometer is sensitive to thermal radiation and joule heating occurring because of non-equilibrium quasiparticle tunneling in large and tall mesa is clearly seen at high bias voltages. The back-bending (or heating in the high bias) in I-V and thermal radiation in bolometric measurement at highest bias currents are good evidence of heating and they are clearly seen in figure 4.19.
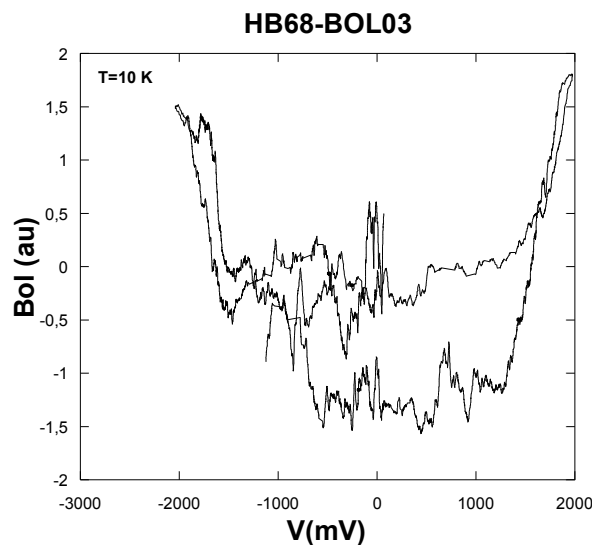

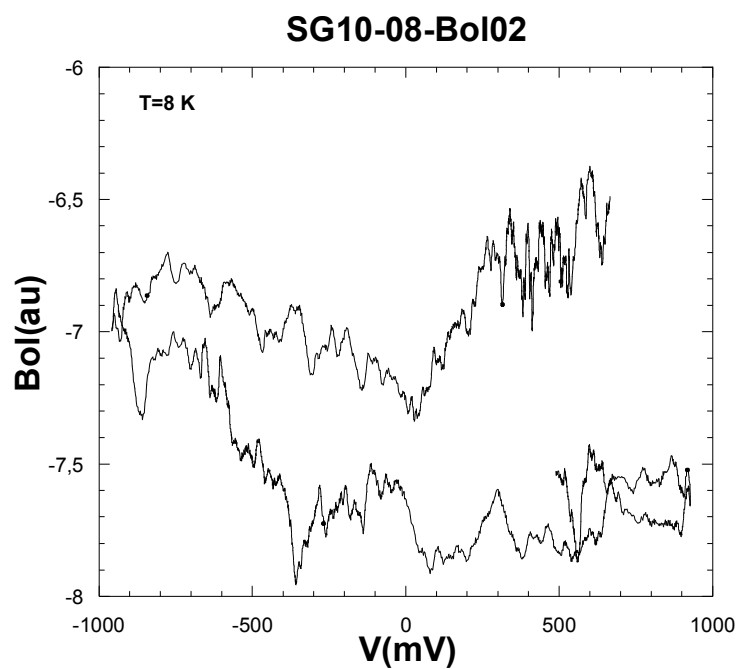Figure 4.17. Bolometer measurements of HC18 at 10 K

SG10-08-Bol02

Figure 4.18. Bolometer measurements of SG10–8 at 8 K
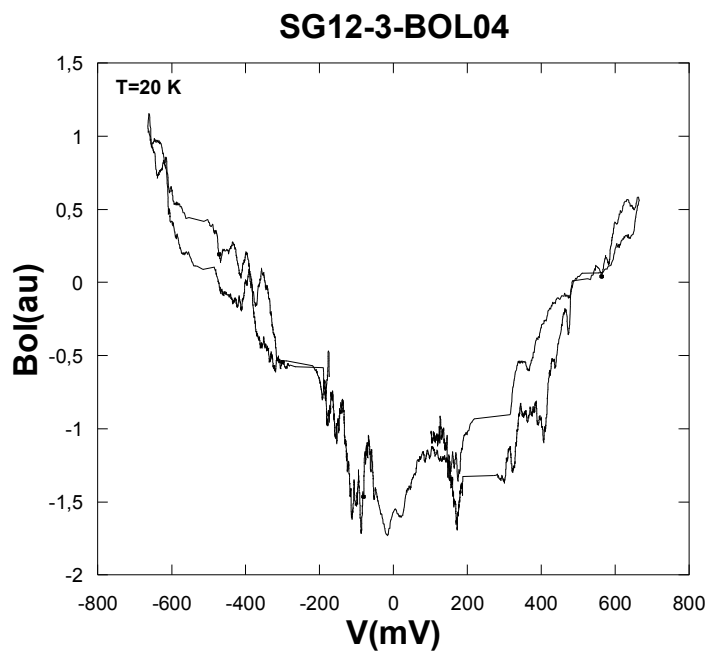
SG12-3-BOL04

Figure 4.19. Bolometer measurements of SG12–3 at 20 K

As can be seen above figures, there are no emission peaks detected by bolometer. Some peaks in bolometric detections were not taken into account since they were both small and irreproducible. Although, the angle of the lateral dimension of the mesa is high apart from the HC12, it was thought that main reason of non-emission is irregular mesa shapes for the both edges. It is clearly seen in (Table 4.1) that not only lateral angles of mesas are low for the HC12 but also their distributions along the all lateral mesa dimensions for the other mesas are quite inhomogeneous. Low lateral angle shows to fabricate such a trapezoid mesa and because of non-rotational sample holder during etching different lateral angles at edges of mesa were obtained. It causes junctions with different areas along the mesa height because junction areas are extended from top of the mesa to crystal surface. Thus junctions have different critical current values.

The other reason of de-synchronization in mesa is heating problem which is general problem for Bi2212. According to our emission consideration, tall and large mesas were fabricated on the contrary small mesa sizes are preferred in recent studies to avoid heating problem, so in our I-V measurements we encountered the effect of heating that is considered to destroy synchronization in IJJ stacks. However it was able to be manageable in large and tall mesas by using underdoped Bi2212 and coherent THz radiation were obtained (Ozyuzer, et al. 2007). Some fabrication design for improving thermal managements of the crystal was explained in a paper published by (Koshelev and Bulaevskii 2008).

CHAPTER 5

SUMMARY AND CONCLUSION

In this thesis, tall and large mesas on $Bi_2Sr_2CaCu_2O_{8+\delta}$ superconducting single crystal were fabricated by thermal evaporation, optical photolithography and reactive ion beam etching techniques. After these processes, mesas which have planar dimensions 60-100x300 μm^2 and thickness about 1 μm respectively were obtained. The lateral angles and heights of mesas were analyzed by AFM, Profilometer and SEM measurements. After the tunneling behaviors of natural layered structure of SIS junctions inside Bi2212 were characterized by R-T and I-V measurements, bolometric detection of emission from long lateral size of mesas were done.

We used Ca-rich Bi2212 single crystals grown by TSFZ method and self flux method for the mesa fabrication. In long mesa fabrication processes, firstly the crystals having smooth alignment planes of SIS junction were glued onto a sapphire substrate by silver epoxy. In order to get a fresh and smooth surface, the crystal was cleaved for better mesa fabrication. Then a gold layer (~50-100 nm) was deposited using vacuum thermal evaporation technique. So, the crystal structures of Bi2212 HTS are protected by the gold layer during some chemical processes. To obtain natural IJJ stacks with various size and height, mesas on Bi2212 have been prepared by optical photolithography and reactive ion beam etching techniques with the three kind of mask such as PR (single layer) mask, Ta/PR (multilayer) mask and PR′/Ta/PR (multilayer) mask. We have obtained tall mesas with sizes are 40-100x300 μm^2.

Our AFM analysis results of the fabricated mesas can be seen in Table 4.1. By using these parameters, mesas with thickness of about 1 μm were able to be fabricated. It was seen from the table 4.1, using multilayer instead of single layer indicates a distinctive increase of the lateral angle, and this is the proof of the approaching nearly rectangular mesa. This is most important achievement of this study. Since ion beam with incident angle of 22.5°-67.5° is accelerated through the sample holder, differences

in lateral angles of mesa occur. If we rotate the sample holder just one direction, there exist height and lateral angle differences between the edges of the mesa. Therefore, sample holder should be rotate with equal time for the both clockwise and counter-clockwise direction.

Due to the difficulties in the contacts on the mesa with small area, firstly CaF_2 insulating layer onto crystal and small area of the mesa and then a gold stripe onto mesa and CaF_2 were deposited by vacuum evaporation after fabrication of mesas. After three points contacts were made, R-T and I-V measurements were performed. The experimental measurements were clearly defined in chapter 3.

In the R-T graphs, sharp phase transitions to superconducting state are seen and the transition temperatures are for the as grown crystals 44 K and 54 K, for grown crystals by self flux method 70 K and 76 K (Table 4.2). It is seen from phase diagram of Bi2212 that they are in underdoped region instead of optimally doped SG12-3. These behaviors in R-T measurements are exponential increasing of resistance at various temperatures from 300 K to T_c and lower T_c than Bi2212 crystals with optimally doped. Furthermore it should be considered the Bi2212 single crystals enriched with Ca. It was discussed in some study their critical temperatures are suppressed due to the excess of Ca content in Bi2212.

It is well known that Bi2212 single crystals have anisotropic electrical behaviors because of their layered SIS structures. Electrical measurements along the mesa height exhibit the characteristic tunneling behaviors including the contributions of whole stacks of IJJs. Large hysterical tunneling behavior of Bi2212 and many number of quasiparticle branches such a voltage jumps are seen I-V graphs. However less number of branches than calculated number of IJJs is seen because of joule heating. Also it causes back-bending at high bias current and causes to decrease total conductance peak of all IJJs. While temperature increase toward T_c, decreases in both sum-gap voltages and hysterical behaviors are clearly seen in temperature evolution I-V graphs. It was found that the order of critical current density J_c is 10^1 A/cm^2. The magnitude is compatible with critical current densities of Bi2212 in underdoped region and lower than J_c of Bi2212 crystals with higher oxygen contents. It is thought to solve heating problems in Bi2212 markedly, because its low critical current does not allow being attained higher bias currents until sum-gap voltage of whole IJJ stacks. Thus less heating occurs in the crystal. Moreover, it is observed that the temperature evolutions of

Josephson critical currents tend to decrease with temperature. However the order of temperature evolution of I_c is small at quite different temperatures and the differences get bigger with temperature differences.

The bolometric measurements were done to detect emission from the Bi2212 superconductors, but there is no emission peak. According to our emission consideration, we expected that the radiation from long edge of tall mesa is emitted while bias voltage along the c-axis in Bi2212 decreases. Therefore I-V and bolometer measurements were recorded simultaneously. The emission peaks have not been observed due to non-identical IJJ stacks with respect to junction area, after the all bolometric measurements performed at different temperatures. Although, the lateral angle of the mesas is high, there was no emission. In order to synchronize all junction stacks in mesa, they should have identical planer areas and their other junction parameters should be same whereas different junction parameters destroy synchronization of whole IJJs or reduce emission capability. Moreover, one of the reasons of the any emission emitted from the Bi2212 is the quality of the Bi2212 single crystals. This indicates that we need certain doping level of the crystals.

REFERENCES

Akimitsu, J., A. Yamazaki, H. Sawa and H. Fujiki. 1987. Superconductivity in the Bi-Sr-Cu-O system. *Japanese Journal of Applied Physics* 26:2080.

Ambegaokar, V. and A. Baratoff. 1963. High temperature superconductors: Processing and science. *Physical Review Letters* 10:486.

Ambegaokar, V. and A. Baratoff. 1963. Tunneling between superconductors. *Physical Review Letters* 11:104.

Anderson, J. R. and J. M. Rowell. 1963. Probable observation of the Josephson superconducting tunnel effect. *Physical Review Letters* 10:230

Artemenko, S. N. and S. V. Remizov. 2000. Stability, collective modes and radiation from sliding Josephson vortex lattice in layered superconductors. *Physica C* 362:200.

Bae, M. H. and H. C. Lee. 2006. Progress in THz generation using Josephson fluxon dynamics in intrinsic junctions. *The Institute of Electronics, Information and Communication Engineers Transactions of Electronics* E89: 411.

Bardeen, J., L. N. Cooper and J. R Schrieffer. 1957. The Theory of Superconductivity. *Physical Review Letters* 108:1175.

Batov, I. E., X. Y. Jin, S. V. Shitov, Y. Koval, P. Muller and A. V. Ustinov. 2006. Detection of 0.5 THz radiation from intrinsic $Bi_2Sr_2CaCu_2O_{8+x}$ Josephson junctions. *Applied Physics Letters* 88:262504.

Bednorz, J. G. and K. A Müller. 1986. Possible high-T_c superconductivity in the Ba-La-Cu-O system. *Zeitschrift Physics* B 64:189.

Bourdillon, A. and N. X. Tan Bourdillon, eds. 1994. *High temperature superconductor: Processing and Science*. New York: Academic Press INC.

Bulaevskii, L. N. and A. E. Koshelev. 2007. Radiation due to Josephson Oscillations in Layered Superconductors. *Physical Review Letters* 99:057002

Cohen, M. H., L. M. Falicov, and J. C. Phillips. 1962. Superconductive tunneling. *Physical Review Letters* 8:316.

Duzer, T. V. and C. W. Turner, eds. 1999. *Principles of superconductive devices and circuits*. London: Prentice-Hall.

Esaki, L. 1957. New Phenomenon in Narrow Germanium p-n Junctions. *Physical Review* 109:603.

Feigelson, R. S., D. Gazit, D. K. Fork and T. H. Geballe. 1988. Superconducting Bi-Ca-Sr-Cu-O fibers grown by the laser-heated pedestal growth methods. *Science* 249:1642.

Ferguson, B. and X. C. Zhang. 2002. Materials for terahertz science and technology. *Nature Materials* 1:26.

Giaever, I. 1960. Energy gap in superconductor measured by electron tunneling. *Physical Review Letters* 5:147.

Giaever, I. 1960. Electron tunneling between two superconductors. *Physical Review Letters* 5:464.

Giaever, I. 1965. Detection of the ac Josephson Effect. *Physical Review Letters* 14:904.

Ginzburg, V. L. and L. D. Landau. 1950. On the theory of superconductivity. *Journal of Experimental and Theoretical Physics* 20:1064.

Gor'kov, L. P. 1959. Microscopic derivation of the Ginzburg--Landau equations in the theory of superconductivity. *Zh. Eksp. Teor. Fiz.* 36:1918.

Gor'kov, L. P. 1960. Microscopic derivation of the Ginzburg-Landau equations in the theory of superconductivity. *Soviet JETP (USSR)* 9:1364

Hazen, R. M., L. W. Finger, R. J. Angel, C. T. Prewitt, N. L. Ross, C. G. Hadidiacos, P.J. Heaney, D.R. Veblen, Z.Z. Shenh, A. El Ali and A.M. Hermann. 1988. 100 K superconducting phases in the Tl-Ca-Ba-Cu-O system. *Physical Review Letters* 60:1657.

Hu, X. and S. Lin. 2008. Three-dimensional phase-kink state in a thick stack of Josephson junctions and terahertz radiation. *Physical Review B* 78:134510.

Irie, A., Y. Hirai, G. Oya. 1998. Fiske and flux-flow modes of the intrinsic Josephson junctions in Bi2Sr2CaCu2Oy mesas. *Applied Physical Letters* 72:2159

Jin, S., T. H. Tiefel, R. C. Sherwood, R. B. Van Dover, M. E. Davis, G. W. Kammlott and R. A. Fastnacht. 1988. Melt-textured growth of polycrystalline $YBa_2Cu_3O_{7-\delta}$ with high transport J_c at 77 K. *Physical Review B* 37:7850.

Josephson, B. D. 1962. Possible new effects in superconductive tunneling. *Physics Letter* 1:251-253.

Josephson, B. D. 1973. The discovery of tunneling supercurrent. *Nobel Lecture*.

Kamimura, H., H. Ushio, S. Matsuno, T. Hamada, eds. 2005. *Theory of Copper Oxide Superconductors*. Berlin: Springer- Verlag.

Katsui, A. 1988. Crystal Growth of Superconducting Bi-Sr-Ca-Cu-O Compounds from KCl Solution. *Japanese. Journal of Applied Physics* 27:L844.

Kleiner R., F. Steinmeyer, G. Kunkel, and P. Müller. 1992. Intrinsic Josephson effects in $Bi_2Sr_2CaCu_2O_8$ single crystals. *Physical Review Letters* 68:2394.

Kleiner, R. 1994. Two-dimensional resonant modes in stacked Josephson junctions. *Physical Review B* 50:6919.

Kleiner, R. 2007. Filling the terahertz gap. *Science* 318:1254.

Koseoglu, H., Y. Simsek, F. Turkoglu, L. Ozyuzer. 2009. Characterization of c-axis resistivity of superconducting $Bi_2Sr_2CaCu_2O_{8+d}$ single crystals grown by self-flux method. *Journal of Optoelectronics and Advanced Materials Symposia* 1(3): 463-466

Koshelev A. E., L. N. Bulaevskii. 2008. Resonant electromagnetic emission from intrinsic Josephson junction stacks with laterally modulated Josephson critical current. *Physical Review B* 77:014530

Koshelev, A. E. 2008. Alternating dynamic state self-generated by internal resonance in stacks of intrinsic Josephson junctions. *Physical Review B* 78:174509.

Langenberg, D. N., D. J. Scalapino, B. N. Taylor, and R. E. Eck. 1965. Investigation of Microwave Radiation Emitted by Josephson Junctions. *Physical Review Letter* 15:294.

Lin, S. and X. Hu. 2008. Possible Dynamic States in Inductively Coupled Intrinsic Josephson Junctions of Layered High-Tc Superconductors. *Physical Review Letters* 100:247006.

London, F. and H. London. 1935. The Electromagnetic Equations of the Superconductor. *Proceeding of Royal Society A* 149:71.

Maeda, H., T. Tanaka, M. Fukutomi and T. Asano. 1988. A New high-T_c oxide superconductor without a rare earth element. *Japanese Journal of Applied Physics* 27:L209.

Madsen, S., G. Fillatrella, and N. F. Pedersen. 2004. Interaction between a BSCCO-type intrinsic Josephson junction and a microwave cavity. *European Physical Journal B* 40:209

Maxwell, E. 1950. Isotope Effect in the Superconductivity of Mercury. *Physical Review* 78:477.

Meissner, W. and R. Ochsenfeld. 1933. Ein neuer effect bei eintritt der supraleitfahigkeit. *Naturwissenschaften* 21(44):787

Michishita, K., Y. H. Ikuhara and Y. Kubo. 1996. *Bi-based superconductor fabricated by floating-zone method*: Bismuth-based high-temperature Superconductors, Edited by Hiroski Maeda and Kazumasa Togano. New York: Marcer Dekker.

Nagai, Y., K. Tsuru, A. Terada and K. Yanagisawa. 1991. Micropatterning of high-Tc superconducting film by nitrogen ion beam and Ta/resist multilayer mask. *IEEE Transactions on Magnetism* 27:1622.

Nicol, J., S. Shapiro, and P. Smith. 1960. Direct measurement of the superconducting energy gap. *Physical Review Letters* 5:461.

Onnes, H. K. 1911. Disappearance of the electrical resistance of mercury of Helium temperature. *Akad. Van Wetenschappen (Amsterdam)* 14:113.

Ono, A., S. Sueno, F. P. Okamura. 1988. Preparation and Properties of Single Crystals of the High-Tc Oxide Superconductor in the Bi-Sr-Ca-Cu-O System. *Japanese. Journal of Applied Physics* 27:L786

Ohring, M. 2002. *Material science of thin films*. San Diego-Academic Press

Ozyuzer, L., J. F. Zasadzinski, C. Kendziora and K. E. Gray. 2000. Quasiparticle and Josephson tunneling of overdoped $Bi_2Sr_2CaCu_2O_{8+x}$ single crystal. *Physical Review B* 61:3629.

Ozyuzer, L., J. F. Zasadzinski, K. E. Gray, C. Kendziora and N. Miyakawa. 2002. Absence of pseudo-gap in heavily over-doped $Bi_2Sr_2CaCu_2O_{8+x}$ from tunneling spectroscopy of break junction. *Europhysics Letters* 58:589.

Ozyuzer, L., J. F. Zasadzinski, K. E. Gray, D. G. Hinks and N. Miyakawa. 2003. Probing the phase diagram of $Bi_2Sr_2CaCu_2O_{8+x}$ with tunneling spectroscopy. *IEEE Transactions on Applied Superconductivity* 13:89.

Ozyuzer, L., C. Kurter, J. F. Zasadzinski, K. E. Gray, D. G. Hinks and N. Miyakawa. 2005. Comparison of intrinsic Josephson junction and SIS tunneling spectroscopy of $Bi_2Sr_2CaCu_2O_{8+x}$. *IEEE Transactions on Applied Superconductivity* 15:181-184.

Ozyuzer, L., A. E. Koshelev, C. Kurter, N. Gopalsami, Q. Li, M. Tachiki, K. Kadowaki, T. Tamamoto, H. Minami, H. Yamaguchi, T. Tachiki, K. E. Gray, W. K. Kwok and U. Welp. 2007. Emission of coherent THz radiation from superconductors. *Science* 318:1291.

Revcolevschi, A. and J. Jegoudez. 1997. Growth of large high-Tc single crystals by the floating zone method: A review. *Progress in Materials Science* 42:321.

Reynolds, C. A., B. Serin, W. H. Wright, and L. B. Nesbitt. 1950. Superconductivity of Isotopes of Mercury *Physical Review* 78:487.

Schilling, A., M. Cantoni, J. D. Guo and H. R. Ott. 1993. Superconductivity above 130 K in the Hg-Ba-Ca-Cu-O System *Nature* 363:56.

Schmidt, V. V. 1997. *The Physics of Superconductors*, Edited by P. Müller and A. V. Ustinov. Berlin: Springer- Verlag.

Shapiro, S. 1963. Josephson currents in superconducting tunneling: the effect of microwaves and other observations. *Physical Review Letters* 11:80

Shishido, T., D. Shindo, K. Ueki, T. Sasaki, N. Toyota, and T. Fukuda. 1989. Growth of Single Crystals in the Bi-Sr-Ca-Cu-O System Using KCl as a Flux. *Japanese. Journal of Applied Physics* 28:L791

Şimsek, Y. 2008. Temperature Dependence of Tunneling in Intrinsic Josephson Junctions of High Temperature Superconductors. *Izmir Institute of Technology Thesis of M.S.*

Tachiki, M., T. Koyama and S. Takahashi. 1994. Electromagnetic Phenomena Related to a low frequency plasma in cuprate superconductors. *Physical Review B* 50:7065.

Takekawa, S., H. Nozaki, A. Umezono, K. Kosuda, and M. Kobayashi. 1988. Single crystal growth of the superconductor $Bi_2(Bi_{0.2}Sr_{1.8}Ca_1)Cu_2O_8$. *Journal of Crystal Growth* 92:687.

Tanaka, H., M. Nakamura, S. Kishida. 2001. Growth of Bi2Sr2CaCu2Oy single crystals by a modified vertical Bridgman method. *Physica C* 357–360:722.

Ting-Wei L. 1995. Studies of crystal growth, oxygen diffusion, flux pinning and flux lattice melting on $Bi_2Sr_2CaCu_2O_x$ single crystals. *Leiden University Kammerlingh Onnes Laboratory and Van der Walls-Zeeman Laboratory Thesis of PhD.*

Tonouchi, M. 2007. Cutting-edge terahertz technology. *Nature Photonics* 1(2):97-105.

Yurgens, A., D. Winkler, N. V. Zavaritski and T. Claeson. 1996a. Strong temperature dependence of the c-axis gap parameter of $Bi_2Sr_2CaCu_2O_{8+x}$ intrinsic Josephson junctions. *Physical Review B* 53:R8887.

Yurgens, A., D. Winkler N. V. Zavaritski and T. Claeson. 1997. The c-axis gap parameter and resistivity of an individual intrinsic tunnel junction in Bi-2212 single crystals. *Physica C* 293:181.

Yurgens, A. 2000. Intrinsic Josephson junctions: Recent developments. *Superconductor Science and Technology* 13:R85-100.

Wesche, R. 1998. *High Temperature Superconductor Materials, Properties, and Application*. Boston: Academic Publishers.

Won, H. and H. Maki. 1994. *d*-wave Superconductor as a Model of High-T_c Superconductors. *Physical Review B* 49:1397.

Wu, M. K., J. R. Ashburn, C. J. Torng, P. H. Hor, R. L. Meng, L. Gao, , Z. J. Huang, Y. Q. Wang and C. W Chu. 1987. Superconductivity at 93 K in a new mixed-phase Y-B-C-O compound system at ambient pressure. *Physical Review Letters* 58:908.